ABSTRACT

WELLE, ERIC JAMES. The Frequency Response of Counterflow Diffusion Flames. (Under the direction of William Roberts.)

Most practical combustion processes rely on turbulent diffusion flames due to their higher heat release rates when compared to laminar diffusion flames. The higher heat release rates occur because of the increased mixing that results from the flame's interaction with the turbulent flow field. Unfortunately, the turbulent combustion process is very complex; therefore, simplified models have been constructed. Flamelet Theory is a method that characterizes turbulent diffusion flames as a collection of strained, laminar, one-dimensional flamelets. One caveat of this model is the flamelets are assumed to respond quasi-steadily to the applied flow field. The focus of my research has been to elucidate the influence of a time varying flow field on the combustion process.

To test the response, the reaction zone of a propane-air counter-flow diffusion flame was subjected to time varying flow fields using speakers. The results of the experiments illustrate a reaction zone that responds quasi-steadily at forcing frequencies up to 50 Hz. Above this threshold, significant departures occur from steady flame behavior. At elevated frequencies, conditions were found where the reaction zone temperature was found to be in phase with the strain rate, signaling a significant deviation from the quasi-steady state assumption. In diffusion flames, the limiting step for the transport of reactants to the flame front is a diffusion process. The time associated with the increasing phase difference is likely a result of the time necessary for reactants to travel through the diffusion layer. As the forcing frequency is increased, the time rate of change of reactants delivered to the edge of the diffusive zone increases; however, a finite amount of time is still necessary for the reactants to diffuse to the flame front. As the forcing frequency increases, this diffusion time

becomes larger relative to the cycle time of the oscillation, which in turn shows up as an increasing phase difference.

Another aspect of this research was to determine the effects of the transient flow field on soot formation. The formation of soot is of great concern as it is considered to be highly carcinogenic. Unlike other flame parameters such as flame temperature and thickness that responded quasi-steadily at low forcing frequencies, the soot volume fraction showed significant deviations from steady flame behavior at lower frequencies. At higher forcing frequencies, it was found that the soot field asymptotes to a steady structure. The cause of the low frequency response is a result of the long time scales associated with soot production.

The results from this work help illuminate the fundamental physics that governs a flame's response to a time varying flow field. It has shown that significant errors can occur when following the quasi-steady state assumption of the traditional Flamelet Theory. It was also shown that even moderately forced flames exhibit a dramatically different sooting structure when compared to steady flames.

THE FREQUENCY RESPONSE OF COUNTERFLOW DIFFUSION FLAMES

by

Eric James Welle

A thesis submitted in partial fulfillment of the requirements for the degree of Doctor of Philosophy

Mechanical Engineering

North Carolina State University

2002

Approved by:

Dr. William L. Roberts Chair of Supervisory Committee	Dr. Richard D. Gould Member of Supervisory Committee
Dr. Clement Kleinstreuer Member of Supervisory Committee	Dr. H. Christopher Frey Member of Supervisory Committee

DEDICATION

My wife Sandra Welle who has supported me in all ways and helps me to be a better person.

My Parents, Roland and Karen Johns, who taught me how to be a good person and to believe in myself.

My siblings, Mike, Robert, Colleen and Scott who helped me to become stronger through competition but always supported me and lifted me up when I was low.

Dr. Samuel Dwane Thomas for all the invaluable advice when I needed it most and for helping me to embark on my educational career.

Erik Martin for being a good friend throughout the years.

BIOGRAPHY

This Eric James Welle was born in Oxnard, California on September 20, 1971. He is the son of Roland and Karen Johns. Eric Welle comes from a family of seven, which is composed of his parents, Roland and Karen Johns, Mike Welle, Scott Welle, Robert Welle, and Colleen Tomes. His father, Roland Johns, was a non-commissioned officer in the United States Navy and his mother was a housewife for the majority of his childhood. As a result of this, he lived in several states, which included California, Hawaii, South Carolina, Georgia, North Carolina and Florida.

His High School education was completed at R. B. Stall High School in Charleston, South Carolina where he was involved in soccer, football, wrestling, and surfing. Upon completion of high school, he became employed as a pipe fitter's apprentice at General Dynamics Electric Boat Division in Charleston South Carolina. After two and a half years of performing what seemed like tedious and endless labor, he enrolled in a community college where he eventually was awarded a scholarship for Mercer University in Macon Georgia. He completed his Bachelors of Science degree in Mechanical Engineering in July of 1997 at Mercer University. He then began his graduate work at North Carolina State University and completed his Masters of Science degree in Mechanical Engineering in December of 1998. He then went on to finish his Ph. D. in Mechanical Engineering in May of 2002 at which time his wife forced him to get a job. He is now living happily ever after.

TABLE OF CONTENTS

LIST OF FIGURES

1 Introduction

The vast majority of practical combustion devices rely upon turbulent diffusion flames. Diffusion flames are desirable in many cases due to the added safety of not having fuel and oxidizer premixing prior to their introduction into the combustion chamber. Turbulent diffusion flames are often most desirable due to their higher heat release rates relative to laminar diffusion flames. Because of its very nature, the small scales in a turbulent flow field increase the mixing at a molecular level (Wilcox, 1998), and this mixing is much more effective at transporting energy and species than what is achieved via a pure gradient driven diffusion process. Also with turbulence, the flame surface area is greatly increased by the large scales. These two factors help to dramatically increase the heat release rate of turbulent flames over laminar flames.

Flamelet theory is a method that models turbulent diffusion flames as a collection of strained, laminar, one-dimensional flamelets (Peters, 1984; Bray and Peters, 1994) and will be further described in Section 1-1. These flamelets are assumed to respond quasi-steadily to the unsteady strain rates of the turbulent flow field. If the turbulent Reynolds number is sufficiently large, there exists a range of eddy sizes where the characteristic turnover times of the smallest eddies are comparable to the diffusion times of the laminar flamelets (Im et al., 1995). This also leads to a wide range of characteristic frequencies (Egolfopoulos and Campbell, 1996). Therefore, it is necessary to investigate the frequency response of flamelets to better understand the applicability of the flamelet model. In doing so, it is also important to investigate the effects of the time varying flow fields on pollutant formation. Of particular interest in this study were the effects of the unsteady flow field on the soot formation process.

In Diesel engines, the combustion process occurs in two sequential phases. The first phase is primarily controlled by auto ignition and consumption of the premixed reactants. The second phase is controlled by diffusion and in many cases, droplet evaporation. In the combustion chamber, the liquid fuel is injected and on the fringes of the spray the fuel is gasified and mixes with the hot high pressure air. In these areas, auto-ignition occurs and initiates the combustion process and quickly consumes the premixed gases. Relatively speaking, due to the presence of molecular oxygen and chiefly the OH radical (Puri et al., 1994; Chao et al., 1998), soot formation is suppressed during the premixed phase. But, as the temperature rises in the combustion chamber, pyrolysis of the parent fuel in the interior region of the spray occurs, which leads to the formation of soot precursors, and therefore large amounts of soot are produced in this fuel-rich/oxygen-poor zone. Diesel engines, as well as other combustion devices, are well known for their tendencies to form large amounts of soot and previous investigators have suggested that flamelet theory may be an appropriate way of modeling the combustion process in practical burners (Krass et al., 1999).

It is appropriate to briefly describe the mechanisms that govern soot production as well as describe its nature. Soot is particulate matter formed during the combustion of gaseous fuels or vaporized components of liquid and solid fuels. Soot composition is very complex and is a function of the fuel, the combustion device, and the operating conditions; however, it is predominately carbon with small amount of hydrogen, which has an empirical formula of approximately C_8H. It has an emissivity (and absorptivity, due to Kirchoffs law) approaching that of a black body. Soot particles are agglomerates of many smaller primary particles which

range from 10 to 200 nm in diameter and are nearly spherical. Typical diameters of primary particles are 30-60 nm and they generally form within a few milliseconds. The total amount of soot emission from a flame is determined by complex interactions between transport and chemical kinetic processes. However, four characteristics of the mixture field/combustion process have a great impact on the sooting tendency of a flame; flame type (diffusion or premixed), fuel type (aliphatic or aromatic), flame geometry and stoichiometric mixture fraction, and flame temperature (Glassman, 1996).

There are four interdependent and competing processes involved in soot formation: precursor formation, particle inception, particle growth, and particle oxidation (Zhang et al., 1992). The first two processes determine the number of soot particles and the last two processes determine the size of the soot particles (Haynes & Wagner, 1981). The parent fuel molecule undergoes pyrolysis as it moves into the high temperature region of the flame resulting in the fracturing of the large hydrocarbon molecules to form smaller hydrocarbon compounds. These unstable radicals are then available to form soot precursors. Soot precursors, polycyclic aromatic hydrocarbons (PAHs), are the building blocks for soot particles and have a benzene ring structure. The concentration of precursors formed controls the total amount of soot formed in a flame.

Fuel type determines the rate of precursor formation. Aromatic fuels, such as toluene, rapidly form soot precursors through condensation reactions, because they retain their ring structure during fuel pyrolysis. Aliphatic fuels such as propane are chain molecules which form soot precursors via a fragmentation process. The fragmentation process is much slower than the

condensation process, and therefore, for the same flame temperature residence time, an aliphatic fuel will form fewer soot precursors than an aromatic fuel, which reduces the total amount of soot formed in the flame. For aliphatic fuels, an important contributor to soot formation has been attributed to acetylene (C_2H_2). It has been shown that in ethylene flames close to the sooting limit, the soot formation reaction is first order with C2H2 concentration, which suggests the soot growth process is most likely to be dominated by reactions of aromatics and soot surfaces with C_2H_2 (Du et al., 1998). Later, it was shown that soot mass growth stops when acetylene disappears in the flame (Xu and Faeth, 2001).

The flame type, diffusion controlled or premixed, determines if molecular oxygen or more importantly if oxygen radicals such as OH are present during the initial stages of soot formation. Large concentrations of oxygen radicals increase the rates of oxidation reactions with fuel radicals, limiting precursor formation. As a result, PAH formation is inhibited in a premixed flame because of the large concentration of oxygen radicals available in the pyrolysis zone. With regards to diffusion flames, more PAHs are formed due to the absence of oxygen relative to a premixed flame and therefore have a higher sooting tendency.

Glassman (1996) describes the particle inception process as being independent of fuel type or flame type. The precursors grow by surface reactions with the remaining hydrocarbon fragments and they are treated as particles when they reach a molecular weight on the order of 1000. The particles form in about 1 ms and are condensed-phase carbon with hydrogen. The particles lose hydrogen to the high-temperature environment and other small hydrocarbons condense onto these primary particles to form larger soot particles. These primarily spherical

particles then agglomerate and the aggregates may contain hundreds of soot particles. Simultaneously, surface reactions with oxygen and OH radicals reduce the agglomerate size. As a result, particle growth and particle oxidation compete to determine the final agglomerate size.

In an undiluted hydrocarbon/air counterflow diffusion flame, the stoichiometric contour is on the air side of the stagnation plane as shown in Figure 1-1. The pyrolysis reactions that lead to soot precursor formation are highly temperature sensitive so once the parent fuel diffuses to the location where the gas temperatures are 1200 – 1500 K, these reactions will initiate. Given sufficient time, primary particles will be formed and begin to agglomerate. Eventually, the agglomerated soot aggregate will reach the point where the concentration gradient driving it to the reaction zone is not sufficient to overcome the forces of the convective velocities, which are in the direction of the stagnation plane. At this point the particle will be convected back to the stagnation plane. In addition to the drag force exerted by the opposing flow field, the soot particles will be pushed back towards the stagnation plane by thermophoretic forces.

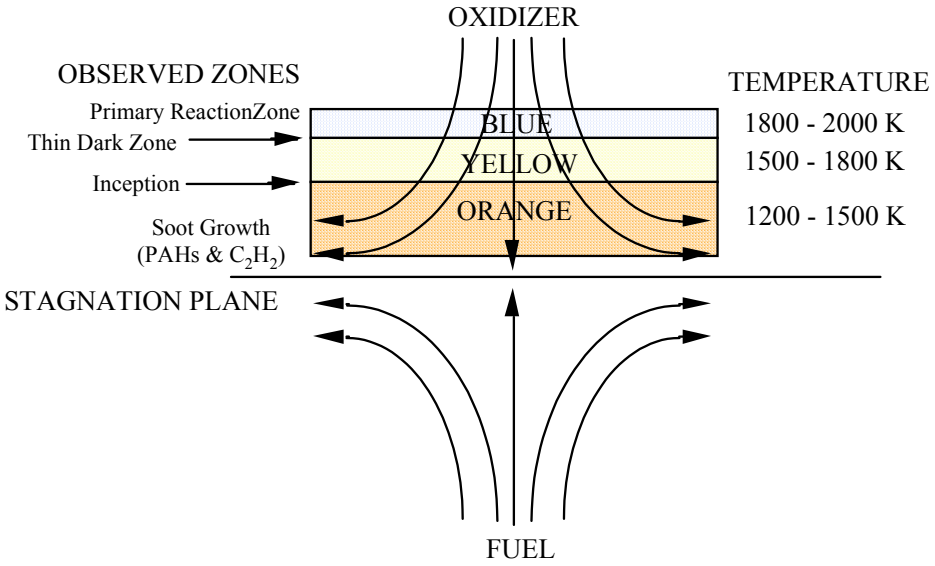

Figure 1-1 Undiluted hydrocarbon/air counterflow diffusion flame geometry and sooting structure from Zhang et. al. (1992)

As a result, it is obvious that the stoichiometric mixture fraction is an important parameter in the counterflow geometry due to its affect on the location of the flame relative to the stagnation plane. If the stoichiometry is such that the flame resides on the fuel side of the stagnation plane (reduced dilution of nitrogen in the air with diluted fuel), the transport mechanisms of the fuel are now convection coupled with diffusion. With this flame configuration, permanently blue flames are found over a wide range of strain rates (Du and Axelbaum, 1995). This is a result of the reduction in the amount of time available for the primary formation and agglomeration processes as well as the soot and its precursors must travel through the reaction zone and are oxidized at the flame front or via molecular oxygen or OH.

It is obvious that soot formation is a complex process which can be affected by many variables. In fact, the soot itself can affect the combustion process leading to a change in the

soot formation process. This can be manifested via the depression of flame temperature due to radiation by soot particles, which in turn will affect the precursor formation process.

In summary, the goal of this research was to determine the effects of an unsteady strain rate on global flame/flow field characteristics such as flame temperature, reaction zone thickness, and the flow field strain rate. Once the effects of these flame/flow field parameters were determined, it was then necessary to determine how they affect the soot formation process. Performing these unsteady measurements will help to illuminate the fundamental mechanisms that govern flame response and soot formation in an unsteady flow field and determine when the quasi-steady assumption is reasonable for modeling turbulent reacting flow fields.

1-1 Flamelet Theory

Turbulent flamelet theory was developed as a conceptual model to describe the turbulent flame structure present in practical combustion devices using simple laminar diffusion flames (Bilger, 1976; Peters, 1984). Flamelet theory treats the turbulent diffusion flame as an ensemble of strained, laminar, one-dimensional flamelets as illustrated in Figure 1-2.

These flamelets must be thin relative to the smallest turbulence scales (Kolmogorov scale) so the laminar substructure of the flamelet is retained. Flamelet theory has been successfully applied to both premixed and diffusion flames where the chemical time is much shorter than all relevant transport processes, i.e. Da >> 1 (Da = reaction_rate/flow_rate).

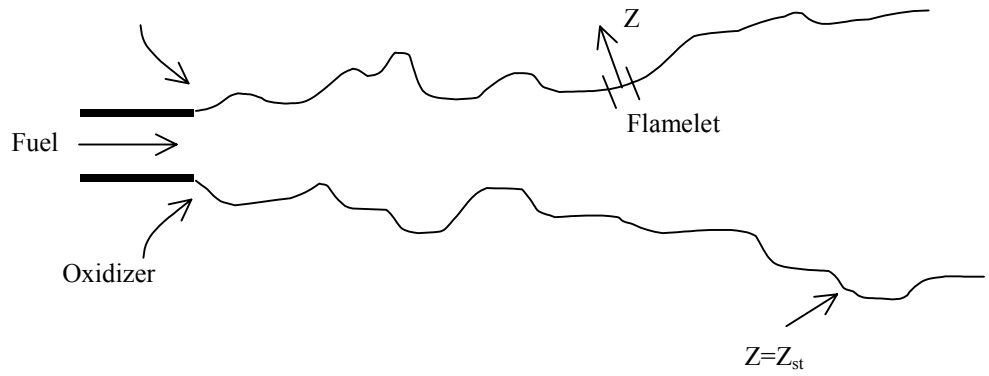

Figure 1-2 Sketch of a turbulent diffusion flame which illustrates a diffusion flamelet

Flamelet theory assumes the 1-D flamelet can be completely described by a single conserved scalar for Da =∞, Le = 1(Le=thermal_diffusivity/mass_diffusivity), and single step chemistry. The conserved scalar used in flamelet theory is the mixture fraction Z, which is a function of the fuel and oxidizer mass fraction and is bounded between zero for pure air and unity for pure fuel.

Equation 1-1 Mixture fraction

$$Z = \frac{\beta - \beta_{O,0}}{\beta_{F,0} - \beta_{O,0}}$$

$$\beta = \frac{Y_O}{M_O \cdot \left(\nu_O'' - \nu_O'\right)} - \frac{Y_F}{M_F \cdot \left(\nu_F'' - \nu_F'\right)}$$

A single variable analysis such as this was first used by Burke and Schumann (1928) to describe a diffusion flame. Their analysis was able to predict flame shape and height reasonably well for the first time. An advantage of this formulation is that all species and temperature profiles are linear in mixture fraction space.

In diffusion flames, the equivalence ratio continuously varies throughout the flow field and in fact Equation 1-1 can be expressed as a function of the equivalence ratio. In the limit of fast chemistry, the flame exists only at the stoichiometric mixture fraction contour. The stoichiometric mixture fraction is calculated from Equation 1-1.

Equation 1-2 Stoichiometric mixture fraction

$$Z_{st} = \left(1 + \frac{Y_{F,1} \cdot \nu_O^{'} \cdot M_O}{Y_{O,2} \cdot \nu_F^{'} \cdot M_F} \right)^{-1}$$

Using this conserved scalar approach, the solution to the governing convective-diffusive equation leads to a universal description of the structure of these flamelets. The above formulation assumes infinitely fast chemistry, Da =∞, so the flame is infinitely thin. Non-equilibrium effects of finite-rate chemistry must be included in the analysis to predict such phenomena as flame quenching or the formation of pollutants such as soot, and NO_x. Finite-rate chemistry means the flame is of finite thickness and is modeled as a diffusive-reactive zone. A second variable, χ, the instantaneous scalar dissipation rate, accounts for non-equilibrium effects.

Equation 1-3 Scalar dissipation, χ, rate defined

$$\chi \equiv 2 \cdot D \cdot \left(\nabla Z \cdot \nabla Z \right)$$

The scalar dissipation rate can be interpreted as the inverse of a characteristic diffusion time and due to the transformation that leads to this parameter, it incorporates the effects of convection and diffusion normal to the surface of the stoichiometric mixture (Peters, 1984 & 1986). The scalar dissipation rate varies inversely with Damköhler number, i.e. as the fluid

transport time gets shorter (higher strain rates), the dissipation rate increases. Evaluating Equation 1-3 at Z_{st} gives the stoichiometric scalar dissipation rate. The scalar dissipation rate is a measure of the heat conduction from both sides of the diffusive-reactive zone. If χ is increased past a critical value, χ_q, then the amount of heat conducted away from the reaction zone exceeds the amount of heat generated by the chemical reaction and the flame quenches. This is shown in Figure 1-3 by the S-shaped curve.

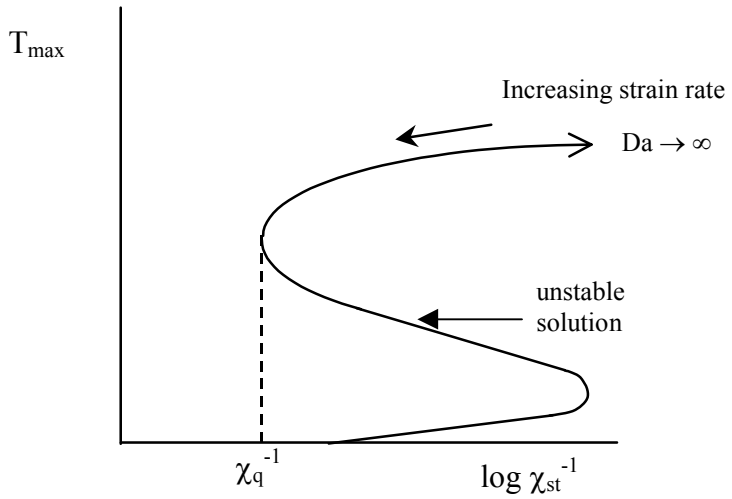

Figure 1-3 The S-shaped curve showing the quenching scalar dissipation rate

The steady, laminar, counterflow diffusion flame (CFDF) has a scalar structure very similar to that of an unsteady distorted mixing layer in a turbulent flow field (Peters, 1984). This makes the CFDF a good model of a flamelet. To experimentally construct the CFDF, a counterflow diffusion flame burner is typically used. Variations of this theme have been used to study the flame structure, reaction rates, and reaction mechanisms of laminar diffusion flames.

This investigation uses an opposed jet burner similar to the design of Seshadri (Puri & Seshadri, 1986), but modified to generate an unsteady flow field (DeCroix, 1998).

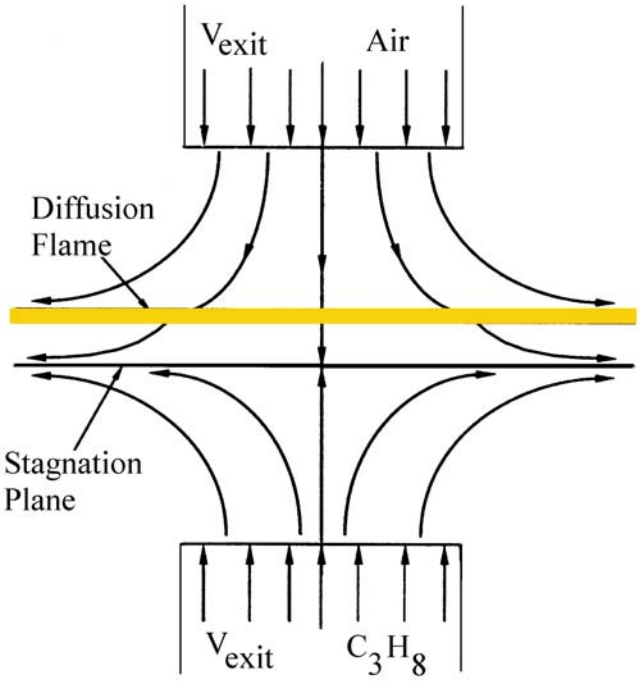

Figure 1-4 Schematic of the stagnation point flow for analysis of counterflow diffusion flames

Figure 1-4 is a sketch illustrating a counterflow diffusion flame stabilized near the stagnation plane of two steady, laminar counterflowing jets of fuel and oxidizer. For momentum-matched opposed jets which are not infinitely far apart, the axial velocity gradient (strain rate) is $K = U_G/(L/2)$, where L is the separation distance of the reactant tubes. This value of strain rate is an exact potential flow solution to the isothermal stagnation point flow field.

For a counterflow diffusion flame, the scalar dissipation rate along the stoichiometric mixture fraction contour for stagnation point flow, has been shown to be a function of the axial strain rate, K (Peters, 2000) and is shown in Equation 1-4.

Equation 1-4 Stoichiometric scalar dissipation rate as a function of the flow-field axial strain rate

$$\chi(Z_{st}) = \frac{2 \cdot K}{\pi} \cdot \exp\left[-2 \cdot \left(erf^{-1}[2 \cdot Z_{st}]^2\right)\right]$$

The scalar dissipation rate is a fundamental parameter as it describes the molecular mixing and couples the reaction zone response to the flow field. Also, this relationship is of critical importance from the perspective that it relates the scalar dissipation rate to an easily measured parameter, K.

For flamelets subject to unsteady strain rates, the scalar dissipation rate is a function of time. As the mean scalar dissipation rate nears the critical value, the instantaneous scalar dissipation rate may make short excursions beyond χ_q, due to fluctuations in the flow field. If the flamelet responds in a quasi-steady manner, then it will quench as soon as the scalar dissipation rate exceeds χ_q. However, if the flamelet survives above the critical scalar dissipation rate, then the quasi-steady assumption is not valid for those hydrodynamic conditions. For unsteady hydrodynamics, flamelet theory may need another variable to account for the temporal dependence of χ.

In a computational study, the issue of the transient response of the flamelet has also been approached using a Lagrangian description (Pitsch et al., 1998). They defined a diffusion time

that helps to quantify the effects of the flow field's rapid changes on the steady nature of the flamelet response as shown in Equation 1-5.

Equation 1-5 Diffusion time

$$t_{\chi} = \frac{(\Delta Z)^2}{\widetilde{\chi}_{st}}$$

Where ΔZ is considered to be the flame thickness in mixture fraction space, which has also been shown to be proportional to $(\Delta Z)_F \propto 1/\sqrt{K}$ (Peters, 2000) and $\widetilde{\chi}_{st}$ is the Favre mean stoichiometric scalar dissipation rate. It was suggested that if the time necessary to exchange mass and energy over ΔZ is small relative to the Lagrangian time, the flamelet is able to follow changes in the scalar dissipation rate rapidly. If this is not the case, they proposed that more unsteady terms in the computations must be retained to properly describe the flamelet response.

The topic of quasi-steady response of flamelets is of great interest and continual research. The results from this work will help to illuminate the controlling mechanism of this response.

2 Laser Diagnostics

When possible, non-intrusive diagnostics techniques are the tools of choice to determine desired quantities so the system is not significantly perturbed by the measurement. The following sections describe laser diagnostic techniques that were used to evaluate the velocity field (Particle Image Velocimetry), reaction zone width (OH PLIF), reaction zone temperature (2-λ OH PLIF), and finally the relative response of the soot field (Laser Induced Incandescence).

2-1 Particle Image Velocimetry Measurements

Particle image velocimetry (PIV) is a planar, non-intrusive technique that provides nearly instantaneous velocity field measurements in a flow-field. In this method, two velocity components are measure to yield the resultant velocity vector. Furthermore, it has been shown that PIV can accurately measure the entire strain field along laminar flames in axisymmetric flow field (Mueller et al, 1998).

With PIV, velocity vectors are determined from sub-sections of the target area called interrogation regions by measuring the displacement of seed particles between two laser scattering events within these regions. Once a sequence of two scattering events is captured and read into memory, the images can be analyzed using peak finding algorithms.

Effectively, the images are divided into interrogation regions and the spatially coincident interrogation regions of the two images are cross correlated. The output of the correlation algorithm is a signal peak that describes the displacement vector $\vec{S}$. Once this displacement vector is determined, the velocity vector can be determined using Equation 2-1 since the time gap between the two pulses Δt is a user adjusted parameter of the experiment.

Equation 2-1 Velocity vector determined from PIV measurements

$$\vec{V} = \frac{\vec{S}}{\Delta t}$$

This procedure is then performed throughout the entire field of a view in each interrogation region and results in a 2D visualization of the flow-field. As stated, this method has the advantage of providing 2D snapshots of the flow-field where as methods such as LDV

provide point measurements and as a result are much more laborious in execution. Essentially, the PIV technique is a Lagrangian particle tracking method that results in an Eulerian velocity field. This is appropriate so long as the time step between laser pulses is small relative to the important time scales of the flow.

The major sources of error that will be present in the PIV measurements are a result of the peak finding algorithm and perspective error. The error introduced from the peak finding algorithm is exactly as expected, which is a result of the cross correlation algorithms ability to identify the appropriate peak that will define the displacement vector $\vec{S}$. The perspective error is a result of the out of plane motion of the seed particles.

The peak finding error in this experiment is expected to be very small. This is based upon the observation that in the cold flow region of the flow field, very few bad vectors are found. This is a result of proper seed density within the interrogation regions and proper displacement of the seeds between the two laser pulses. As a rule of thumb, there should be at least 10 – 25 seed particles in each interrogation region and the particles should be displaced approximately 1/3 of the interrogation region length. These parameters were satisfied in the cold flow region, but due to thermal expansion in the heat release zone, the seed density decreased and many more spurious vectors were found in the high temperature region. This is to be expected due to the low seed density in these regions (Donbar et al., 2001), but this was of little consequence as the strain rate was being calculated in the cold flow region of the flow field.

The perspective error is a result of the motion of the seed particles into and out of the plane of the laser sheets. These unaccounted for components can result in spurious velocity

vectors due to the error it can introduce via the peak finding algorithm. In the flow field studied in these experiments, this error is expected to be minimal due to its laminar axisymmetric nature.

2-2 Laser Induced Fluorescence (LIF)

Laser Induced Fluorescence is an optical technique that has been shown to be invaluable in the quest to describe a wide variety of systems that are of interest to engineers and scientists. It has been shown to be a highly sensitive technique for determining information about population densities of molecular species, which in turn can yield information about species concentrations, density, temperature, reaction zone location and thickness, and velocity. The sensitivity of LIF detection methods can be on the order of ppm or even sub ppm (Crosley, 1980; Crosley and Smith, 1983; Kohse-Höinghaus, 1994). Furthermore, LIF has been successfully used to detect more than thirty species of molecules that include the atomic species O, N, H, C and S (Crosley and Smith, 1983). Initially, LIF was executed as point measurements (Lucht et al., 1982; Chan and Daily, 1980), but has now evolved into planar measurements (Planar Laser Induced fluorescence-PLIF) (Seitzman and Hanson, 1993; Tait and Greenhalgh, 1992; Hanson et al., 1990), which are extremely useful as they facilitate a simultaneous 2D imaging of the target species. This section will briefly describe the theory of LIF and extrapolate it to the specific use of this study, which is to use it as a tool to determine reaction zone temperature and thickness.

Laser-induced fluorescence can be viewed as the absorption of a specific quantum of energy that then elevates the absorbing molecule to an excited state. This excited molecule can then make a transition down to a lower ground state via a radiative decay process, which entails

the molecule re-emitting a photon, which is usually shifted to longer wavelengths (Stokes-shifted), or the complete deactivation of the molecule via collisions with other molecules. This deactivation via collisions is called collisional quenching. Figure 2-1 illustrates the potential curves for two electronic states of the OH radical and a simplified fluorescence spectrum. This shows the two u-shaped potential curves of two electronic states with various vibrational levels. Line (a) on the figure represents the absorption of a photon that bridges a quantized energy gap and elevates the molecule from the v″=0 vibrational band of the $X^2\Pi$ electronic state to the v′=1 vibrational band of the $A^2\Sigma^+$ electronic state. This quanta of energy that will bridge the energy gap to elevate the molecule to an excited state can be shown to be a function of Planck's constant h, the frequency of the photon ν, or to the speed of light c and the wavelength λ. This relationship is stated in Equation 2-2.

Equation 2-2 Quanta of energy required to elevate a molecule to an excited state

$$\Delta E_{1\to 2} = h \cdot \nu = \frac{h \cdot c}{\lambda}$$

Upon excitation, a resonant fluorescence process can occur, which is illustrated by line (b), where a photon is re-emitted with the same frequency or wavelength as the incident light.

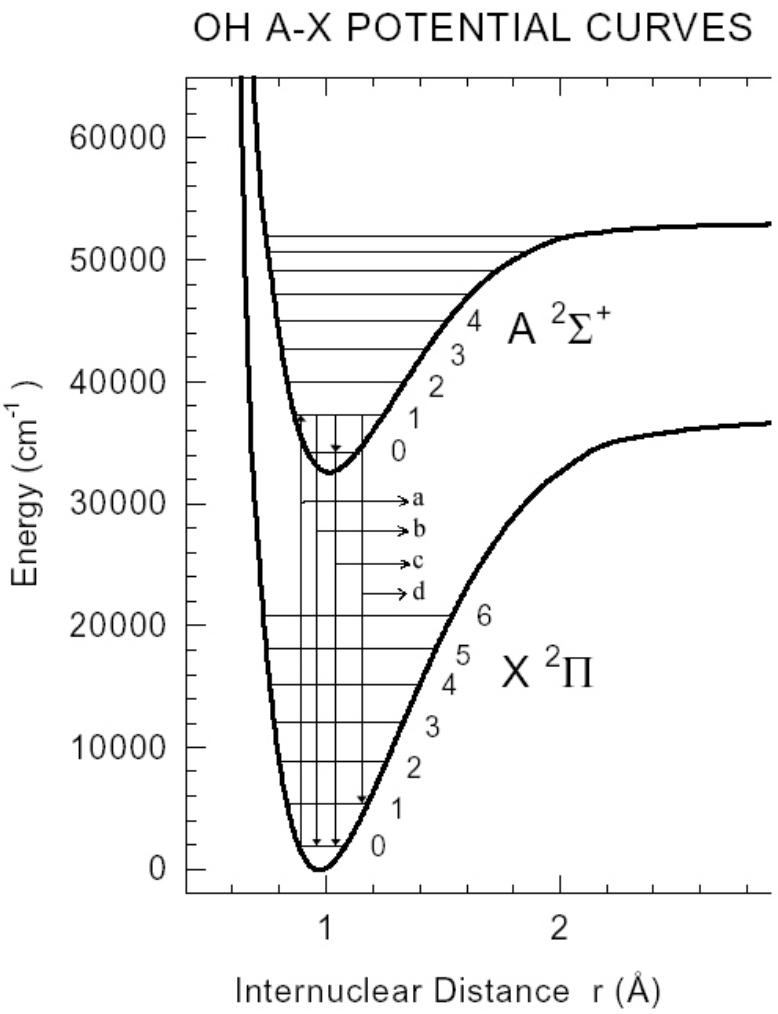

Figure 2-1 Potential curves of the OH radical which shows various vibrational levels and a simplified fluorescence spectrum

Another possible process is illustrated by line (c), where the molecule is demoted from the v′=1 band to the v′=0 vibrational band in the elevated electronic state as a result of collisional processes prior to transitioning down to the ground electronic state via fluorescence at a short wavelength. Another possible process, line (d) is where a photon of a shorter wavelength is emitted as a result of a transition from the v′=1, $A^2\Sigma^+$ state to the v″=0, $X^2\Pi$ state. Figure 2-1 is

a simplified description as it only depicts the vibrational levels and vibrational energy transfer via collisional processes, but these processes can also occur within rotational bands simultaneously. It is also possible for an excited molecule to absorb another photon to elevate it to higher electronic states and possibly ionize the molecule.

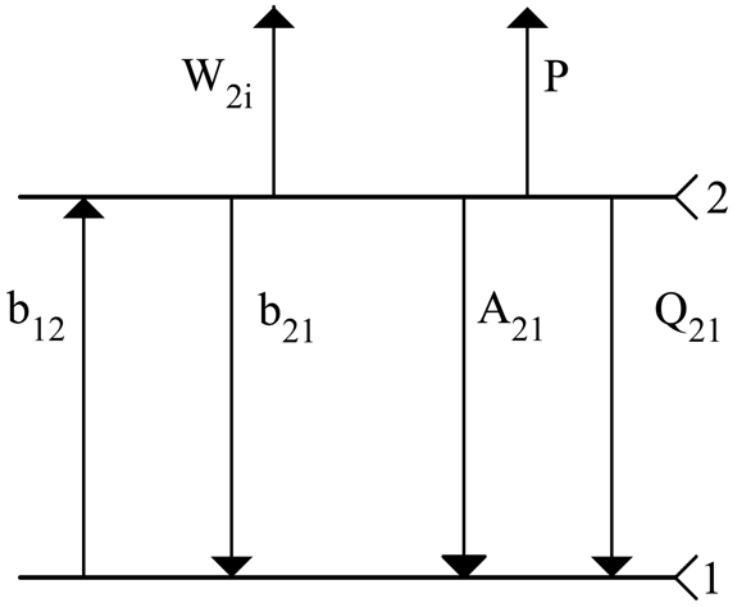

Figure 2-2 Two level energy diagram for LIF modeling

Fundamentally, the models that describe LIF measurements are based upon rate equations. These rate equations describe the excitation rates of molecules to excited rotational, vibrational, or electronic states and the subsequent rates of radiative decay to a ground state as well as photo ionization and collisional quenching rates. A simple two-level energy model is shown in Figure 2-2. In this model, b_{12} is the stimulated absorption rate constant, b_{21} is the stimulated emission

rate constant, A_{21} is the spontaneous emission rate constant, W_{2i} is the photoionization rate constant, P is the predissociation rate constant and Q_{21} is the collisional rate constant. The rate constants can be used to express the rate of population changes for the two levels as shown in Equation 2-3 and Equation 2-4 (Eckbreth, 1996, pp. 390).

Equation 2-3 Rate of change equation for the ground state population N_1

$$\frac{dN_1}{dt} = -N_1 \cdot b_{12} + N_2 \cdot \left(b_{21} + A_{21} + Q_{21}\right)$$

Equation 2-4 Rate of change equation for the excited state population N_2

$$\frac{dN_2}{dt} = N_1 b_{12} - N_2 \cdot \left(b_{21} + A_{21} + Q_{21} + P + W_{2i}\right)$$

It is typically a reasonable assumption to eliminate the rate constants for predissociation and photoionization, thus simplifying the rate equations. It has been shown that the stimulated absorption and emission rate constants shown in Equation 2-3 and Equation 2-1 can be related to the Einstein coefficients for stimulated emission or absorption as shown in Equation 2-5.

Equation 2-5 Relations for stimulated Einstein coefficients and rate constants

$$b_{ij} = \frac{B_{ij} \cdot I_\nu}{c}$$

In Equation 2-5, B_{ij} is the Einstein coefficient for stimulated absorption or emission, I_ν is the incident laser irradiance per unit frequency interval and c is the speed of light. If Equation 2-5 is substituted into Equation 2-3 and Equation 2-4, while assuming a steady state population has been achieved in the two energy levels and ignoring predissociation and photoionization rates,

the rate equations can be solved for the populations in the two states. At this point, an expression for the molecules present in the elevated state (N_2) is desired, because these molecules will be available for a possible fluorescence event, and how N_2 is related to the initially undisturbed ground state population. This relationship, which is a result of the solution of the rate equations under the conditions stated above, is illustrated in Equation 2-6.

Equation 2-6 Relationship between the excited state population and the initial undisturbed ground state

$$N_2 = N_1^{\,0} \cdot \frac{B_{12}}{B_{12} + B_{21}} \cdot \frac{1}{1 + \frac{I_{sat}^{\nu}}{I_{\nu}}}$$

Where $N_1^{\,0}$ is the initial undisturbed ground state population and I_{sat}^{ν} is the saturation spectral irradiance and is defined in Equation 2-7.

Equation 2-7 Definition of saturation spectral irradiance

$$I_{sat}^{\nu} \equiv \frac{(A_{21} + Q_{21}) \cdot c}{B_{12} + B_{21}}$$

Ultimately, a relation is sought between the fluorescence collected to the initially undisturbed ground state population of the molecule and intuitively it is expected to scale with the population of the excited state and the rate of spontaneous emission ($F \propto N_2 \cdot A_{21}$) or more specifically it can be shown in Equation 2-8.

Equation 2-8 Fluorescence signal power

$$F = h \cdot \nu \cdot N_2 \cdot A_{21} \cdot \frac{\Omega}{4 \cdot \pi} \cdot A \cdot l$$

In Equation 2-8, h·ν is the specific quanta of energy necessary to elevate the molecule to the excited state, Ω is the collection solid angle, l is the axial extent along the beam from which the fluorescence is observed, and A is the focal are of the beam. Substituting Equation 2-6 into Equation 2-8, we can now express the result we ultimately seek which is shown in Equation 2-9.

Equation 2-9 Fluorescence signal power as a function of initial undisturbed ground state population N_1^0

$$F = h \cdot \nu \cdot \frac{\Omega}{4 \cdot \pi} \cdot l \cdot A \cdot N_1^0 \cdot \frac{B_{12}}{B_{12} + B_{21}} \cdot \frac{A_{21}}{1 + \frac{I_{sat}^{\nu}}{I_{\nu}}}$$

The result shown in Equation 2-9 is of fundamental importance as it relates the fluorescence yield, F, to the initially undisturbed ground state population, N_1^0. Once this result is stated, the fluorescence can be classified as being in either the saturated or linear regimes. Upon examination of Equation 2-7, if the rate of spontaneous emission is much smaller than the quenching rate ($A_{21} \langle\langle Q_{21}$), we can describe the fluorescence signal using Equation 2-10.

Equation 2-10 Fluorescence signal in the linear regime

$$F = h \cdot \nu \cdot \frac{\Omega}{4 \cdot \pi} \cdot l \cdot A \cdot N_1^0 \cdot B_{12} \cdot I_{\nu} \cdot \frac{A_{21}}{A_{21} + Q_{21}} \cdot$$

This fluorescence regime is what researchers resort to when lower pulse energies are available and as shown in Equation 2-10, the fluorescence signal is linearly related to the laser irradiance. This is usually an unfavorable condition as it requires the quantification of the quenching rate Q_{12} before a true comparison can be made between the fluorescence signal and N_1^0.

Increasingly common, laser systems with higher pulse energies are becoming available that allow researchers to work within the saturation regime. This condition is achieved when $I_\nu \rangle\rangle I_{sat}^\nu$ and effectively shows that the fluorescence is no longer coupled to the laser irradiance, as shown mathematically in Equation 2-11.

Equation 2-11 Saturated Fluorescence Regime

$$F = h \cdot \nu \cdot \frac{\Omega}{4 \cdot \pi} \cdot l \cdot A \cdot N_1^0 \cdot \frac{B_{12}}{B_{12} + B_{21}} \cdot A_{21}$$

This pumping scheme is very desirable as it eliminates the daunting task of correcting for quenching as well as maximizes the signal-to-noise ratio. This method has been successfully executed in many research efforts (Schäfer et al, 1991; Carter et al, 1994 & 1992; Lucht et al., 1983), but the complete saturation of a transition is very difficult. This is due to the fact that the laser pulse has a spatial energy distribution, which is often Gaussian, so saturation will not be achieved at the wings of the beam (Daily, 1978; Ahn et al., 1982). It has been shown in previous saturation measurements using a monochromator (Daily, 1978; Carter et al, 1992), effects of the wings can be minimized by the orientation of the detector slit used. To further complicate this situation, the energy of the pulse is also a function of time so only during the peak of the laser pulse will the transition be truly saturated. To deal with this, researchers have used gate widths for detection on the order of a few nanoseconds that capture fluorescence signal during the peak of the laser pulse.

It should be noted that although the two-level model describes all the basic processes that affect the fluorescence yield, it should not be used if collisional processes are transferring

significant amounts of excited state molecules from the laser coupled state to neighboring energy states. A four level model has been proposed that deals with the transfer of molecules to non-laser coupled states as a result of collisions and spontaneous fluorescence.

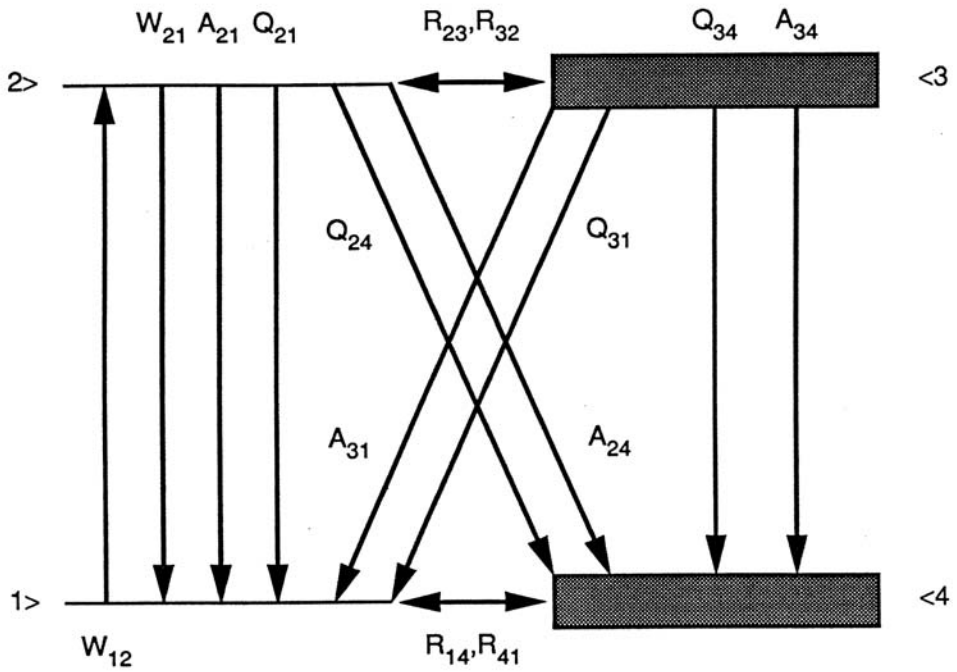

Figure 2-3 Four-Level model illustrating neighboring states that are populated via collisions, fluorescence or quenching from the non-laser coupled states

Where W_{12} and W_{21} are the rates for upward and downward transitions between the laser coupled states, R_{ij} represents the transfer rates between rotational levels and all other parameters have identical definitions as previously presented. The above model better represents the possible processes occurring at the price of simplicity.

With the background just presented, it is now possible to describe the fundamentals of 2-λ OH PLIF thermometry. This topic will be described in Section 2-2-1.

2-2-1 2-λ OH-PLIF Thermometry

The basic premise of the 2-λ thermometry technique is to collect the fluorescence from two sequentially excited states and then relate the ratios of the fluorescence collected to temperature using Boltzmann statistics or a calibration flame. In a turbulent flow field the sequential pulses must occur on a time scale that is small relative to the times scales of a flow. As presented by Eckbreth (Eckbreth, 1996), a possible option of excitation and detection is presented in Figure 2-4. Expressions for the resulting fluorescence signal power are shown in Equation 2-12 and Equation 2-13.

Equation 2-12 Fluorescence from level 3 to 1 as shown in Figure 2-4, assuming steady state

$$F_{31} = \frac{N_2 b_{23} A_{31}}{b_{32} + A + Q}$$

Equation 2-13 Fluorescence from level 3 to 2 as shown in Figure 2-4, assuming steady state

$$F_{32} = \frac{N_1 b_{13} A_{32}}{b_{31} + A + Q}$$

In the above equations, $A=A_{31}+A_{32}$ and $Q=Q_{31}+Q_{32}$. If we assume the fluorescence is within the linear regime the temperature can be determined using Equation 2-14.

Equation 2-14 Temperature as a function of measured fluorescence and fixed experimental parameters

$$T = \frac{h \cdot \nu_{1\to 2}}{\ln\left[\frac{F_{31}}{F_{32}} \cdot \frac{I_{13} \cdot \lambda_{31}^{\ 3}}{I_{23} \cdot \lambda_{32}^{\ 3}}\right] \cdot k}$$

As illustrated by Equation 2-14, the precision of the calculated temperature will be a result of how well fluorescence yields are measured and the pulse irradiance fluctuations quantified.

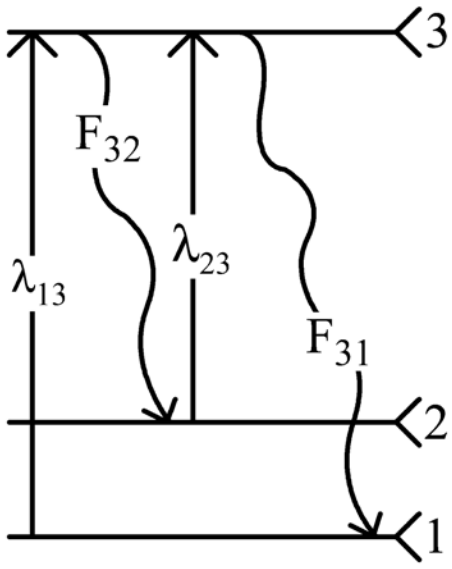

Figure 2-4 2-λ LIF approach as presented by Eckbreth

Cattolica (1981) first applied a 2-λ technique using the OH radical in a flame that is similar to the method just presented. The same rotational level in the upper $A^2\Sigma(v'=0)$ state was excited from two different levels within the $X^2\Pi(v''=0)$ ground state. The resulting fluorescence events were then collected and the ratios yielded temperature. Because the upper state was identical, the quenching rates were the same and therefore were fortuitously eliminated from the analysis. This study reported temperatures that were within ±5% of absorption measurements at 2000 K. In a latter experiment, 2-λ saturation measurements were performed (Lucht, 1982) where no corrections for quenching were necessary as the transitions were saturated. In this study, the 2-λ measurements were found to be within 3 – 5% of the temperature values determined by thermocouple and absorption measurements.

Unlike the scheme presented by Eckbreth, this study used two different rotational levels within the $X^2\Pi(v''=0)$ ground state and sequentially excited them to the $A^2\Sigma(v'=1)$ state. The target specie for this study was the hydroxyl radical (OH) because of its abundance around the reaction zone. The transitions chosen were the $Q_1(5)$ and the $Q_1(14)$ transitions because they are spectrally isolated, have high fluorescence yield and provide good temperature sensitivity. The quenching effects were minimized using a calibration burner. The two line technique has been successfully executed in various burners and with various target species (McMillin et al., 1992; Seitzman et al., 1994; Seitzman and Hanson, 1993; Tsujishita et al., 1999; Palmer and Hanson, 1996).

The hydroxyl radical, whose electronic states are illustrated in Figure 2-1, has been a widely used LIF species because of its unusually well known spectroscopic properties, its strong fluorescence yield and its importance as a reaction zone marker as well as the availability of UV laser sources and detectors with sufficient quantum efficiencies (Welle et al., 2000; Palmer and Hanson, 1996;Crosley and Smith, 1982). For these reasons, it was chosen as the target LIF species in this study. In many cases, the hydroxyl radical is ideally suited for LIF studies in combustion because extensive research has been performed on the emission spectra and collisional energy transfer rates which opens up the opportunity for several avenues of data analysis (Dieke and Crosswhite, 1962; Lengel and Crosley, 1977; Lengel and Crosley, 1978; Dimpfl and Kinsey, 1979; Chidsey and Crosley, 1980; Jeffries et. al., 1988; Raiche et. al., 1990; Tamura et. al., 1998).

2-3 Laser Induced Incandescence

Laser Induced Incandescence (LII) is an optical diagnostics technique where thermal radiation from soot particles is used to deduce the soot concentration. The thermal radiation or incandescence is a result of the soot particles absorbing incident laser energy and being heated to a temperature significantly greater than the ambient flame temperature. It is a spatially and temporally resolvable measurement technique that has become very popular due to its simplicity. The LII technique has been used by several researchers to quantitatively measure soot volume fraction in steady flat and coflow diffusion flames when coupled with a calibration source (Appel et al., 1996; Will et al., 1996). Vander Wal has used LII combined with laser induced fluorescence to investigate soot particle inception (Vander Wal, 1996; Vander Wal et al., 1997). Pinson et al. (1993) used LII to measure soot volume fractions in a test diesel engine. Shaddix and Smyth (1996) measured soot volume fraction in an unsteady coflow diffusion flame using LII.

An early investigation resulted in an energy balance that describes the dominant mechanisms of energy exchange for a soot particle (Melton, 1984). This energy balance is shown in Equation 2-15 where the subscripts s and v denote properties for the solid and vapor phases of carbon respectively.

Equation 2-15 Soot particle energy balance

$$K_{abs}(r)\cdot q-\frac{8\cdot K_a\cdot(T-T_0)}{G\lambda}\cdot\frac{\Delta H_v}{W_s}\cdot\rho_v\cdot U_v-4\cdot\sigma_{sb}\cdot\left(T^4-T_0^{\,4}\right)-\frac{4}{3}\cdot\rho_s\cdot C_s\cdot r\cdot\frac{dT}{dt}=0$$

The first term is the rate of laser energy absorbed by the particle, where q is the laser power density. The absorption efficiency, K_{abs}, is a linear function of particle radius, r, when $r < \delta$ and is constant for $r > \delta$. The absorption length parameter, δ, is a function of the index of refraction, and is ~ 100 nm for the visible probe wavelengths used in this work. The second term in the energy balance is conduction from the particle to the environment, which is assumed to be air at the flame temperature, T_0. K_a is the thermal conductivity and $G\lambda$ is a correction factor required to account for non-continuum heat transfer effects. The last three terms in Equation 2-15 are the energy required for vaporization of carbon, radiation of the particle to the environment, and rate of internal energy increase. Similar expressions are reported in more recent studies (Stephan et al., 1998).

Examination of the energy balance has led to some qualitative conclusions about the laser heating of soot particles (Melton, 1984). Once the particle reaches the vaporization temperature (~ 4000 K – 4900 K), the dominant heat loss mechanism of the particle is the phase change, which limits the increase in temperature. Radiation only becomes important at very high temperatures due to the T^4 dependence and finally, the heat loss terms are only a function of temperature and not particle radius.

In the limit of high laser energy coupled with soot particles that are at the vaporization temperature, Equation 2-15 reduces to Equation 2-16.

Equation 2-16 Soot particle energy balance for high laser fluence and particles at the vaporization temperature

$$K_{abs}(r)\cdot q + \frac{\Delta H_v}{W_s}\cdot\left(4\cdot\rho_s\cdot\frac{dr}{dt}\right)\cong 0$$

If the particle size is limited to small particles, $r < \delta$, it can ultimately be shown that the incandescent signal, J, from a soot field which has been heated to the vaporization temperature by laser radiation can be expressed using Equation 2-17, where N is the total number density and P(r) is the normalized probability density for particles of radius r:

Equation 2-17 Soot field incandescence signal

$$J = C_1 \cdot \int_0^\infty NP(r) \cdot r^x dr$$

$$\text{where } x = 3 + \frac{0.154}{\lambda_{em}}$$

For a black body, the wavelength of peak intensity, λ_{em}, is inversely proportional to the temperature by Wein's law. For a particle temperature of ~ 4000 K, λ_{em} is ~ 0.7 μm which yields an exponent of 3.21. From this result, the incandescence signal approximately scales with soot particle diameter when detection is in the visible or infrared. Therefore, in the maximum temperature limit, the laser induced incandescence signal is approximately proportional to the soot volume fraction. In practice, using LII as a diagnostic technique requires appropriate choices for pumping and signal detection in order to maintain this proportionality to soot volume fraction.

Melton's analysis shows the LII signal is a function of particle size, temperature, time, laser fluence, detection wavelength and bandwidth. Therefore, choices made by the researcher

for probe wavelength and laser fluence as well as detection wavelength and timing determine how closely the experiment matches the assumptions made in Melton's analysis. The following is a discussion of the choices available to the researcher and how they impact the LII measurement.

The probe wavelength determines the absorption length parameter, δ, which defines the upper limit of small particle sizes, $r < \delta$. Longer probe wavelengths allow larger particles to satisfy the criteria, thereby, increasing the particle size range of the LII measurement. However, probe wavelength has a more important role in determining the spectral range of detection. Probe wavelengths at the lower end of the visible spectrum cause both PAHs and C_2 to fluoresce in many spectral bands within the range of detection wavelengths. These fluorescence signals add to the LII signals and, in some cases, can entirely mask low LII signals if not properly filtered. This severely limits the choice of detection wavelengths and bandwidths. Infrared probe beams do not excite fluorescence of either PAHs or C_2, which opens the entire visible spectrum for LII detection. However, they are difficult to work with in the laboratory.

The threshold fluence, which is the laser irradiance at which the LII signal becomes insensitive to changes in laser irradiance, is determined experimentally by monitoring the incandescent signal from a sooting flame over a range of laser fluences. The curve rises rapidly until reaching the threshold fluence where the slope of the signal line adopts a value with a small positive slope. This signal response is valid for a Gaussian beam profile (Tait & Greenhalgh et. al., 1993; Shaddix and Smyth, 1996). With top hat profiles, significant vaporization can occur and the incandescence signal adopts a negative slope shortly after the threshold fluence is

reached (Shaddix and Smyth, 1996). Shaddix and Smyth also did an extensive study of LII signal as a function of laser fluence using different fuels and detector gate widths. When plotted on a log-log scale, their results clearly show a threshold fluence of ~ 0.03 J/cm^2, which was independent of fuel and detector gate width. Interestingly enough, this fluence is similar to that reported elsewhere as the lower range at which LII measurements can be calibrated to determine soot volume fraction (Vander Wal and Jensen, 1998).

Recent research has shown excessive laser heating can change the soot particle composition and significant mass loss can occur by vaporization (Vander Wal et. al., 1995). However, significant beam or sheet attenuation can occur in flames with a high concentration of soot and the threshold laser fluence may not be sufficient to heat particles furthest from the laser to vaporization temperature (Quay et. al., 1994). Both situations introduce error into the soot volume fraction measurements. Therefore, the appropriate laser fluence is sufficient for heating all particles in the probe volume to the vaporization temperature without causing significant mass loss due to vaporization. A laser fluence of ~0.5 J/cm^2 was used in this work and was determined by the experimental method described above.

Measurable incandescence signal can be seen for hundreds of nanoseconds after the laser pulse as the particle cools (Quay et. al., 1996; Bryce et al. 2000). For time-resolved LII measurements, the long duration of the LII signal raises the issue of gate width and temporal position of the gate relative to the laser pulse, because it is easy to bias the measurements to large particle sizes. Small particles cool faster than large particles, because they have a higher surface area to volume ratio. Therefore, a long gate width or delaying the gate significantly after the

laser pulse biases the LII measurements to large particles. Short gates do not bias the data but do significantly reduce the LII signal, which decreases the signal-to-noise ratio. A medium width gate of 30 ns was used in this investigation with the gate opening just prior to the laser pulse. Based upon previous research (Shaddix and Smyth, 1996), this gate width should have no significant bias towards large particles.

As previously noted, the LII signal decay is a function of particle size and persists at a detectible level for hundreds of nanoseconds. In more recent studies, investigators have used ratios of time delayed images to infer information about particle size distributions (Will et al., 1998; Mewes and Seitzman, 1997). Due to the intense interest in size distributions of the soot particulates because of the health concerns associated with the size distributions, these efforts will be of continued interest.

Without calibration, LII can provide qualitative information about the soot field (Cignoli et. al., 1992; Tait & Greenhalgh et. al., 1993; Greenhalgh, 1994). In order to quantitatively measure soot concentrations, the LII technique must be calibrated to a known soot volume fraction. This was not performed in this study as a qualitative description derived from the currently measurements were coupled with quantitative soot volume fractions from previous investigations in this lab (DeCroix and Roberts, 2000).

3 Experimental Apparatuses and Conditions

As stated in Peters (1986), the counterflow diffusion flame burner is the most appropriate choice for constructing an experimental flamelet on which measurements may be performed. Section 3-1 describes the counterflow burner used in this study. The optical systems used to perform particle image velocimetry (PIV), reaction zone thickness, reaction zone temperature, and laser induced incandescence (LII) measurements of soot are described in Sections 3-2, 3-3, and 3-4 respectively.

3-1 Counterflow Diffusion Flame Burner

Figure 3-1 is a schematic of the counterflow diffusion flame burner (CFDF). This burner is a modified version of the burner designed by Prof. K. Seshadri (Puri and Seshadri, 1986).

The burner was mounted on a lab jack and the jack was mounted on a self supporting platform. This platform was then fixed to the optical bench via optical rails. The height of the burner was adjusted by raising or lowering the lab jack. The CFDF burner was operated at atmospheric pressure and was constructed of stainless steel except for the plenums which were fabricated from aluminum. The reactants were delivered via 2.54 cm diameter tubes centered in the top (oxidizer side) and bottom (fuel side) halves of the burner. The oxidizer side was supported above the fuel side by four threaded rods which allowed the easy removal of the upper half of the burner and the tube separation distance to be quickly changed.

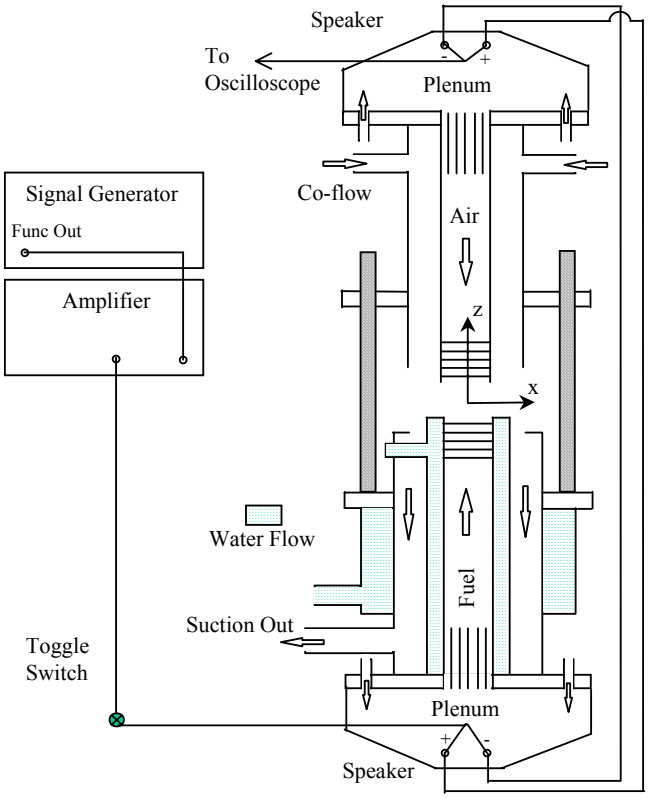

Figure 3-1 Schematic of Counterflow diffusion flame burner

The oxidizer tube was surrounded by a 0.6 cm thick annulus for a nitrogen coflow, which prevented preheating of the oxidizer and entrainment of ambient air into the reaction zone. A separate nitrogen line was plumbed into the fuel line for purging the fuel plenum before and after shutting off the fuel. The fuel tube was surrounded by an inner water jacket to prevent preheating of the fuel. Combustion products were evacuated from the reaction zone by suction through an annulus surrounding the inner water jacket. The suction was provided by a standard shop-vac attached to the burner with a vacuum hose. The pressure in the vacuum was monitored with a manometer attached to the vacuum line. For these experiments, the suction was

maintained at 2 inches of water. Another water jacket formed the outside wall of the suction annulus and provided some cooling of the combustion gases. A large heat exchanger was installed between the burner and the shop-vac to cool the gases to near room temperature.

A 25-mesh screen was laid across the entrance to the exhaust annulus to help stabilize the flame. The flame attached itself to the screen, so there was heat transfer and soot deposition to the screen. In previous studies, it was found that this screen did not affect extinction values so it was deemed that there was no negative consequence of its use (DeCroix, 1998).

Five one inch, 80-mesh, stainless steel screens, separated by 3 mm spacer rings, were press fit 6 mm from the exit of both delivery tubes. The screens flattened the exit velocity profiles and broke up any large scale structure. It was imperative that the screens were very flat, especially the last screen, because any curvature caused non-uniform velocity profiles. This configuration proved to be very unwieldy during the PIV measurements as it required frequent screen changing due to seed particle buildup. In the event of another burner being built, it would be advantageous to consider a converging nozzle to flatten the flow-field and possibly the use of a single exit screen. In addition to the screens, a series of copper tubes, 5 cm in length and 3 mm outer diameter, were press fit into the entrance of each reactant delivery tube to help straighten the velocity profile down the centerline of the reactant tube.

Aluminum plenums that were 20 cm outer diameter and 5 cm in length were placed on the fuel and oxidizer sides and sealed to the burner with silicon sealant. The reactants were supplied to the burner through two 1/4″ NPT ports in the base plate of each plenum shown in Figure 3-1.

The plenums were capped by 20 cm Kicker C8a subwoofer loudspeakers. The speakers had a frequency response range of 30 to 600 Hz and were wired in parallel, as shown in Figure 3-1, for an impedance of 4 Ω.

The unsteady flow-field was generated by applying a sine wave with a set frequency and amplitude to the speakers. The sine wave was generated by an SRS Model DS335 signal generator. An inherent limitation of the signal generator was that it had an upper amplitude limit of 5 V_{p-p} and could not provide enough current to drive the loudspeakers at even small amplitudes. A McIntosh amplifier was used to provide adequate current to the speakers and provide a 2:1 amplification of the signal for studying large amplitude fluctuations. The amplifier response had a slight frequency dependence, so for a consistent amplification, the system was calibrated for a 2:1 amplification at a forcing frequency of 10 Hz and forcing amplitude (amplitude set on the signal generator) of 1 V_{p-p}. Also, there was a switch between the amplifier and the speakers that allows signal interruption without powering off the signal generator.

3-2 Simultaneous PIV and OH Field Thickness Measurements

The layout for the optical system used to simultaneously measure the velocity field via PIV and the OH field thickness is illustrated in Figure 3-2. The velocity field was measured to determine the strain rate, which is the inverse of a characteristic time scale for the flow field. The OH field thickness was measured so the response of the reaction zone to the unsteady flow field could be determined.

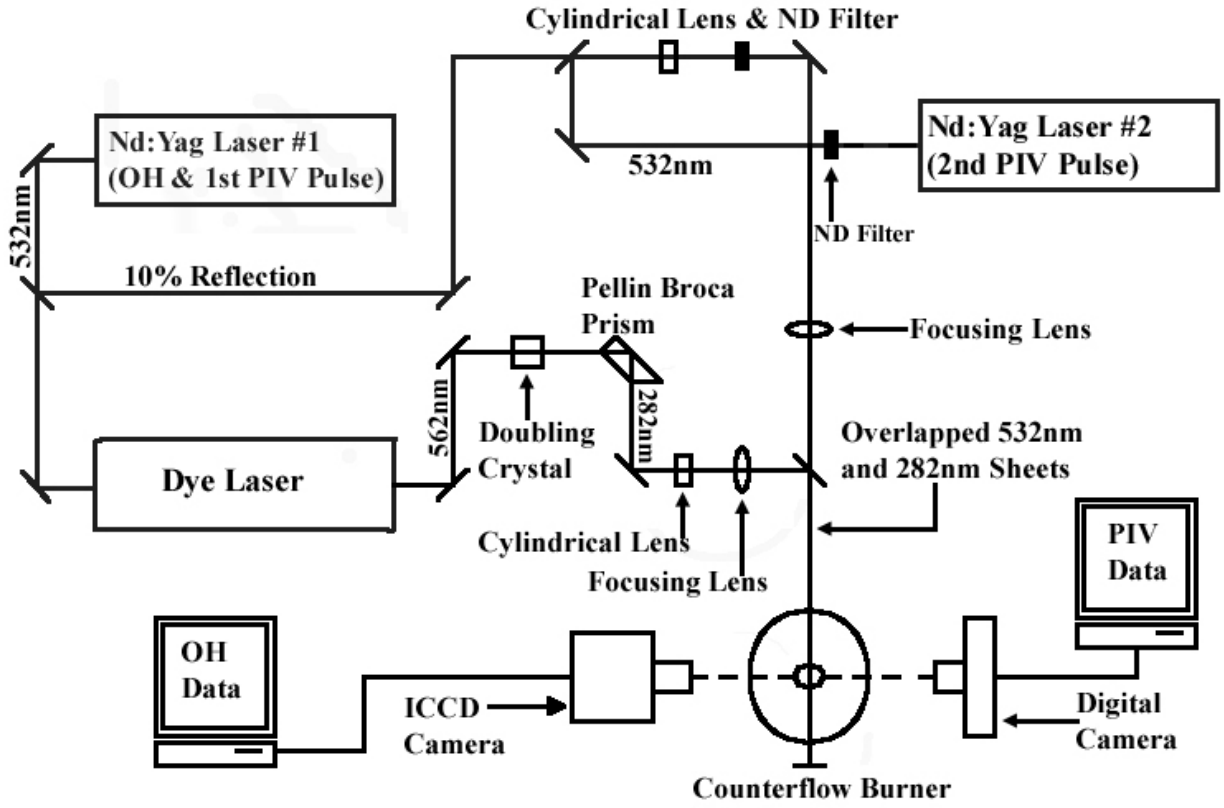

Figure 3-2 Optical Layout for PIV and OH-PLIF measurements

3-2-1 PIV Measurements

The PIV measurements were made using two frequency doubled Nd:YAG lasers (λ = 532 nm). The first PIV pulse was supplied by picking off approximately 10 % of the output of the first Nd:YAG laser. The second PIV pulse was supplied from the output of a second Nd:YAG laser. A neutral density filter (ND Filter) was used for the second PIV pulse to reduce the intensity of the output beam to be more consistent with the intensity of the beam from the first PIV pulse. The beams were spatially overlapped prior to the interrogation region using a dielectric thin film polarizer that preferentially reflects vertically polarized light. The

horizontally polarized light of the 2nd PIV pulse was changed to vertically polarized light using a combination of two mirrors that reduced the height and direction of the beam. Once the two beams were spatially overlapped, a Galilean telescope with cylindrical ocular and objective lenses of focal lengths f = -100 mm and f = 400 mm were used to expand the beam to a height of 20 mm. After this expansion, another ND filter was used to further reduce the intensity of the light so as not to saturate the camera used to collect the scattering images. Finally, the horizontal widths of the two sheets were set to 500 μm using an f = 1 m lens and an iris was used to reduce the height of the beams to 12.7 mm.

The PIV images were recorded using a Kodak ES 1.0 interline-transfer digital camera (1008x1012 pixels, ~70 px/mm) fitted with a 105 mm lens, using an f stop of 8. An interference filter centered at 532 nm with a FWHM of 3 nm was used to block background flame emission. Using this camera, there is no directional ambiguity of particle motion due to the sequential readout of the frames as is the case with two color PIV techniques (Watson et al., 1999). In pulsed acquisition mode, the ES 1.0 can collect images with a time delay as small as 10 μs, which allows the determination of velocity field information of flow fields with small time scales. The timing for the second PIV frame was selected to achieve reasonable particle displacements, typically 10 to 20 pixels on the CCD array.

Custom software developed at ISSI Inc. of Dayton Ohio, which included cross correlation algorithms, was used to derive the velocity field from the two scattering images collected with the Kodak ES 1.0 camera. Interrogation regions composed of 64 pixel squares (0.9 mm x 0.9

mm) with 75% overlapping were employed for the velocity measurements. Effectively, this resulted in velocity field information at approximately 0.12 mm intervals.

To provide the surfaces for the light scattering, the air side of the flow was seeded with hollow Zeospheres, having a mean diameter of 2.2 μm. Due to the stoichiometry, the propane-air flame will sit on the air side of the stagnation plane and thus the transport of the oxidizer is a result of convection and diffusion where the fuel is transported via diffusion only. As a result, it was only necessary to determine the velocity field on the air side of the flow.

3-2-2 OH Field Measurements

As shown in Figure 3-2, the OH measurements were made using a Nd:YAG pumped dye laser, which was running Rhodamine 590 dye. The output of the dye laser was 562.518 nm and was then passed through a BBO frequency doubling crystal to frequency double a portion of the input beam. After the BBO crystal, laser light of 562.518 and 281.259 nm and the two beams were separated using a Pellin-Brocca prism. The UV laser light was then passed through a Galilean telescope with cylindrical ocular and objective lenses of focal lengths f = -100 mm and f = 400 mm were used to expand the beam. Finally, prior to the final turning mirror, the beam passed through an f = 1 m focusing lens, yielding a nominal 10 ns pulse which was 10 mm high with a measured thickness of 300 μm. Using the UV beam, the $R_1(8)$ transition of the $A^2\Sigma+ \leftarrow X^2\Pi(1,0)$ band was excited, partially saturating the transition.

The Stokes shifted spontaneous fluorescence was then collected using a Princeton Instruments ICCD camera (576x384 pixels, ~20 px/mm). Coupled to the ICCD camera was a

UV grade 105 mm/f4.5 lens fitted with UG-11 and WG-295 filters to discriminatorily collect the OH fluorescence. The $R_1(8)$ transition was chosen because of its reduced sensitivity to temperature fluctuations; indeed, the maximum OH signal varied by less than 5% from the average cycle value for any of the experimental conditions. This is further illustrated in Figure 3-3 which shows the normalized calculated fluctuation of the N″ = 8 ground state population over the temperature ranges measured in the counterflow diffusion flame burner.

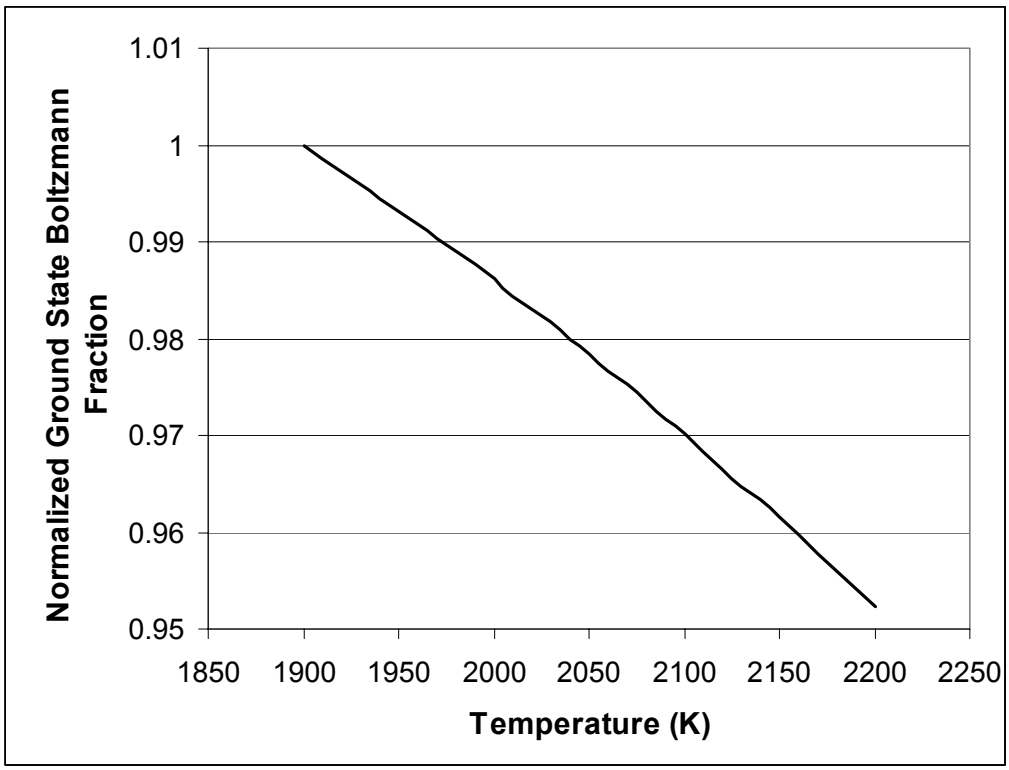

Figure 3-3 N″ = 8 calculated ground state population over the expected temperature range normalized by the peak value

Consistent with measurements, the expected fluctuations of the ground state for the $R_1(8)$ transition will be less than 5 % based on Boltzmann populations.

3-2-3 Timing and Wiring

As shown in Figure 3-2, the pump beam for the first PIV pulse also pumped the dye laser whose output excited the $R_1(8)$ transition of the OH radical. Due to inherent delays in the dye laser, this allowed the passage of the first PIV pulse through the interrogation region of the flame prior to the pulse that excited the OH radical. Finally, the second PIV pulse arrived in the interrogation region a fixed time later that was set based on local flow field time scales.

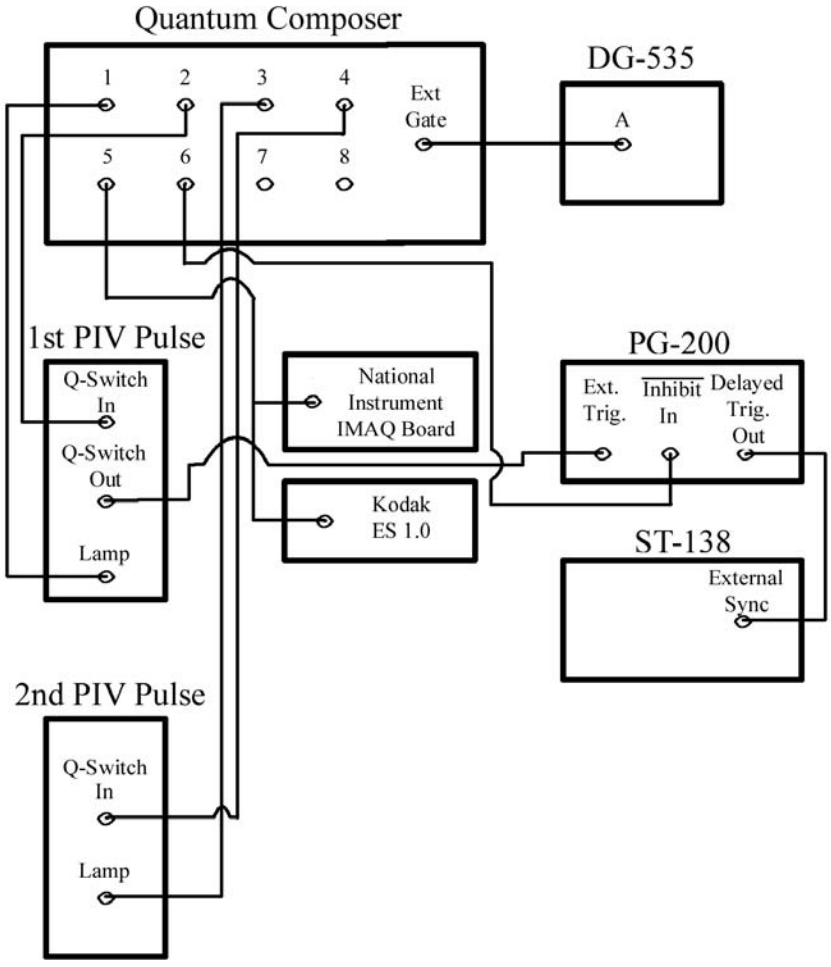

Figure 3-4 Wiring diagram for simultaneous OH-PIV measurements

The wiring diagram that allowed the precise temporal placement of acquisition events is shown in Figure 3-4. The Quantum Composer shown in Figure 3-4 is a signal generator that allowed the delivery of programmable time delayed signals, which allowed the proper temporal placement of laser pulses with acquisition events of the cameras. On the Quantum Composer, Channels 1 and 2 provided the negative going TTL pulses for the Flash Lamp and Q-switch to the Nd:Yag for the first PIV/OH pulse. Channels 3 and 4 then provided the TLL signals for the Flash Lamp and Q-switch to the Nd:Yag for the second PIV pulse. The fixed temporal spacing between the first and second PIV pulses was achieved by referencing the Flash Lamp signal of the second PIV pulse to Channel 1, which was the Flash Lamp signal for the first PIV/OH pulse. This temporal spacing between the TTL signals from Channel 1 and 3 was the set Δt between the two PIV pulses that would eventually be used to determine the velocity vector as shown in Equation 2-1. Channels 5 and 6 were then used to trigger the Kodak ES 1.0 camera and the National Instruments data acquisition board that collected the two PIV images. The Princeton Instruments PG-200, which provided the high voltage gate pulse to the ICCD, was triggered using the Q-switch output from the first PIV/OH pulse. In this way, all laser and acquisition events were referenced to the Flash Lamp signal from Channel 1 on the Quantum Composer.

In these unsteady experiments, it was necessary to place all laser and acquisition events coincident with specific temporal locations within the sinusoidally forced flow field. This was done by using the speaker oscillation as the reference for all time-delayed laser and acquisition events. This is illustrated in Figure 3-5, which shows the placement of laser and data acquisition events relative to the speaker oscillation. Once the speakers are initiated via the SRS Model

DS335 function generator, there is an arbitrary placement of the data acquisition events relative to the speaker phase.

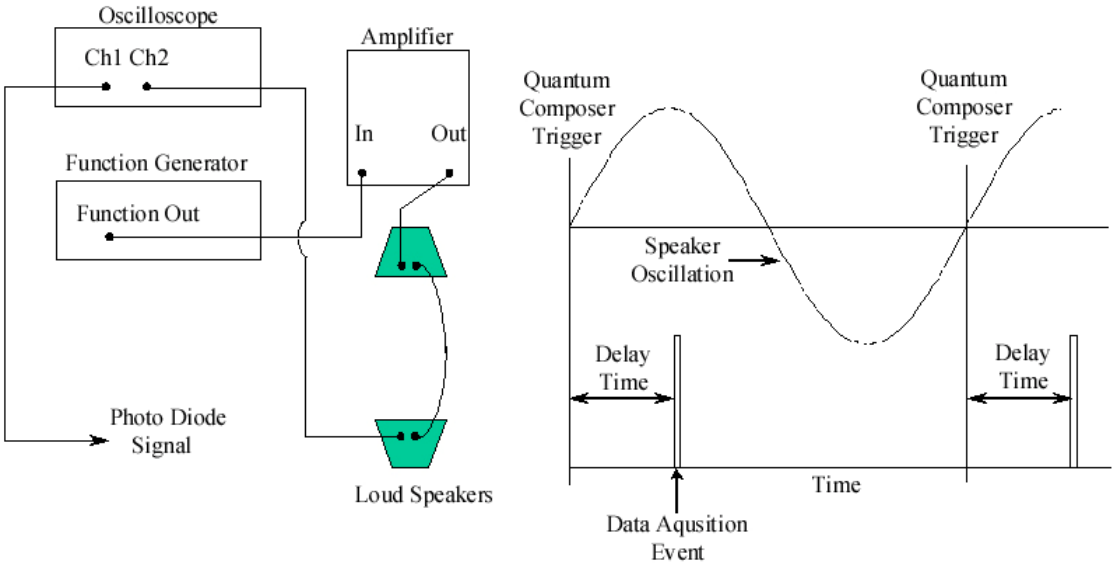

Figure 3-5 Timing events of speaker phase and data acquisitions

This relative placement was determined by collecting a signal from a photo diode, which collects scattered laser light from the first PIV/OH pulse, and the sinusoidal signal input to the speakers that cap the plenums on the counterflow diffusion flame burner. The photo diode signal or the PMT signal as will be seen in Section 3-3-2, effectively identifies the laser and acquisition events that are controlled by the Quantum composer (or the two DG-535s in Section 3-3-2) relative to the speaker oscillation. As previously stated, all laser and data acquisition events are fixed relative to the Flash Lamp signal of the first PIV/OH pulse (Channel 1). Channel 1 of the Quantum Composer is delayed relative to an internal reference T_o. By increasing or decreasing

the delay between the Flash Lamp command of Channel 1 and T_o specific placement of all laser and acquisition events can be achieved relative to different phases within the speaker oscillation.

3-3 2-λ OH Thermometry

The 2-λ OH PLIF experiments were conducted to determine the response of the reaction zone temperature to the unsteady flow field. The determination of this response is critical as reaction zone temperature affects heat release rates and the formation of pollutants such as NO_x and soot. Sections 3-3-1 and 3-3-2 describe the experimental layout as well as the timing and connections of laser systems and data acquisition systems. These experiments were much more equipment intensive and more challenging with respect to data collection and reduction relative to the other experiments conducted in this investigation.

Two setups were used to perform the 2-λ OH PLIF measurements; where the first is very similar to that which is described in Section 3-2. The second setup is almost identical with the exception that it did not allow the saturation of both OH transitions and it used two DG-535 digital delay generators in place of the Quantum Composer. Due to the fact that the second 2-λ OH PLIF setup is available for use at AERL, it will be described in Section 3-3-1 to provide instruction for future students of that lab.

3-3-1 Simultaneous 2-λ OH PLIF Measurements and Image Correction

The experimental configuration that was used to perform simultaneous measurements of spontaneous fluorescence from two different ground state populations is shown in Figure 3-6. The first pulse was provided by a Continuum Jaguar dye laser pumped by the second harmonic

of a Continuum Surelite III Nd:Yag laser. The output of this dye laser (572.8 nm) was then frequency doubled by a BBO crystal which yield an output of ~286.4 nm ($Q_1(14)$ transition). The 286.4 nm beam was then separated from the fundamental beam using a Pellin-Brocca Prism. The 286.4 nm beam is horizontally polarized and its polarization was rotated using a combination of mirrors that dropped the beams vertical height and its direction. The 286.4 nm beam then travels through a Galilean telescope that is a combination of two cylindrical lenses with f = -100 mm and f = 300 mm. The second pulse was provided from a combination of a Lambda Physik FL3002 dye laser pumped by the second harmonic of a Continuum Surelite III Nd:Yag. The fundamental output of this system provided laser light at ~565.3 nm which was then frequency doubled using a KD*P crystal to ~282.7 nm ($Q_1(5)$ transition). The 282.7 nm beam is horizontally polarized and is passed through a Galilean telescope with ocular and objective lenses of focal lengths f = -50.9 mm and f = 100 mm. The two beams were then spatially overlapped using a thin film polarizer, which selectively reflects S-polarized light (286.4 nm beam) and passes P-polarized light (282.7 nm beam). The final beam shaping lens, which both beams shared, was an f = 1.2 m cylindrical lens.

It was necessary to use two different telescopes due to the fact that the two output beams where too dissimilar with regards to the height of the beams. The widths of the beams were also dissimilar so this required the iterative adjustment of the telescope within the Lambda Physik dye laser and subsequently re-optimization of the dye laser until the beam thicknesses were approximately equal upon arrival at the final cylindrical focusing lens prior to the burner. Once these adjustments were performed, the beams entering the interrogation region of the flame were

measured to be approximately 5 mm tall by 300 μm wide with an energy of ~2 mJ/pulse, which placed the fluorescence in the linear regime.

Just prior to entering the interrogation region of the flame, a small portion of the beam (~ 4%) was redirected through a McKenna burner and the resulting fluorescence was used to tune on transition and to quantify shot-to-shot energy fluctuations.

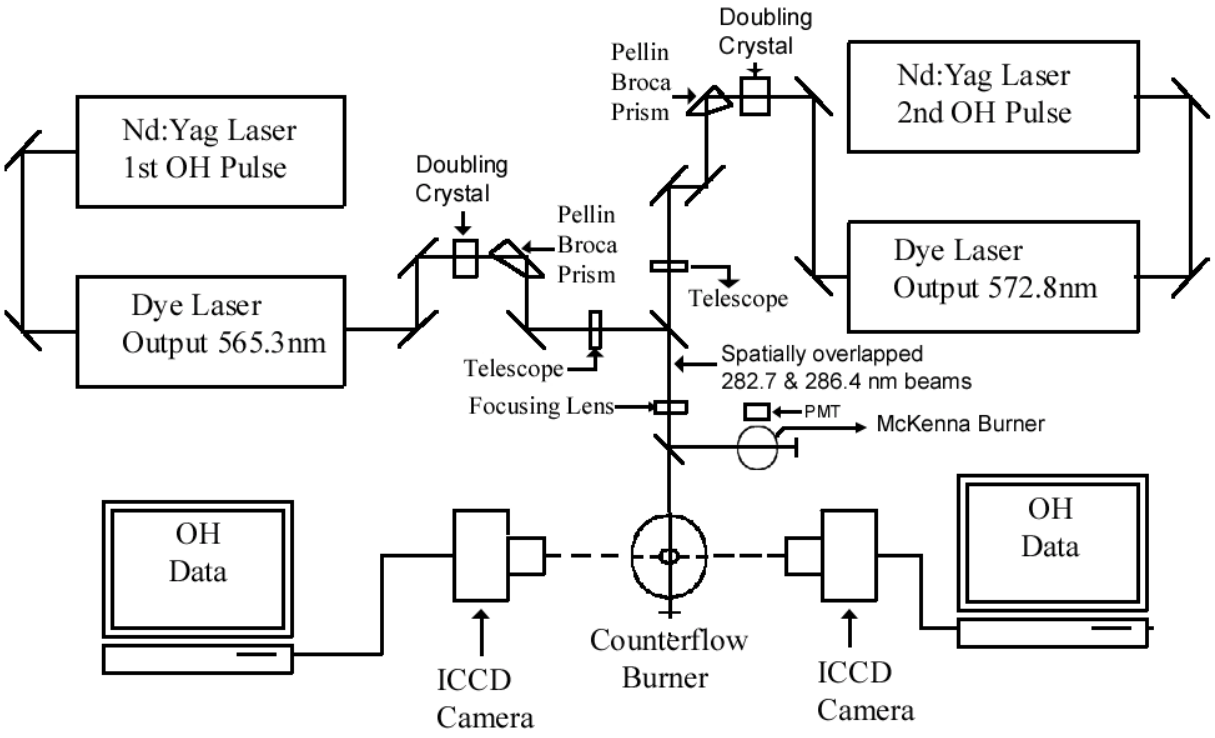

Figure 3-6 Simultaneous 2-λ OH PLIF Thermometry Setup

The Stokes shifted spontaneous fluorescence was then collected using two Princeton Instruments ICCD cameras (576x384 pixels, ~18.5 pixels/mm). Coupled to the ICCD cameras were UV grade 105 mm/f4.5 lenses fitted with UG-11 and WG-320 filters to discriminatorily

collect the OH fluorescence. This combination of filters effectively created a band pass filter centered around 340 nm and is shown in Figure 3-1.

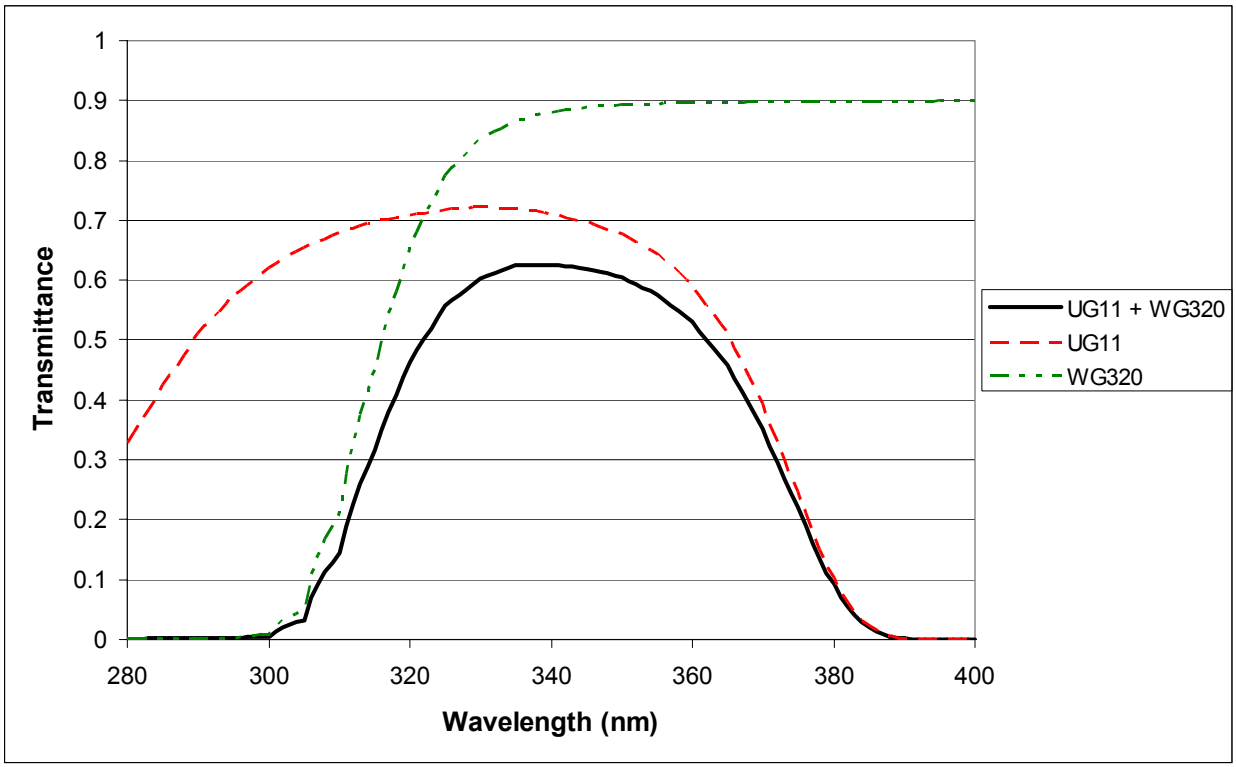

Figure 3-7 2-λ OH PLIF camera filter combination

Using the filter combination shown in Figure 3-7 effectively reduced any scattering signal from the pump beam to indistinguishable levels. In previous experiments (Santanionni et al., 2001 and Welle et al., to be submitted), a combination of UG-11 and WG305 filters were used that allowed some passage of scattered laser light although the scattered signal was ~250x smaller than the broad band fluorescence signal collected.

Using the UG-11/WG320 filter combination also further reduced the fluorescence signal collected from the (0,0) vibrational band, which has higher absorption coefficients, in favor of

the (1,1) vibrational band near 315 nm. This helps to mollify fluorescence trapping effects since at 2000 K approximately 92% of the OH radicals are in the v″=0 vibrational band. Ideally, it would be most beneficial to perform OH excitation of the (1,0) vibrational band coupled with the detection of the (1,1) band and this method has been performed (Allen & Hanson, 1986; Dyer & Crosley, 1982), but complete segregation of the two bands is not possible (Dieke & Crosswhite, 1961; Luque & Crosley, 1999).

The correction procedure for the OH-PLIF images included subtraction of a background flame emission image from the raw image, which was then followed by the division of an image that corrected for flat-field and vertical fluctuations of the energy profile of the beam. This correction procedure is illustrated in Equation 3-1.

Equation 3-1 OH-PLIF image correction procedure

$$\text{Image}_{Corrected} = \left(\text{Image}_{Raw} - \text{Image}_{FlameEmisson\,\&\,DarkCurrent}\right) \Big/ \text{Image}_{\text{LaserSheet \& Flatfield}}$$

The image that accounted for the laser sheet profile as well as flat field effects was constructed by collecting Raleigh scattering from the exit fuel stream. This inelastic scattering process is linear with the input energy of the beam and therefore once normalized facilitated the correction for the laser sheet profile and the flat-field correction simultaneously.

Without correction of flat-field variations of the ICCD camera, significant errors can result and lead to possible misinterpretation of observed phenomenon. Figure 3-8 shows the

column averaged result of the normalized flat-field image for the Princeton Instruments ICCD camera with the Thompson intensifier chip, which is connected to the ST-130 and Macintosh computer. It is obvious that significant apparent signal reduction can occur due to the intensification drop of up to ~30% in the center of the intensifier chip. In the PLIF/LII experiments, the laser sheet propagation is coincident with increasing horizontal pixel location, as depicted in Figure 3-8. Unfortunately, this general profile of the flat-field is oddly similar to a situation of linear fluorescence decay coupled with strong absorption/trapping of the spontaneous fluorescence in a symmetric flame, which is what is being studied here. The flat-field for the second Princeton Instruments ICCD camera, which has an EEV chip (ST-138 coupled to a PC), only showed flat-field fluctuations of less than 5% throughout the entire array and there were no notable trends in the intensifier variations.

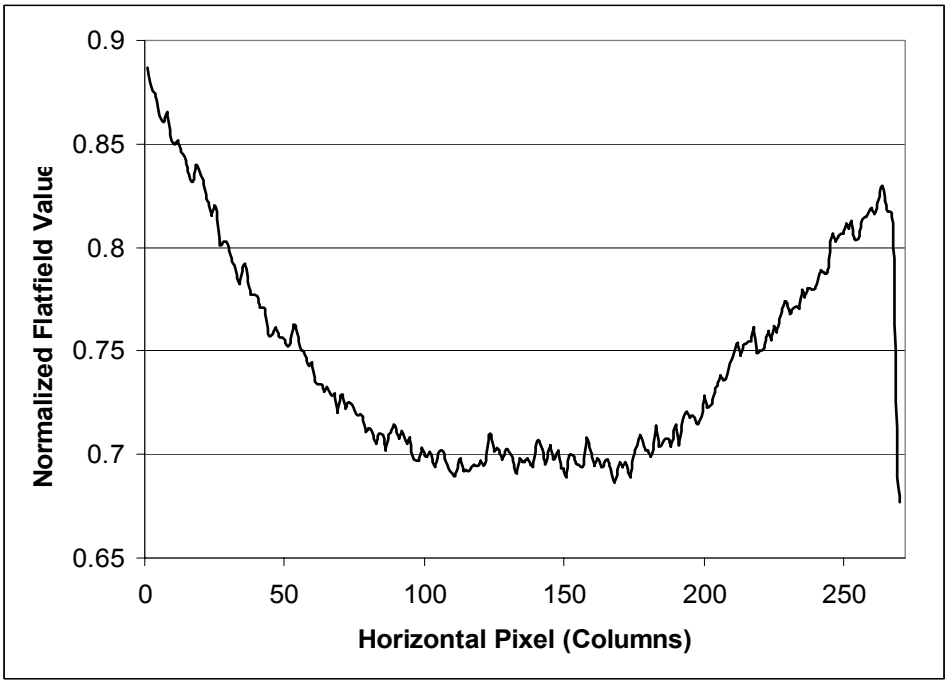

Figure 3-8 Column averaged, normalized flatfield plot for Thompson Chip (Macintosh based camera)

Once the above mentioned corrections were performed, the ratio of the images was then calculated. These 2D ratio fields were then related to temperatures using a relationship that expressed temperature as a function of image ratio. The T(ratio) functional relationship was derived from a calibration flame. It should be noted that no corrections for beam absorption were performed as this trend was not distinguishable. This can be argued to be a result of the flame being thin (only needing 12.7 mm of the flame to determine reaction zone temperatures of the centerline stagnation streamline). Also, taking the ratio helps to further mitigate these effects as the Einstein B (absorption) coefficients for the two transitions are very similar ($B_{Q1(5)}/B_{Q1(14)} \approx .90$).

Each reported data point from the first set of temperature measurements (collected at WP AFB), which were in the saturation regime, was an average of 20 shots. In the second set of data (collected at AERL), which was in the linear fluorescence regime, each data point was a result of a 40 shot average.

3-3-2 Timing and Wiring

Figure 3-9 shows the necessary connections between the laser systems, integrating boxcars, and camera systems to perform the simultaneous 2-λ OH PLIF thermometry measurements. This experiment requires much more equipment and consideration with respect to timing and monitoring issues. This is primarily a result of the need to constantly monitor and tune the doubling crystals as well as checking to verify that the dye lasers have not drifted off peak transition.

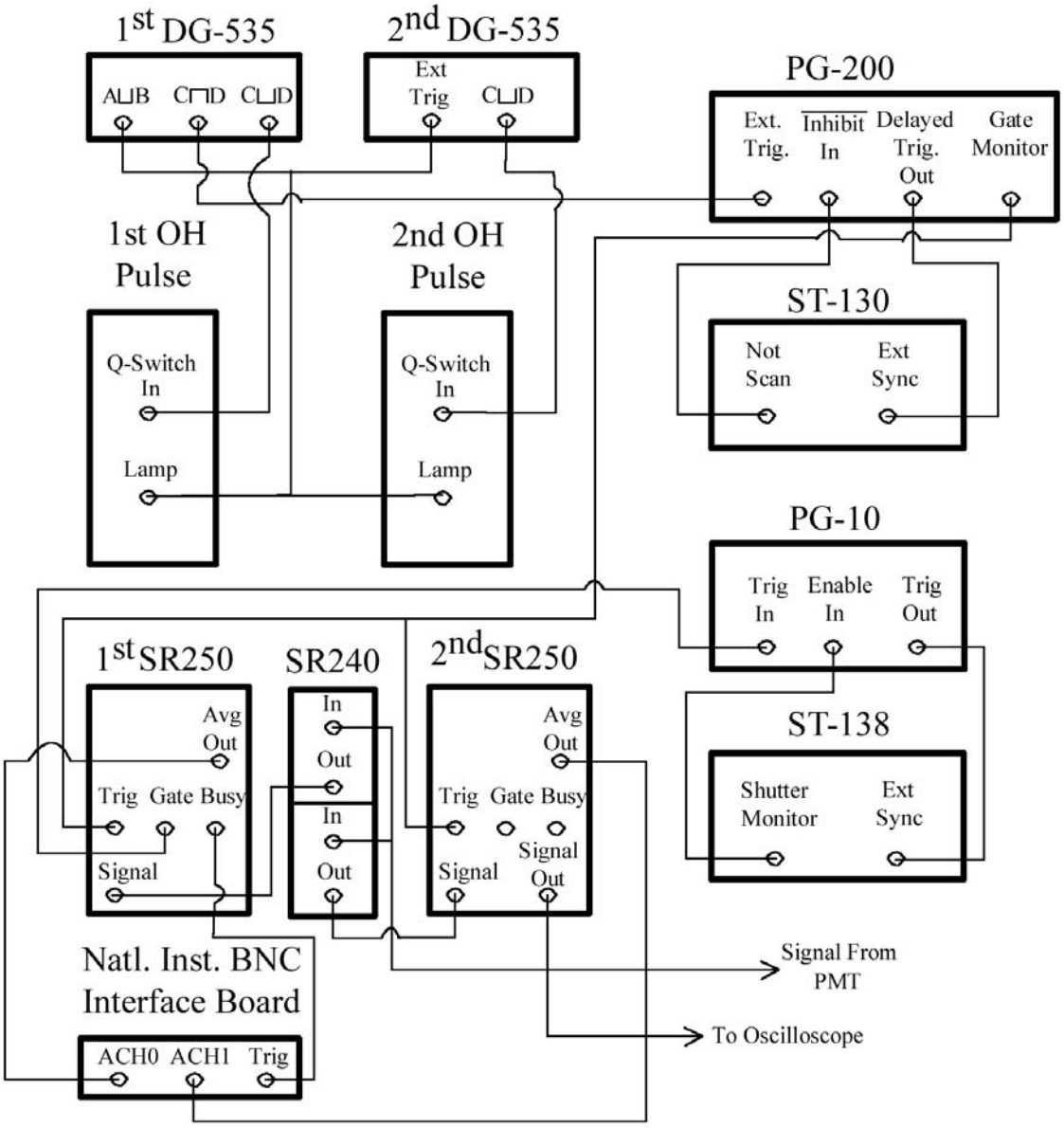

Figure 3-9 Wiring diagram for simultaneous 2-λ OH PLIF thermometry

In this experiment, two DG-535s were used instead of a Quantum composer to control all timing issues. The first DG-535 provided the Flash Lamp signal for both Nd:Yag laser systems

from the negative going TTL channel AB. The output from this channel was also used to trigger the second DG-535. Then the second negative going TTL signals (CD) from the DG-535s were used for the Q-Switch signal to the two Continuum Surelite IIIs. The temporal displacement between the two laser pulses was achieved by increasing the Q-Switch delay of the second laser pulse, controlled by the second DG-535, by 600 ns. This resulted in a delay of 600 ns between the second OH pulse, which came from the Lambda Physik FL3002 dye laser, relative to the first OH pulse, which came from the Continuum Jaguar Dye laser.

The first DG-535 also provided the trigger for the PG-200, which in turn triggered the ST-130 and collected the first fluorescence event. The 1 MΩ gate monitor signal from the PG-200 was then used to trigger the first SR250. The first SR250 boxcar integrator then collected a 5x amplified signal from the PMT, which collected fluorescence from the porous plug burner. The 5x amplification was achieved by first passing the PMT signal through a SR240.

The trigger for the PG-10, which collected the second fluorescence event, was received from the gate signal of the first SR250. Upon receiving a trigger from the first SR250, the PG-10 then triggered the ST-138 so the second fluorescence event could be collected.

The gate monitor signal from the PG-200 also triggered the second SR250. A delay of 600 ns was programmed into the second SR250 so it would collect the 5x amplified signal from the second PMT fluorescence event so shot-to-shot energy and wavelength fluctuations could be quantified.

The National Instruments BNC interface board and data acquisition card were triggered using the busy signal from the first SR250. The two integrated outputs were then collected from

the two SR250s and digitized. The signals were collected and saved using a Labview VI, which is illustrated in Appendix 1.

The temporal positioning of the laser pulses and data acquisition events relative to temporal locations within the speaker oscillation were achieved by monitoring the signal out from the second SR250 relative to the speaker oscillation. This setup is identical to that depicted in Figure 3-5 except the signal out from the second SR250 replaces the photo diode signal. Also as before, all triggering events were referenced to the negative going TTL signal of channel AB of the first DG-535. It was then only necessary to increase or decrease the delay of this trigger relative to an internal T_o reference to shift to positioning of the data acquisition events throughout the speaker oscillation.

Due to the complexity of this experiment, a timing diagram is presented in Figure 3-10. This figure illustrates the relative timing of the triggering events of the various laser systems, boxcar integrators, and camera systems. The gate opening events of the two ICCD cameras occurred just prior to the passage of the pump beams through the interrogation region. The gate widths were set to 200 ns and as seen in Figure 3-10, the spacing between the openings of the two camera gates was 600 ns, which resulted in a time delay of 400 ns between the closing of the first camera gate and the opening of the second camera gate. The 600 ns spacing was more than sufficient to ensure no fluorescence signal was collected from the first fluorescence event during the second camera gate.

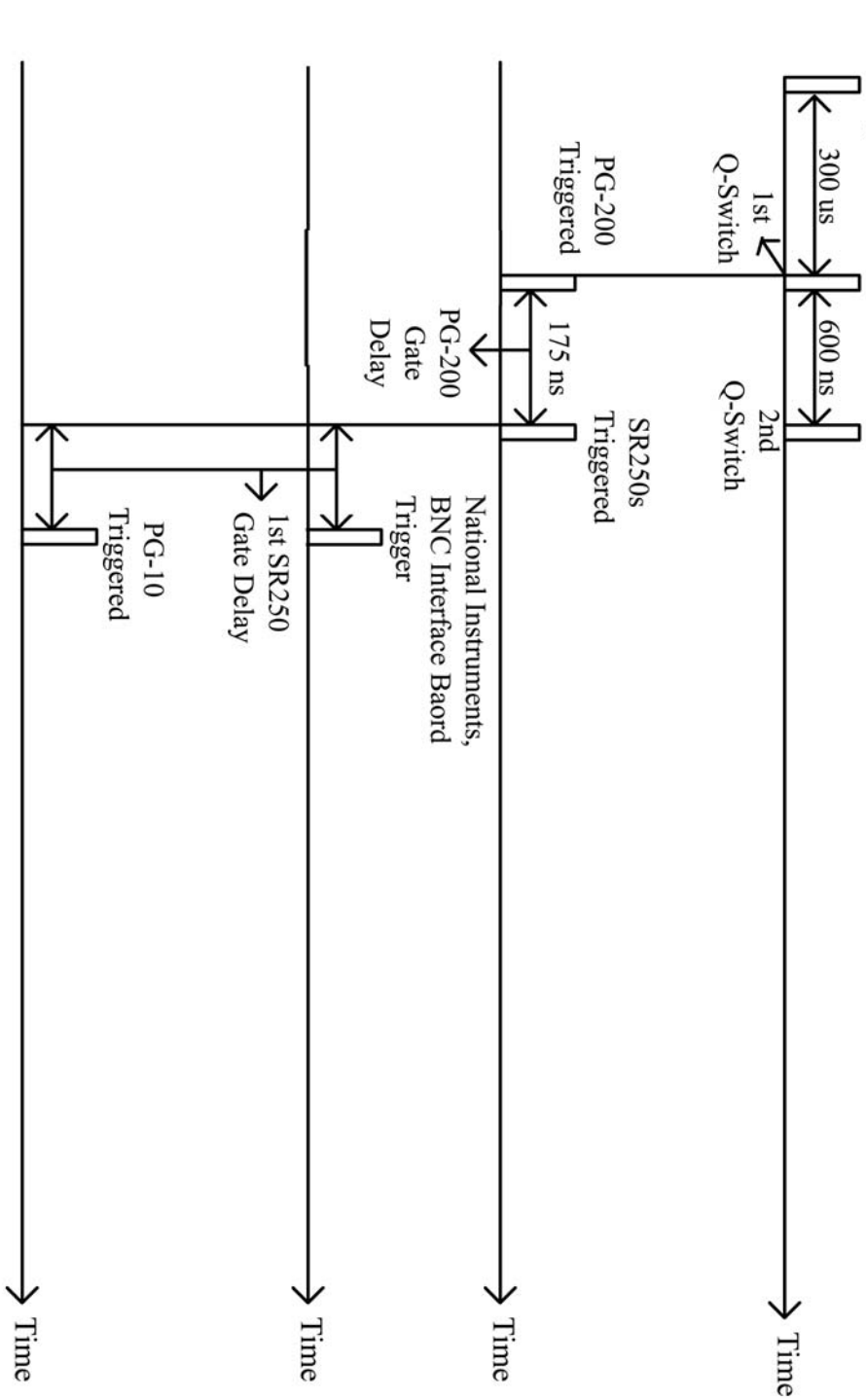

Figure 3-10 Timing diagram for 2-λ OH measurements

3-4 Laser Induced Incandescence

Laser Induced Incandescence (LII) measurements were performed to qualitatively describe the soot field response to the unsteady flow field. Extinction measurements were not performed in this effort so quantitative soot volume fraction values were not determined, but LII is useful in the way that it allows spatially and temporally resolved relative comparisons. Section 3-4-1 describes the experimental setup used to execute the experiments and Section 3-4-2 describes the wiring of the equipment and timing.

3-4-1 LII Experimental Layout

The experimental layout for the LII experiments is illustrated in Figure 3-11. These experiments were performed using the first harmonic (1064 nm) of a Continuum Surelite III Nd:YAG laser. The first harmonic of the beam was used to avoid exciting the polycyclic aromatic hydrocarbons (PAH) that are nearly spatially coincident with the soot field. The PAH fluorescence signal is many times stronger than the incandescence signal so if not properly filtered or excitation avoided, the PAH fluorescence can cause considerable systematic error in the measurements.

Due to the minimal amounts of energy needed for this experiment, ~10% of the output 1064 nm beam was reflected down the optical path. The energy was modulated using a combination of a 1064 nm $\lambda/2$ wave plate and a polarizing beam splitter (PBS). The PBS preferentially transmits P-polarized light and reflects S-polarized light with an extinction ratio of

1000:1. As a result, the amount of energy was easily modulated by adjusting the amount of P-polarized light present using the λ/2 wave plate.

The final beam shaping optic was an f = 1.2 m cylindrical focusing lens. This long focal length lens helped to minimize beam size changes through the 25.4 mm interrogation region. This optical system resulted in a beam approximately ~7.9 mm in height and ~210 μm thick. The amount of energy used for each pulse was ~8.2 mJ which resulted in an energy density of ~ 0.49 J/cm^2. This energy density was chosen to reduce significant amounts of vaporization of smaller soot particles. This is especially important in a CFDF since the size distribution present in the interrogation region at any given time includes the primary particles of ~50 nm up to the larger fractal like soot agglomerates.

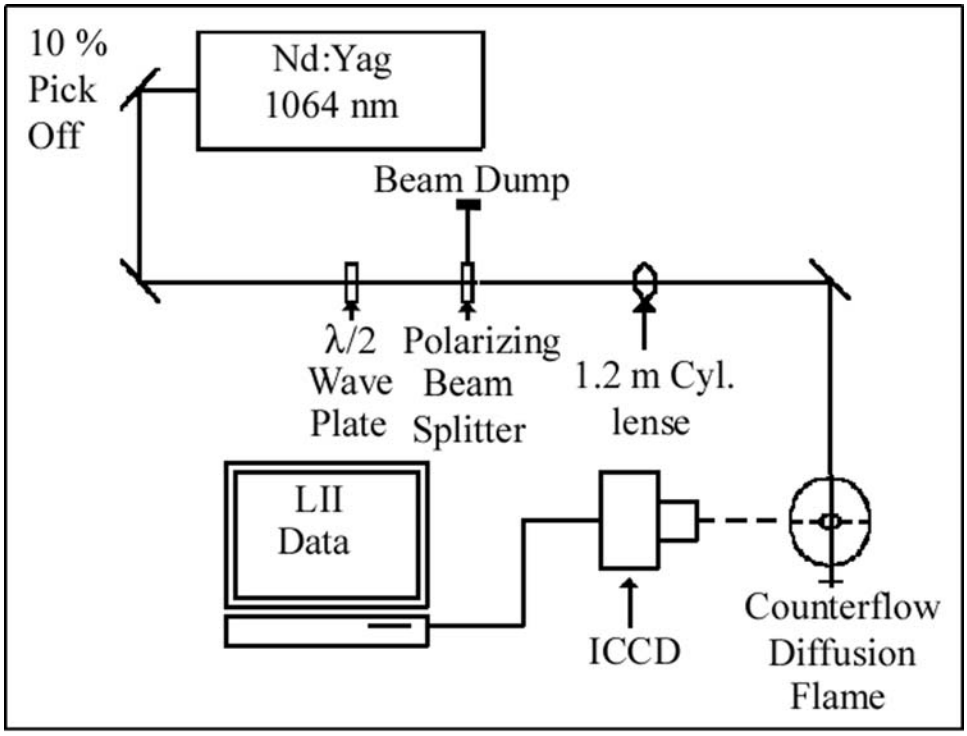

Figure 3-11 Laser induced incandescence experimental layout

The incandescence signal from the heated soot particles was then collected using a Princeton Instruments ICCD camera (576x384 pixels, ~19 px/mm). Coupled to the ICCD camera was a UV grade 105 mm/f4.5 lens fitted with a Melles Griot filter to discriminatorily collect the incandescence signal. The Melles Griot filter was centered at 400 nm with a band pass of 80 nm.

The image correction procedure was very simplistic since extinction measurements were not performed to relate the signal strength to soot volume fraction (f_{sv}).

Equation 3-2 LII Image correction procedure

$$\text{LII\_Image}_{\text{Corrected}} = \left(\text{LII\_Image}_{\text{Raw}} - \text{Image}_{\text{Background}}\right) \Big/ \text{Image}_{\text{Laser Sheet Profile}}$$

Basically, a background image was subtracted from the raw image and then a normalized laser sheet profile image was divided into the image to correct for vertical energy fluctuations of the beam. The laser sheet profile was determined by collecting thermal radiation emitted from a target placed in the interrogation region of the flame.

At each temporal location, 50 images were collected and averaged. The shot-to-shot energy fluctuations were quantified by collecting a reflected portion of the beam and integrating it using the SR250 boxcars. Due to the stability of the laser system, these corrections were very small. In fact, when the energy fluctuations of the laser were monitored over a 10 minute time frame, the fluctuations were less than 3% and were not monotonically increasing or decreasing. The stability of the Continuum Surelite III was found to be very reliable.

3-4-2 Timing and Wiring

The wiring for the LII experiments is very similar to the previous experiments and is illustrated in Figure 3-12. A DG-535 digital delay generator was used to provide the TTL signals to the Nd:YAG laser for the laser events. The DG-535 was also used to trigger the PG-200 pulse generator, which in turn triggered the ST-130 controller.

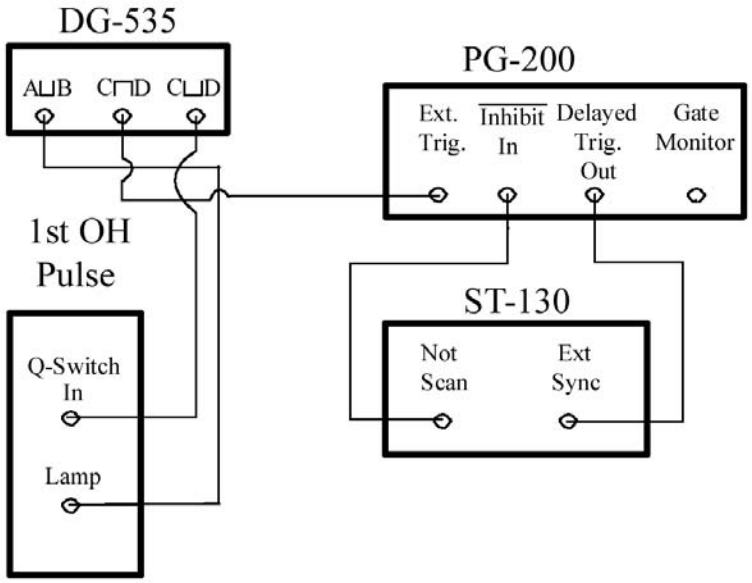

Figure 3-12 Wiring diagram for LII measurements

In the same way as the simultaneous PIV/OH measurements, scattering from a turning mirror was collected using a photo diode and the signal was digitized using an oscilloscope along with the speaker oscillation trace. In this way the firing command (negative going AB TTL) to the laser could be delayed so proper temporal placement of the laser and acquisition events could occur within the speaker oscillation.

The opening of the camera gate was coincident with the passage of the laser pulse through the interrogation region. This afforded higher signal-to-noise ratios and is called prompt acquisition. The camera gate width was set to 30 ns so as not to bias the measurements to larger particles. The possible biasing with longer gate widths is a result of smaller particles having larger surface to volume ratios and thus cooling quicker and subsequently the signal decays faster.

3-5 Experimental Conditions

The experiments performed in this investigation were intended to mimic the conditions present in an unsteady reacting flow-field. Before performing measurements, the unforced global strain rates (GSR) were quantified by using the following relationship illustrated in Equation 3-3, which is the strain rate for an isothermal potential flow.

Equation 3-3 Unforced steady strain rate relation

$$K = \frac{2 \cdot V_{Air}}{L}$$

In Equation 3-3, K is the strain rate, V_{air} is the air velocity at the exit of the upper reactant tube of the counterflow diffusion flame burner and L is the separation distance between the reactant tubes. When a steady strain rate value is reported (SSR), this signals that the reported strain rate value was determined from velocity field measurements. The fuel and the air gas streams were

momentum matched and for an isothermal flow, the stagnation plane would be in the center of the gap between the two reactant tubes. The flow controllers were calibrated using DryCal DC-2M positive-displacement volumetric flow meter, which is NIST traceable (DryCal documentation). The necessary flow rates, as determined by the momentum matching of the flows, and the corresponding flow meter settings, which are determined after calibration were calculated using a MathCAD document and are illustrated in Appendix 2.

The frequencies and amplitudes that were studied in this investigation are reported in Table 3-1. In a turbulent reacting flow field, there is a wide range of eddy length and time scales. The idea of this investigation was to simulate the characteristic times scales by varying the flow-field frequency. The length scale is set by the reactant tube exit diameters and the different amplitudes represent different turbulence intensities. Although not shown in Table 3-1, a limited number of experiments were also conducted at a forcing frequency of 500 Hz.

Table 3-1 Peak-to-Peak voltage set on the signal generator for each unsteady case

	Forcing Amplitude (V_{p-p} on signal generator)					
Freq	SSR 30 s^{-1}		SSR 60 s^{-1}		SSR 90 s^{-1}	
(Hz)	A_1	A_2	A_1	A_2	A_1	A_2
30	0.15	0.25	0.15	0.3	0.28	0.56
50	0.15	0.5	0.15	0.3	0.35	0.7
100	0.15	0.75	0.15	0.3	0.50	1.0
200	0.15	1.5	0.15	0.3	0.28	0.56

In Table 3-2 and Table 3-3, the strength of these amplitude oscillations is described in terms of their strength relative to flow reversal and extinction as previously determined (DeCroix, 1998).

Table 3-2 Forcing amplitude denoted as A1 as a fraction of the flow reversal and extinction voltages and the resulting amplitude of the velocity fluctuation

	Forcing Amplitude A_1											
Freq	GSR 15 s^{-1}			GSR 30 s^{-1}			GSR 60 s^{-1}			GSR 90 s^{-1}		
(Hz)	$\frac{V}{V_{rev}}$	$\frac{V}{V_{ext}}$	$\frac{U_{max}}{U_{steady}}$	$\frac{V}{V_{rev}}$	$\frac{V}{V_{ext}}$	$\frac{U_{max}}{U_{steady}}$	$\frac{V}{V_{rev}}$	$\frac{V}{V_{ext}}$	$\frac{U_{max}}{U_{steady}}$	$\frac{V}{V_{rev}}$	$\frac{V}{V_{ext}}$	$\frac{U_{max}}{U_{steady}}$
25	1.0	0.38	---	1.0	0.25	1.7	0.50	0.13	0.7	0.50	0.17	0.6
50	1.0	0.17	---	1.0	0.15	0.9	0.50	0.08	0.4	0.50	0.17	0.8
100	1.0	0.06	---	1.0	0.05	0.8	0.50	0.05	0.3	0.50	0.14	0.6
200	1.0	0.06	---	1.0	0.05	1.0	0.50	0.05	0.4	0.50	0.10	0.5

Table 3-3 Forcing amplitude denoted as A2 as a fraction of the flow reversal and extinction voltages and the resulting amplitude of the velocity fluctuation.

	Forcing Amplitude A_2											
Freq	GSR 15 s^{-1}			GSR 30 s^{-1}			GSR 60 s^{-1}			GSR 90 s^{-1}		
(Hz)	$\frac{V}{V_{rev}}$	$\frac{V}{V_{ext}}$	$\frac{U_{max}}{U_{steady}}$	$\frac{V}{V_{rev}}$	$\frac{V}{V_{ext}}$	$\frac{U_{max}}{U_{steady}}$	$\frac{V}{V_{rev}}$	$\frac{V}{V_{ext}}$	$\frac{U_{max}}{U_{steady}}$	$\frac{V}{V_{rev}}$	$\frac{V}{V_{ext}}$	$\frac{U_{max}}{U_{steady}}$
25	1.3	0.50	---	1.7	0.42	2.8	1.0	0.26	1.4	1.0	0.34	1.1
50	2.9	0.50	---	3.3	0.50	3.0	1.0	0.15	0.8	1.0	0.34	1.6
100	8.3	0.50	---	5.0	0.25	4.0	1.0	0.10	0.6	1.0	0.28	1.2
200	8.3	0.50	---	10	0.50	10	1.0	0.10	0.8	1.0	0.20	1.0

4 Simultaneous PIV and OH-PLIF Measurements in an Unsteady Counterflow Propane-Air Diffusion Flame

Abstract

To study the transient response of a diffusion flame to an unsteady flow-field, quantitative measurements of velocity, using Particle Image Velocimetry (PIV), and OH measurements, using Planar Laser Induced Fluorescence (PLIF), were made simultaneously in an oscillating counterflow diffusion flame. These non-intrusive measurements were performed to spatially and temporally resolve flow-field and flame characteristics as a function of initial steady strain rate and forcing frequency. For the forcing frequencies considered in this study, the strain rate fluctuations were found to lag the velocity fluctuations, but the phase difference decreased with increasing forcing frequency. At lower forcing frequencies, the width of the OH field responded quasi-steadily, but as the forcing frequency increased, the OH field showed transient effects. The dilatation velocity, defined as the difference between the minimum velocity in the preheat zone and the maximum velocity in the reaction zone, was used as a flame temperature indicator. The dilatation velocity revealed that the phase difference between the velocity and the temperature increased with increasing forcing frequency, confirming the existence of a "diffusion limited" response. The results presented here help to illuminate the interconnecting relationships between the chemistry, fluid dynamics and reactant transport times.

Introduction

Turbulent diffusion flames are of particular interest because of their presence in most practical combustion devices. Flamelet theory is a method that characterizes turbulent diffusion flames as a collection of strained, laminar, one-dimensional flamelets [1,2], which are solely dependent upon the mixture fraction and instantaneous scalar dissipation rate. The flamelets are assumed to respond quasi-steadily to the unsteady strain rates of the turbulent flow-field. Recent computational and experimental studies, however, have shown that conditions exist where this assumption is invalid [3-6]. If the turbulent Reynolds number is sufficiently large, there exists a range of eddy sizes where the characteristic turnover time of the smallest eddies is comparable to the diffusion time of the laminar flamelet [3]. The large-scale eddies establish the magnitude of the mean strain rate, while the fluctuations around this mean value are caused by the smaller eddies. These conditions can lead to a wide range of characteristic frequencies [4]. Thus, it is necessary to investigate the frequency response of flamelets in an attempt to extend the applicability of the flamelet theory.

The purpose of this investigation was to quantify the strain rate and relative OH concentration fluctuations in a propane-air flame subjected to velocity fluctuations. A counterflow diffusion burner was used because it has the same scalar structure as a flamelet in the mixing zone of a turbulent reacting flow-field [1]. PIV measurements were used to quantify the velocity, strain rate, and phase angle relationships between measured parameters as a function of velocity oscillation frequency. Simultaneously, the OH field was measured using

PLIF. Reaction zone thickness as measured by the width of the OH field, rather than OH concentration, is presented in this paper.

Experimental Apparatus and Procedure

A schematic of the counterflow diffusion flame burner used in this study is shown in Figure 4-1. The burner is a modification of the design described by Puri and Seshadri [7], and described in detail in [8]. Briefly, the oxidizer and fuel tubes are 25.4·mm in diameter and have a 12.7·mm separation distance. Plenums located on the fuel and oxidizer sides are capped with 20·cm loudspeakers, which impose the velocity fluctuations and are driven by an amplified signal generator.

An unsteady flow-field was imposed on the counterflow diffusion flame by inputting a sinusoidal voltage signal to the speakers. The velocity and relative [OH] measurements were made as a function of initial steady strain rate (SSR) and forcing frequency. These measurements were made at four temporal locations within the sinusoidal voltage oscillation applied to the speakers: the zero amplitude with positive slope (0+), maximum amplitude (Max), zero amplitude with negative slope (0-), and minimum amplitude (Min). The forcing frequencies considered in this study were 30, 50, 100, and 200·Hz. A weak forcing amplitude was applied to the flow; Table 4-1 defines this amplitude relative to flow reversal and extinction as previously measured [8].

Figure 4-2 is a schematic of the PIV-OH measurement system. The PIV measurements were made using two frequency doubled Nd:YAG lasers (λ = 532·nm); in the probe region, the thickness of the two sheets were set to 500·μm with a height of·20 mm. Hollow zeospheres, having a mean diameter of 2.2·μm, were used to seed the airflow. The PIV images were recorded using a Kodak interline-transfer digital camera (1008x1012 pixels) fitted with a 105·mm lens, using an f stop of 8. An interference filter centered on 532·nm with a FWHM of 3·nm was used to block background flame emission. Interrogation regions composed of 64 pixel squares (0.9·mm x 0.9·mm) with 75% overlapping were employed for the velocity measurements. Custom software including a cross correlation algorithm was used to derive the velocities.

The OH measurements were made using a Nd:YAG pumped dye laser, which was running Rhodamine 590 dye, and the output of which was frequency doubled down to ~282·nm, yielding a 10·ns pulse of approximately 10·mJ in a sheet of approximately 300·μm in width and 20·mm in height. The $R_1(8)$ transition of the $A^2\Sigma+ \leftarrow X^2\Pi(1,0)$ band was excited, partially saturating the transition, and detected using a Princeton Instruments ICCD camera. The $R_1(8)$ transition was chosen because of its reduced sensitivity to temperature fluctuations; indeed, the maximum OH concentration varied by less than 5% from the average cycle value for any of the experimental conditions. A 105·mm/f4.5 lens fitted with UG-11 and WG-295 filters was used to collect the OH fluorescence.

The response of the reaction zone to velocity oscillations was characterized by measuring the full width at half maximum (FWHM) of the OH field. The strain rate was determined by

evaluating the gradient of the axial velocity profile at the centerline of the burner on the oxidizer side of the stagnation plane. The centerline velocity was determined by averaging the three closest velocity vectors on both sides of the centerline that were at the same axial distance from the air tube exit. This averaged the velocity over 1.16·mm in the transverse coordinate at each axial position, which was less than 5% of the air tube exit diameter. A line was fit to the velocity data prior to the preheat zone and the strain rate was then calculated from the fitted line. The location of the fitted line relative to the preheat zone is illustrated in Figure 4-3. Twenty OH and PIV images were taken and averaged at each of the four temporal locations within the speaker oscillation. No corrections for thermophoretic effects have been performed on the velocity measurements, as previous studies have shown that accurate velocity measurements can be performed prior to the preheat zone without accounting for thermophoresis [9].

Results and Discussion

Due to the stoichiometry in a counterflowing propane-air diffusion flame, the flame is located on the airside of the stagnation plane. The transport of fuel is a result of diffusion, while the transport of oxidizer to the flame is a result of convection and diffusion. This convective-diffusive coupling on the airside effectively links the chemistry of the flame with the flow-field dynamics. A flame that is subject to a cyclical velocity field, with a characteristic cycle time much greater than that of any of the relevant transport times of the flame, should respond in a quasi-steady manner. As the characteristic cycle time of the velocity fluctuations decreases and

approaches the relevant transport times of the flame, unsteady or transient characteristics in the flame behavior begin to appear.

The measured strain rates and FWHM of the OH field for an initial SSR of $74 \cdot s^{-1}$ are plotted in Figure 4-4 at the four temporal locations in the speaker oscillation for all four forcing frequencies. At a forcing frequency of 30·Hz, the instantaneous strain rate continuously increases from the temporal locations of 0+ to 0-, as seen in Figure 4-4a. During this period, the OH field narrows continuously. Between the 0- and Min locations, the instantaneous strain rate decreases and the OH layer thickens. It was also found that when the instantaneous strain rate for the forced flames was above the steady strain rate, the OH field was thinner than the steady case. The converse of this was also found to be true. The strain rate and OH field behavior at a forcing frequency of 50·Hz mimicked the behavior found at 30·Hz, as seen in Figure 4-4b. If the flame were responding steadily, increasing the strain rate would be accompanied by an increase in the convective velocities at the edge of the convective-diffusive zone of the flame. With this elevated supply of cool reactants, the flame would move closer to the stagnation plane, due to stoichiometry, and the flame would also cool and become thinner. Thinning of the flame with increasing strain rate has been found previously in experimental and numerical studies [10,11]. Thus, from Figure 4-4 a and b, the OH field, and hence the flame, is responding to the instantaneous strain rate in a quasi-steady manner, at forcing frequencies of 30 and 50·Hz. Note that cyclic behavior of the OH concentration has been found previously in a N_2 diluted methane-air flame [6].

As the forcing frequency was increased to 100 Hz, the strain rate was found to increase continuously between the temporal locations of 0+ and 0- and then decreased between the locations of 0- and Min, as seen in Figure 4-4c. This is similar to the behavior found for lower-frequency oscillations. The OH field width was found to increase between the temporal location of 0+ and Max and then decreased continuously between the Max and Min locations. Thus, for the 100·Hz case, between the 0+ and Max locations, there is an increase in the instantaneous strain rate that is accompanied by an increase in the width of the OH layer. Also, between the 0- and Min locations, a decrease in the instantaneous strain rate is accompanied by a decreasing width of the OH layer. Similar behavior was also noted when the forcing frequency was increased to 200 Hz, which is shown in Figure 4-4d. At 200·Hz, the strain rate decreased between 0+ and Max and then continuously increased between the Max and Min temporal locations. The OH field width increased between the locations of 0+ and 0- and then decreased between 0- and Min. Between the Max and 0- locations, there is an increasing strain rate and an increasing OH field width. Thus, the OH field does not respond quasi-steadily to the instantaneous strain rate at forcing frequencies above 100·Hz.

As illustrated in Figure 4-4, the maximum strain rate occurs at the 0- temporal location for the 3 lower frequencies, but at the Min location for the 200·Hz case. Although a frequency dependant phase angle relationship between the strain rate and width of the OH field seems apparent, it cannot be directly deduced from Figure 4-4. This is due to a frequency dependant phase angle that exists between the speaker motion and the applied voltage [8]. Although only four temporal locations were measured for each flame condition, phase-angle relationships were

still resolvable with this limited temporal sampling. Because the speakers are oscillating in a sinusoidal manner, previous studies have shown that parameters dependent upon their motion, such as the air exit velocity, respond similarly [6,8,12]. The measured results of the velocity, strain rate, and the OH field were fitted to an offset sine function, as shown by Equation 1, to determine phase angle relationships.

$$V = V_0 + V_1 \cdot \sin(\omega \cdot t + V_2) \qquad (1)$$

Here, V_0 is an offset value, V_1 is half the peak-to-peak difference, V_2 is the phase difference, t is the temporal location in the oscillation, and ω is equal to $2\pi f$, where f is the forcing frequency. The parameters V_0, V_1, and V_2 were determined from the measured data.

Figure 4-5 shows a typical plot of the normalized measured velocity and strain rate with the corresponding fitted curves plotted versus time for a forcing frequency of 50·Hz. Subtracting V_0 and then dividing by V_1 normalizes the measured data and fitted curves. Good agreement was found between the measured data and the fitted sine functions. The velocity measurements reported in Figure 4-5 correspond to the closest point to the flame that was not affected by heat release. This location was used because the relevant marker of the flow-field exists in the region where strain rate is measured instead of the nozzle exit [12]. This is a result of a phase difference between the air exit velocity and the velocities just prior to the preheat zone. As can be seen in Figure 4-5, the strain rate is lagging the velocity. Under isothermal conditions or cyclic oscillations which have cycle times much longer than relevant transport times of the flame, the velocity and the strain rate will be in phase. Figure 4-6 shows the phase angle relationship between the velocity and strain rate as a function of frequency for steady strain

rates of $23 \cdot s^{-1}$, $44 \cdot s^{-1}$, and $74 \cdot s^{-1}$. For all strain rates, the phase difference between the strain rate and the velocity is decreasing as the forcing frequency is increased from 30 to 200·Hz. Egolfopoulos and Campbell [4] performed a detailed numerical study of the frequency response of counterflowing strained diffusion methane/oxygen/nitrogen flames. For a flame with a mean strain rate of $400 \cdot s^{-1}$, they found the strain rate was in phase with the velocity for forcing frequencies below 10·Hz. Above forcing frequencies of 10·Hz, a phase difference was present between the strain rate and the air exit velocity, which reached a maximum and then began to decay back to zero as the forcing frequency continued to increased. The phase difference between the velocity and the strain rate was found to be induced by a systematic increase in a lag between the velocity and thermal expansion, which follows the phase shifted maximum cyclic temperature. The magnitudes of the oscillations in maximum temperature were also found to decrease as the forcing frequency increased. Sensitivity of strain rate to thermal expansion has been observed and investigated in previous studies [10,13,14]. Experimental results of the phase difference between velocity and strain rate presented in this study support the numerical results of Egolfopoulos and Campbell [4].

Figure 4-6 also illustrates that, generally, the phase difference between the velocity and strain rate is decreasing with decreasing initial steady strain rate. Increasing mean strain rates result in increased mean velocities at the edge of the convective-diffusive zone on the air side and thereby reduce the diffusive time necessary for the oxidizer to be transported to the reaction zone. Consequently, higher forcing frequencies will be necessary to induce a phase difference. An analogy has been presented between the attenuation of spatial gradients in viscosity for

Stoke's second problem and the attenuation of spatial gradients of reactants with increasing forcing frequency [4]. With increasing strain rate, the frequency at which phase-shifted temperature (thermal expansion) effects decrease their influence on the strain rate will increase. Ultimately, this means an increasing strain rate should shift the location where the phase difference of the strain rate becomes non-zero, reaches a maximum, and decreases back to zero to higher forcing frequencies. The general trends shown in Figure 4-6 support this description.

A flame temperature marker was derived to help confirm the phase shifting behavior of the maximum temperature. Although no corrections for thermophoretic forces have been made to the velocities in the heat release zone, the difference between the maximum velocity in the reaction zone and the minimum velocity in the preheat zone, as shown in Figure 4-3, was used as an indicator of the flame temperature. The increasing velocities in the reaction zone are a result of density changes resulting from heat release, so the general behavior of the changes in velocity should follow the temperature trend. This velocity difference will be referred to as the dilatation velocity. Figure 4-7 shows the phase difference between the air velocity and the dilatation velocity as a function of frequency and initial steady strain rate. The magnitude of the phase difference was found to increase with increasing forcing frequency, which suggests there is a systematic increase in the phase difference between the velocity and the temperature. The time associated with the increasing phase difference is likely related to a diffusion time. As the forcing frequency is increased, the time rate of change of reactants delivered to the edge of the convective-diffusive zone increases; however, a finite amount of time is still necessary for the reactants to diffuse to the flame front. As the forcing frequency increases, this diffusion time

becomes larger relative to the cycle time of the oscillation, which in turn shows up as an increasing phase difference. This "diffusion limited" response has been observed in previous numerical studies [3,4].

Conclusions

The response of a propane-air counterflow diffusion flame subjected to an unsteady flow-field was investigated to increase fundamental understanding of turbulent flame behavior and to help qualify the quasi-steady assumption used in flamelet theory. The conclusions drawn from this investigation are as follows:

1) The width of the OH field appears to be responding quasi-steadily to the instantaneous strain rate for forcing frequencies of 30·Hz and 50·Hz; the calculated phase difference between the strain rate and width of the OH field are 183° and 185° respectively. However, at forcing frequencies of 100·Hz and 200·Hz, the phase lag of the OH field thickness grew to 210° and 241°, respectively.
2) For the weakly forced flames presented in this report, the sinusoidal response of the velocity, strain rate, and width of the OH field correlated well with the speaker oscillations at the given frequency.
3) A phase difference was present between the velocity and the strain rate, which was found to decrease with increasing forcing frequency. This apparently results from the distortions imposed on the velocity field due to a phase shifted thermal expansion.
4) The dilatation velocity was used as an indicator of flame temperature. The phase difference between the velocity and the dilatation velocity was found to increase with

increasing forcing frequency. This increasing phase difference suggests the transport of reactants through the reactive-diffusive zone of the flame is the limiting step in the response of the flame sheet.

Acknowledgements:

This work was supported by the Army Research Office, ARO Grant Number DAAH04-95-10230, under the technical monitoring of Dr. David Mann

References

1. Peters, N., Prog. Energy Comb. Sci., 10:319-339 (1984).
2. Bray, K.N.C., Peters, N., Turbulent Reacting Flows, Academic Press Ltd, (1994), p. 63.
3. Im, H.G., Law, C.K., Kim, J.S., Williams, F.A., Combust. Flame, 100:21-30 (1995).
4. Egolfopoulos, F.N., Campbell, C.S., J. Fluid Mech., 318:1-29 (1996).
5. Darabiha, N., Combust. Sci. and Tech., v86, pp. 163-181 (1992).
6. Brown, T.M., Pitz, R.W., Sung, C.J., Proc. Combust. Inst. 27: 703-710 (1998)
7. Puri, I.K., Seshadri, K., Combust. Flame, 65, 137-150 (1986).
8. DeCroix, M.E., Roberts, W.L., Comb. Sci. Tech v146, pp.57-84, (1999).
9. Sung, C.J., Kistler, M., Nishioka, M., Law, C.K., Combust. Flame, 105:189-201 (1996).
10. Sung, C.J., Liu, J.B., Law, C.K., Combust. Flame 102:481-492 (1995).
11. Pellett, G.L., Isaac, K.M., Humphreys, JR., W.M., Gartrell, L.R., Roberts, W.L., Dancey, C.L., Northam, G.B., Combust. Flame 112:575-592 (1998).

12. Kistler, J.S., Sung, C.J., Dreutz, T.G., Law, C.K., Nishioka, M., Proc. Combust. Inst. 26: 113-120 (1996)

13. Kim, J.S., Libby, P.A., Williams, F.A., Combust. Sci. and Tech., v87, pp. 1-25 (1992).

14. Zhoa, J., Isaac, K.M, Pellett, G.L., Journal of Propulsion and Power, Vol. 12, No. 3 (1996).

Table 4-1 Voltage amplitude relative to flow reversal and extinction amplitude

Forcing Amplitude						
	SSR 23 s^{-1}		SSR 44 s^{-1}		SSR 74 s^{-1}	
Freq	V	V	V	V	V	V
(Hz)	Vrev	Vext	Vrev	Vext	Vrev	Vext
30	1	0.25	0.5	0.13	0.5	0.17
50	1	0.15	0.5	0.08	0.5	0.17
100	1	0.05	0.5	0.05	0.5	0.14
200	1	0.05	0.5	0.05	0.5	0.1

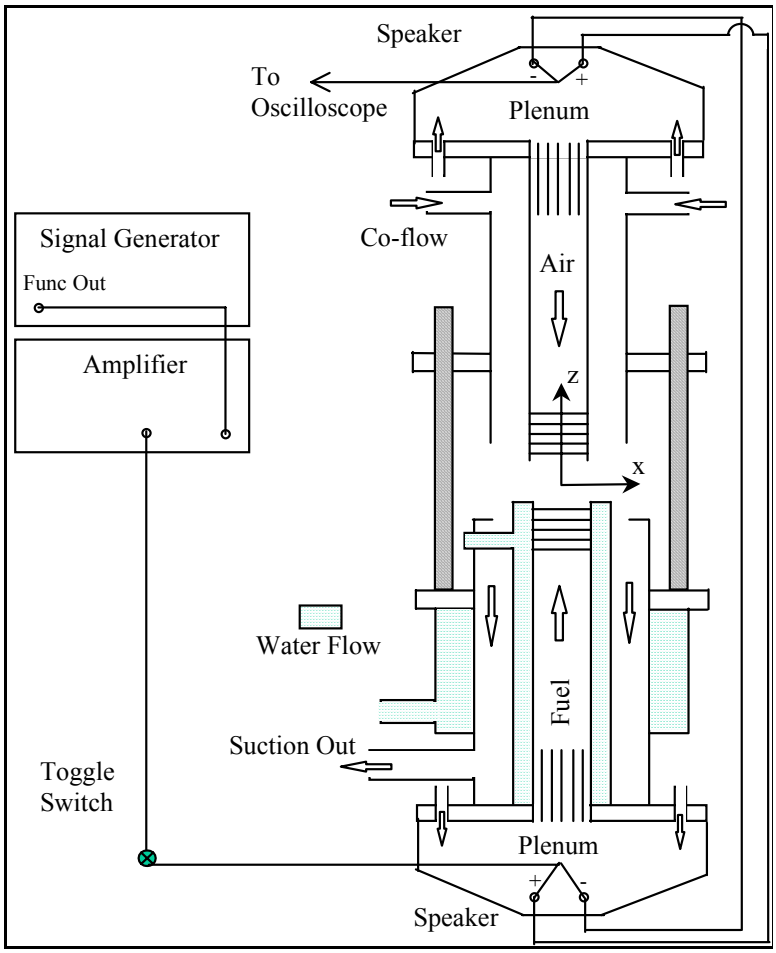

Figure 4-1 Schematic of counterflow diffusion flame burner

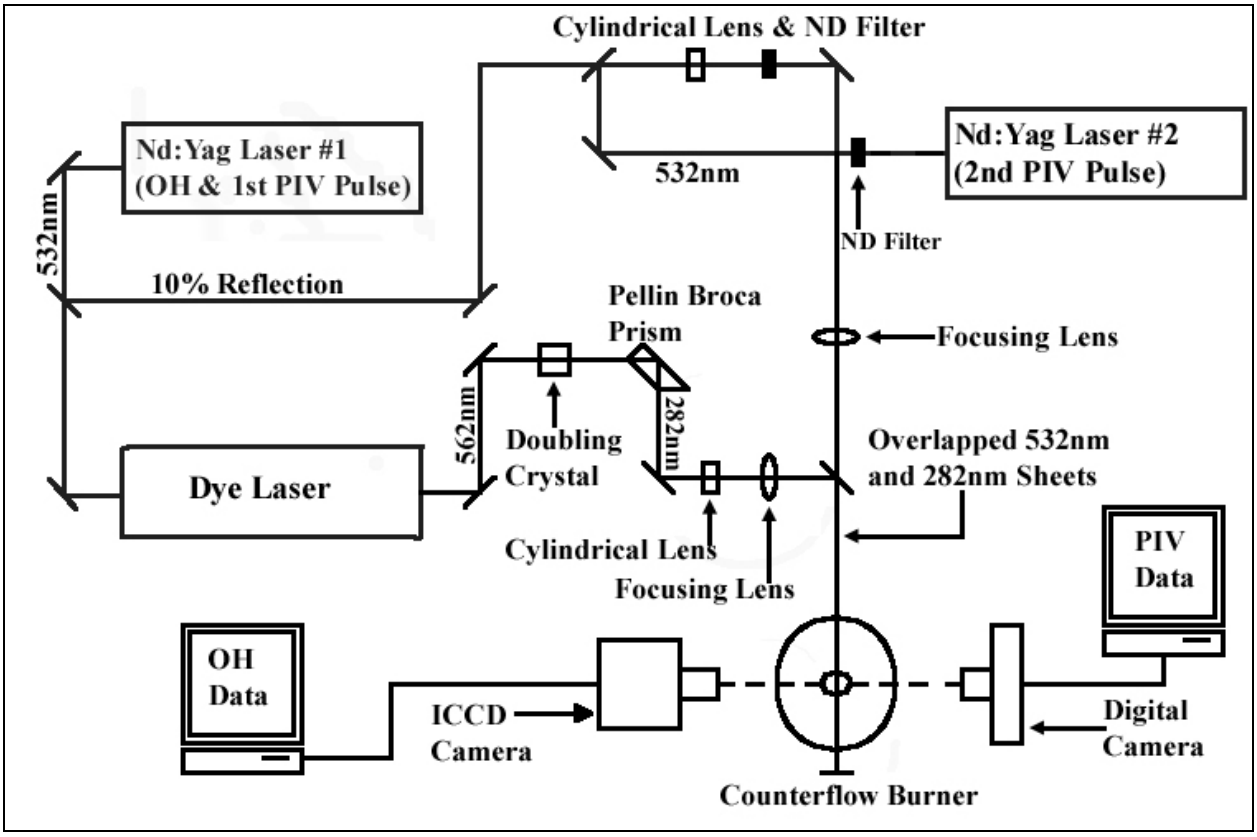

Figure 4-2 Optical Layout for PIV and OH-PLIF measurements

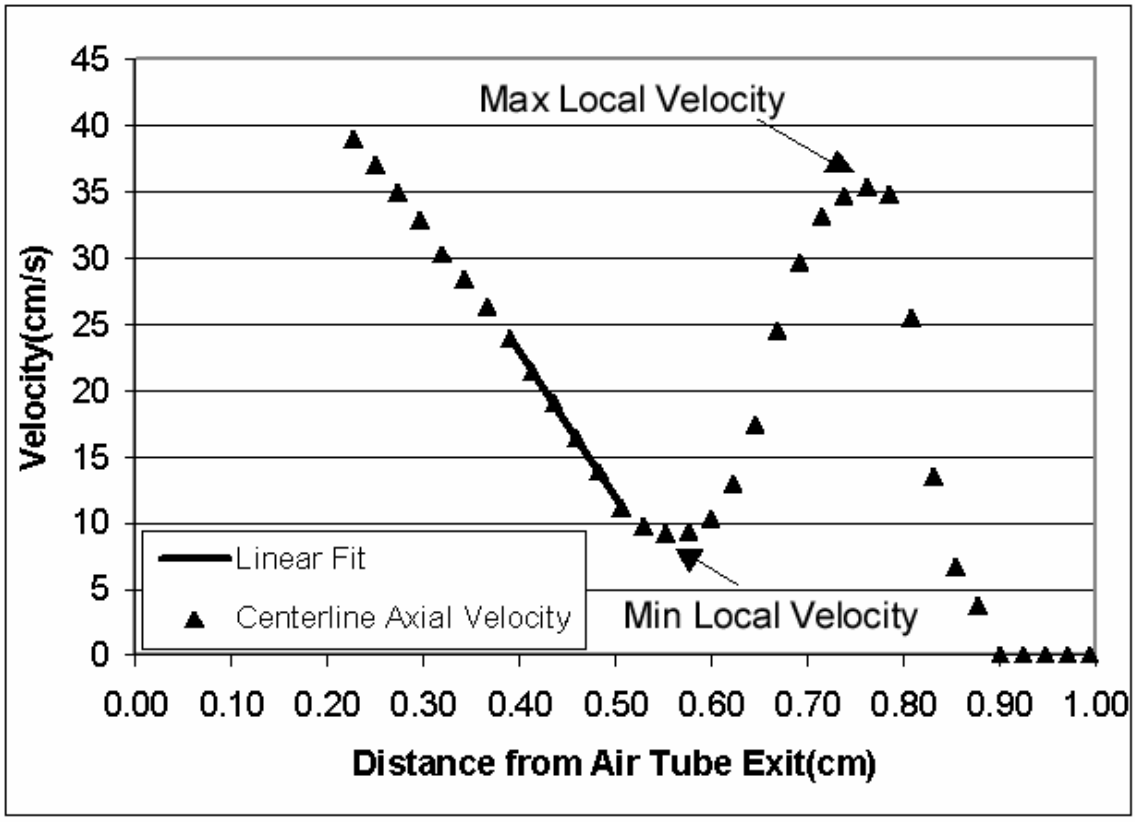

Figure 4-3 Velocity field data showing the linear fitted line for strain rate calculations. Also shown are the velocities used to determine the dilatation velocity

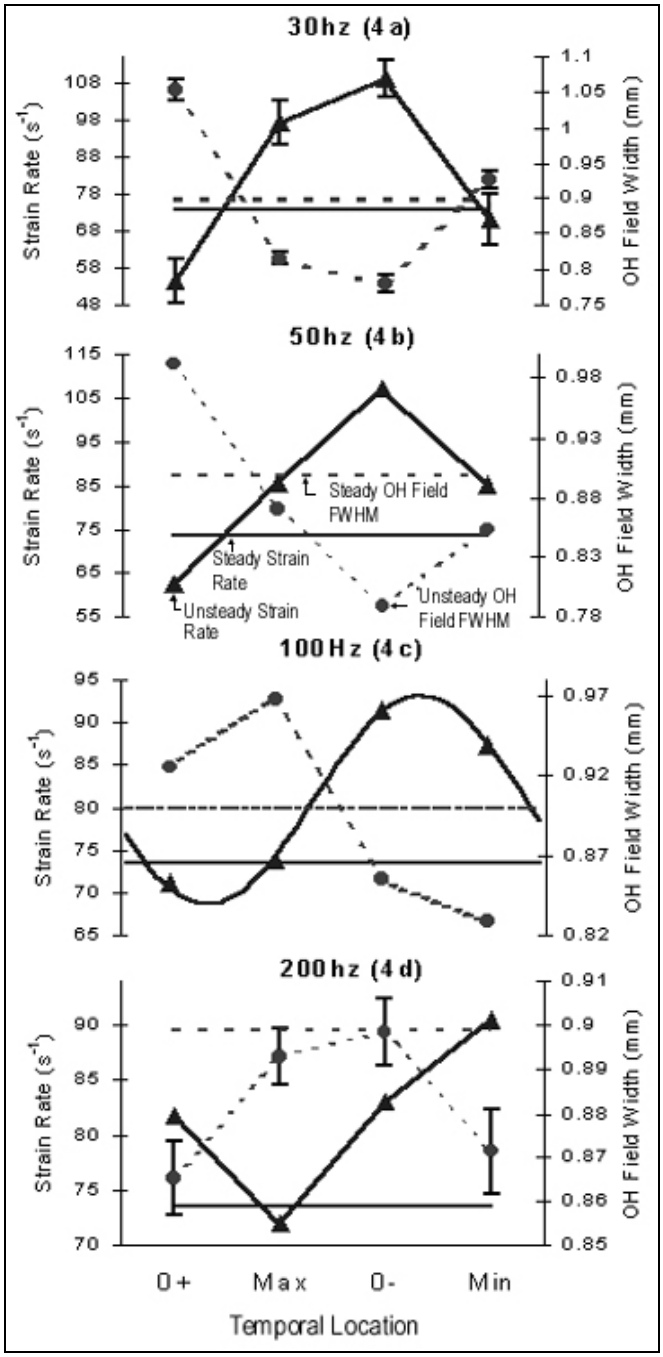

Figure 4-4 Strain rate and FWHM of the OH field results for SSR 74·s^{-1} and all forcing frequencies. Error bars of one standard deviation have been included for the OH fields FWHM on the 30 Hz and 200 Hz forcing frequencies as well as for the strain rate at 30 Hz. Error bars for the strain rate were excluded on the 200 Hz forcing frequency plot for clarity. The fitted strain rate sine wave curve is also included on the 100 Hz forcing frequency plot

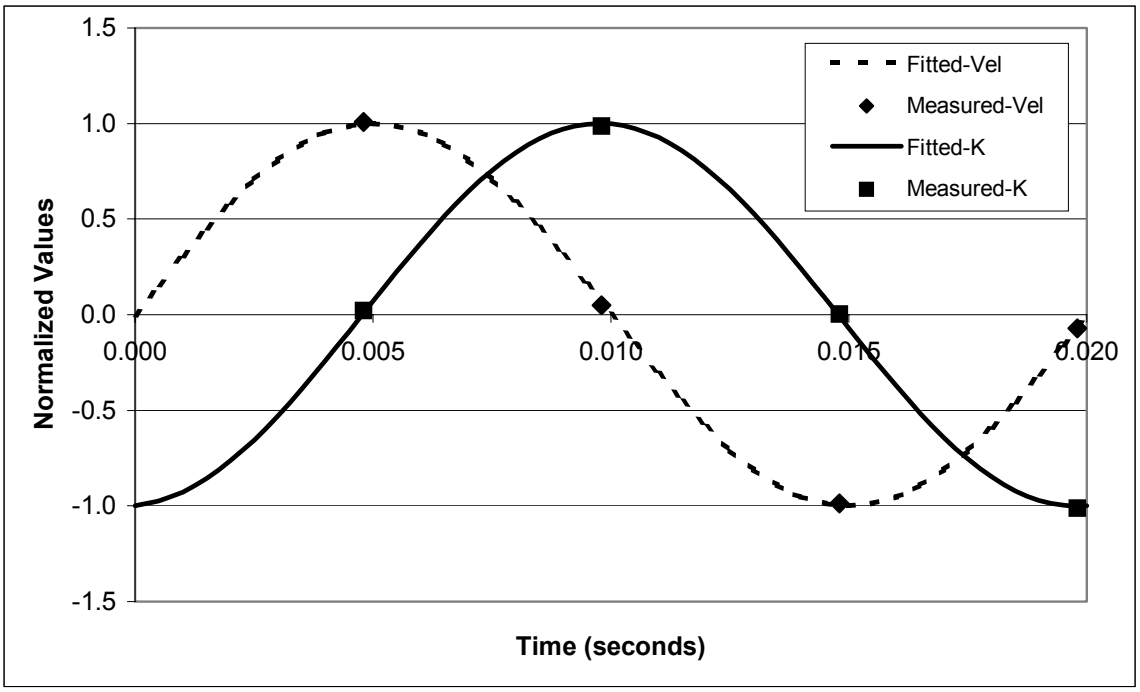

Figure 4-5 Normalized velocity and strain rate data with their fitted curves for SSR 74·s^{-1} and 50·Hz. The solid circles are the measured velocities and the dashed line is the fitted sine function to the velocity data. The filled squares are the measured strain rates and the solid line is the fitted sine function for the strain rate data

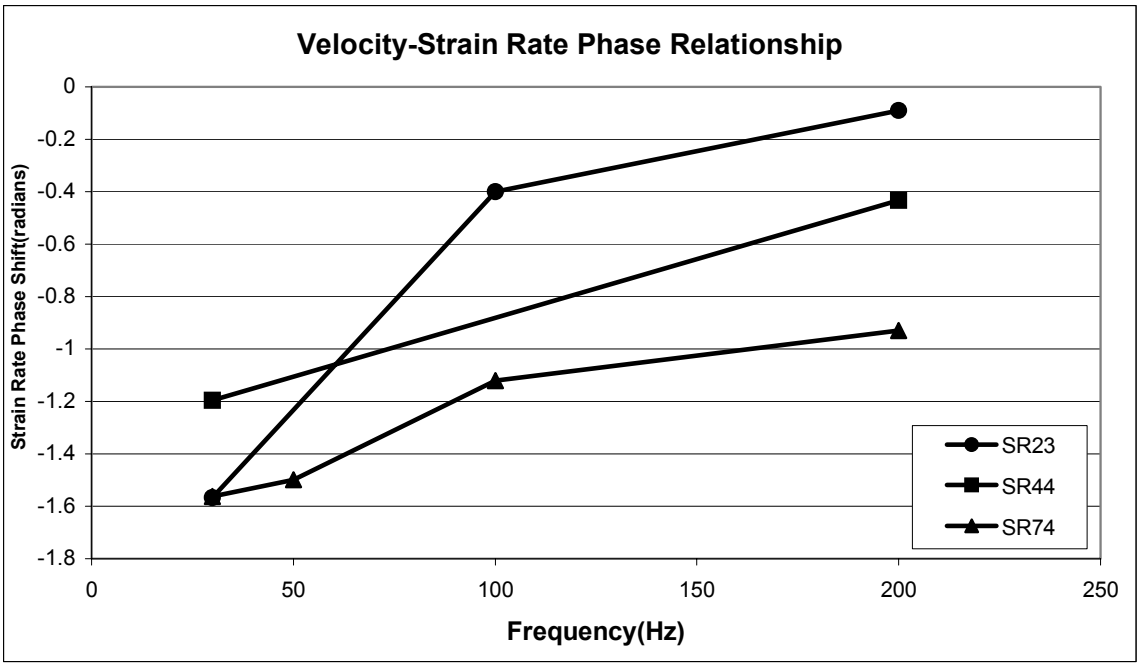

Figure 4-6 Phase difference relationships between the air velocity and the strain rate as a function of frequency for initial steady strain rates of $23 \cdot s^{-1}$, $44 \cdot s^{-1}$, and $74 \cdot s^{-1}$. The circles connected by solid lines represent the $23 \cdot s^{-1}$ data, the squares represent the $44 \cdot s^{-1}$ data, and the triangles represent the $74 \cdot s^{-1}$ data

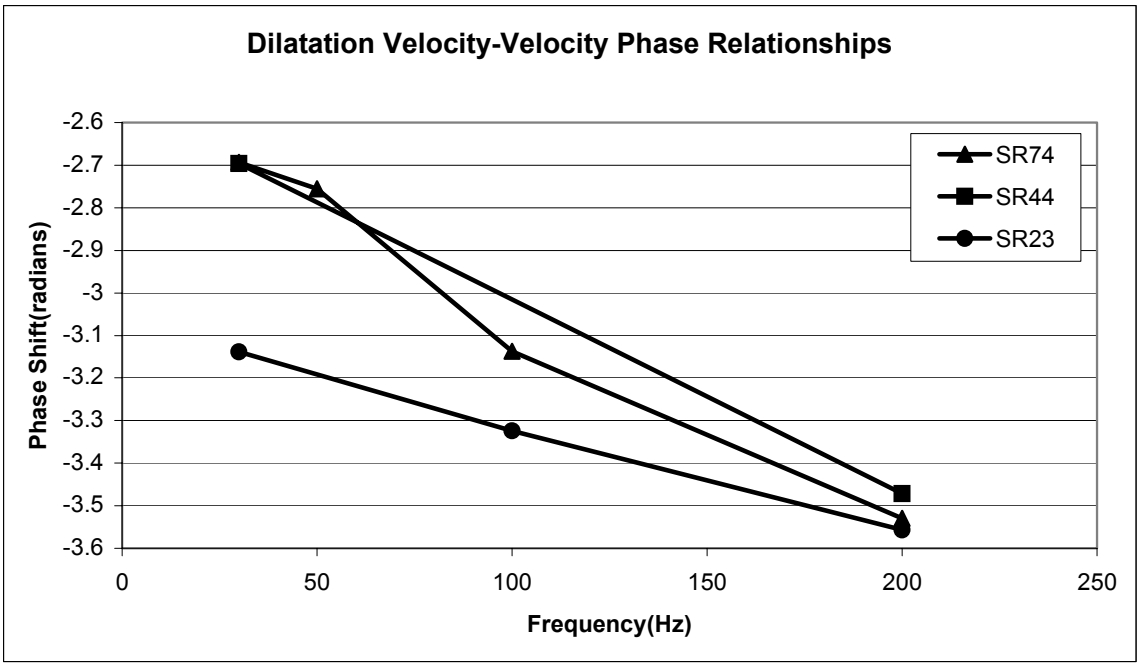

Figure 4-7 Phase difference relationships between the dilatation velocity and the air velocity. The circles connected by solid lines represent the $23 \cdot s^{-1}$ data, the squares represent the $44 \cdot s^{-1}$ data, and the triangles represent the $74 \cdot s^{-1}$ data. The change in velocity was determined by the difference between the maximum velocity in the reaction zone and the minimum velocity in the preheat zone

Response to written questions

Q1 from Sebastien Candel, Ecole Centrale Paris

Question: One characteristic time of a strained diffusion flame is just the inverse of the strain rate. This could be used to define a dimensionless frequency and this might allow you to collapse the data gathered in these experiments.

Answer: Following the work of Egolfopoulos and Campbell [ref 4], a dimensionless Stokes parameter may be defined as $(\pi f/k)^{1/2}$, where f is the forcing frequency and k is the steady strain rate. If the change in thickness of the OH zone through the oscillation, normalized by the steady thickness, is plotted against the log of this Stokes' parameter, all the data from the four forcing frequencies (30, 50, 100 and 200 Hz) and three different initial strain rates (23, 44, and 74 s^{-1}) collapse very well onto a single line with a fairly steep negative slope. The Stokes' parameter ranges from 1 to 6 in these experiments; Ref 4 shows a negative slope when the normalized maximum temperature is plotted over this range as well.

Q2 from Jay Jeffries, Stanford University

Question: Could you qualify the uncertainty on temperature and spatial resolution? It appears you have drawn conclusions from temperature variations of 15 K and spatial (OH FWHM) variations of 10's of μm.

Answer: First, allow us to make a correction to Fig. 4 of the paper; the OH Field Widths, shown as the y-axis, should be scaled up by a factor of 3.5. With this correction, the maximum delta in OH field width throughout the oscillations range from 280 □m at 30 Hz to 31 □m at 200 Hz. While these differences are small, from 3 to 30% of the steady width (880 □m), they are real and very repeatable. The axial OH profile was averaged about the centerline in the radial direction over 3 mm (60 pixels), and 20 OH PLIF images were averaged to get the final OH field width. The standard deviation among these 20 images at each location within the oscillation was typically less than 1% and always less then 2%. Thus, while our smallest delta in field width is 0.7 pixels wide, due to the radial averaging, we believe this is a real result. The standard deviation in temperature is very similar. So, while the absolute temperatures are no better than to within 50 K, the relative temperatures throughout the oscillation are much better. Further details regarding the thermometry are forthcoming.

5 The Response of a Propane-Air Counter-Flow Diffusion Flame Subjected to a Transient Flow Field

Abstract

OH planar laser-induced fluorescence (PLIF) and particle image velocimetry (PIV) have been used to study the frequency response of laminar C_3H_8-air counterflow diffusion flames, and thereby the adequacy of the steady-flamelet model for turbulence. PIV was used to determine the flame strain rate, while OH PLIF was used both to measure temperature at the flame front, using the two-line PLIF technique, and the reaction-zone width. Both measurements demonstrate the existence of a diffusion-limited frequency response of flames subjected to a time-varying flow field. At the 30-Hz and 50-Hz forcing frequencies, the maximum reaction-zone temperature and width were found to respond quasi-steadily. However, at higher forcing frequencies—that is, 100 and 200 Hz—transient behavior is evident from the phase relationship between the imposed sinusoidal strain rate and the resulting peak temperature and reaction-zone width. The measured values of the OH-field widths (FWHM) were fit well by an offset sine function. In all cases when the oscillation amplitude (from the sine-curve fit) is normalized by the cycle mean strain rate and plotted against the non-dimensional flow field frequency, it collapses onto a single line with a steep negative slope.

Introduction

Many practical combustion devices rely on turbulent diffusion flames due to their higher heat release rates. For this reason, great efforts have been expended to further the fundamental understanding of these types of flames. Flamelet theory is a method that characterizes turbulent diffusion flames as a collection of strained, laminar, one-dimensional flamelets [1,2], which can be fully characterized by the mixture fraction and instantaneous scalar dissipation rate. These flamelets are assumed to respond quasi-steadily to the unsteady strain rates of the turbulent flow field. Recent computational and experimental studies, however, have shown that conditions exist where this assumption is invalid [3-6]. If the turbulent Reynolds number is sufficiently large, there exists a range of eddy sizes where the characteristic turnover times of the smallest eddies are comparable to the diffusion times of the laminar flamelets [3]. This also leads to a wide range of characteristic frequencies [4]. Therefore, it is necessary to investigate the frequency response of flamelets to extend the applicability of the flamelet model.

The purpose of this investigation was to quantify the response of the reaction-zone temperature and thickness and the local strain rate to a time-varying flow field. A counterflow diffusion burner was used because the associated flame has the same scalar structure as a flamelet in the mixing zone of a turbulent reacting flow field [1]. The temperature field in the reaction zone was experimentally determined using two-line OH planar laser-induced fluorescence (PLIF) thermometry. Particle image velocimetry (PIV) was used to quantify the velocity and strain rate relationships between measured parameters as a function of flow rate oscillation frequency. Simultaneous with velocity, the OH-field width was measured using

PLIF. Reaction-zone thickness was characterized by the full width at half maximum (FWHM) of the OH field.

Experimental Apparatus and Procedure

A schematic of the counterflow diffusion flame burner used in this study is shown in Figure 5-1. The burner is a modification of the design described by Puri and Seshadri [7] and is described in detail in ref. [8]. The oxidizer and fuel tubes are 25.4 mm in diameter. A 12.7-mm separation distance between the reactant delivery tubes was used in this study. Plenums located on the fuel and oxidizer sides are capped with 20-cm loudspeakers, which impose the velocity fluctuations and are driven by an amplified signal generator.

An unsteady flow field was imposed on the counterflow diffusion flame by providing a sinusoidal voltage to the speakers. Velocity and relative [OH] measurements were made as a function of initial steady strain rate (SSR) and forcing frequency [9]. These measurements were made at four temporal locations within the sinusoidal voltage oscillation applied to the speakers: 1) zero amplitude with positive slope, designated *0+*; 2) maximum amplitude, designated *Max*; 3) zero amplitude with negative slope, designated *0–*; and 4) minimum amplitude, designated *Min*. The forcing frequencies considered in this study were 30, 50, 100, 200 and 500 Hz. Results for three flow conditions are reported in this study and are given in Table 5-1 below in standard liters/min, slpm (where "standard" refers to STP conditions). These flow rates determine the steady strain rate (SSR), which is defined here as the gradient of the airside axial velocity just prior to the heat release zone.

When possible, non-intrusive techniques are preferred over physical probes when performing combustion measurements. In this study, two-line OH-PLIF thermometry was chosen because it is non-intrusive and has been shown to be a successful method for measuring flame temperature [10-12]. However, this technique is not without its drawbacks, including bias associated with absorption and radiation trapping, electronic quenching, and dye laser wavelength drift. Figure 5-2 is a schematic of the two-line OH PLIF measurement system used in this study. The OH measurements, which were used to characterize the response of the temperature field of the reaction zone, were made using two Nd:YAG-pumped dye lasers. The output of each dye laser was frequency doubled (to ~282 nm and ~286 nm), yielding a 10-mJ, 10-ns pulse. Each beam was formed into a sheet using a negative cylindrical lens and a positive (1 m focal length) spherical lens. The two beams were then overlapped using a polarization-based beam combiner. At the probe region, the resulting sheet dimensions were measured to be approximately 300 μm (width) by 10 mm (height). Note that the variation in the thickness across the probe region was small due to the long focal length of the focusing lens.

The $Q_1(5)$ and $Q_1(14)$ transitions of the $A^2\Sigma^+ \leftarrow X^2\Pi$ (1,0) band were excited and the fluorescence detected using intensified charge-coupled device (ICCD) cameras. UV 105-mm, f/4.5 lenses, fitted with UG-11 and WG-295 Schott glass filters were used to collect the OH fluorescence and block laser scattering. Here, the field of view of each ICCD camera was 14 mm × 9.5 mm, and the 576 × 384 pixel array was binned 2 × 2, resulting in a scaling factor of 20.3 pixels/mm. The fields of view of the two cameras were overlapped using a transparent target—one employing both a course grid, with 2.5-mm line spacing, and a fine grid, with 0.5-

mm line spacing—which was placed in the probe region during alignment. A delay generator controlled timing and triggering for the lasers and digital cameras. An oscilloscope was used to display the speaker oscillation relative to a photodiode signal, which was collected from a laser-beam reflection just prior to the counterflow burner. Using these two signals, it was possible to phase lock the timing of the laser pulses with a chosen temporal location in the speaker oscillation by simply delaying the initial trigger in the delay generator.

Prior to entering the interrogation region of the flame, portions of the two UV pulses were redirected across a porous plug burner, and the resulting fluorescence was detected using two photomultiplier tubes (PMTs), one for each pumped transition, located on either side of the flame. The output of each PMT was then integrated using a gated integrator/boxcar averager. In this way, LIF signals from each laser were monitored to mitigate dye laser wavelength drift and energy fluctuations.

To derive temperatures from the two OH PLIF measurements, it was necessary to first calibrate the two OH PLIF systems using a known temperature. A 25-mm-square Hencken burner employing CH_4 and air was used for this purpose [13]. Though this burner is normally used in a non-premixed mode with H_2 and air, here the CH_4 and air were premixed at the air-side port. Table 5-2 shows the equivalence ratios used in the CH_4-air Hencken flame, the resulting measured image intensity ratios, and the calculated adiabatic equilibrium flame temperatures. Over this range of conditions, this flame has also been studied with the Rayleigh/Raman scattering technique, and the derived temperatures are within 50 K of the adiabatic equilibrium result [14].

As expected, the ratio $I_{Q1(5)}/I_{Q1(14)}$ will vary significantly with temperature, and is shown in Figure 5-3 by a calculation of the relative Boltzmann fractions for the two states. A second-degree polynomial was used to fit a calibration curve to the Hencken burner temperatures. All maximum reaction-zone temperatures reported in this paper are within the bounds of the Hencken burner's calibration temperatures.

Mass flow controllers were used to meter the flows of both the C_3H_8-air counterflow diffusion flame and the CH_4-air Hencken calibration flame and the meters were calibrated using a DryCal DC-2M positive-displacement volumetric flow meter.

As noted above, accuracy of two-line OH LIF thermometry is affected by absorption and electronic quenching, the latter due to the variation in the electronic quenching rate between the $N' = 5$ and 14 states. To help mitigate these sources of bias, fluorescence measurements of both the $Q_1(5)$ and $Q_1(14)$ transition were performed in the saturation regime. The correction procedure for the raw $Q_1(5)$ images only included the subtraction of a background image since the transition was well saturated. For the $Q_1(14)$ images, the correction procedure also included correcting for flat field effects of the ICCD because large variations in gain were noted over the intensifier array. Once these corrections were performed, the ratio of the $Q_1(5)$ and $Q_1(14)$ images were related to temperature using the Hencken burner calibration.

Subsequently, the maximum centerline temperature, T_{max}, was determined at each temporal location. This was done by row averaging a region that was 40 super-pixels (binned 2 × 2) wide (20 on either side of the centerline of the reactant tubes); this corresponds to a region ~ 2 mm wide. Figure 5-4 shows the centerline temperature for the unforced (steady) case with a

SSR of 44 s^{-1}; here T_{max} was found to be 2113 K with this procedure. The adiabatic equilibrium temperature for a stoichiometric C_3H_8-air mixture is about 100 K higher than this value. Presumably, this difference of ~100 K represents the bias error in the temperature measurements resulting from uncertainty in the true calibration flame temperature [17], from the correction procedure, the temperature dependence on strain rate, and radiation. Nonetheless, this accuracy was sufficient to accomplish the primary goal, namely the observation of temperature variations with strain rate and forcing frequency.

Figure 5-5 is a schematic of the OH-PLIF/PIV system. This setup is identical to a previously used configuration, which was reported and can be reviewed in [9]. Briefly, the PIV measurements were made using two frequency-doubled Nd:YAG lasers (λ = 532 nm), one of which was also employed to pump a dye laser. The images were collected using a Kodak ES1.0 interline-transfer CCD camera. As can be seen from Figure 5-5, the OH PLIF measurement was temporally coincident with the first PIV frame; timing for the second PIV frame was selected to achieve reasonable particle displacements, typically 10 to 20 pixels on the CCD array. Custom software using a cross correlation algorithm was then used to derive velocity from the scattering images.

Clearly, one difficulty of employing particle-based techniques such as PIV (or laser Doppler velocimetry, LDV) in a counterflow burner arises from the phenomenon of thermophoresis. Thermophoresis—which has been studied in detail by Sung et al. [15] in the context of flame velocity measurements—is the tendency for the particle to drift *down* the temperature gradient; Sung and coworkers showed that near the region of the maximum temperature gradient, velocity

measurement error can be as large as 10 to 15 cm/s. Here, however, velocity measurements were made only in the preheat zone where the temperature gradients will be small. Thus, error in the PIV velocity measurement will also be small.

The OH-field width measurements, which were used to characterize the reaction zone's response, were made in the same fashion as the two-line measurements. The $R_1(8)$ transition of the $A^2\Sigma+ \leftarrow X^2\Pi$ (1,0) band was excited, partially saturating the transition, and the fluorescence was detected using an ICCD camera. The $R_1(8)$ transition was chosen because of its ground state population's low sensitivity to the temperature changes considered in this study. Twenty OH and PIV images were taken and averaged at each of the four temporal locations within the speaker oscillation. The response of the reaction zone to velocity oscillations was characterized by measuring the full width at half maximum (FWHM) of the OH field. The strain rate was determined by evaluating the gradient of the measured axial velocity profile at the centerline of the burner on the oxidizer side of the stagnation plane prior to the heat-release zone, as illustrated in Figure 5-6. Here, the heat-release zone is clearly evident from the increase in the velocity in the region between 0.6 and 0.75 cm from the air-tube exit. As noted above, the location of the strain rate measurement is not coincident with the region of large heat release, and therefore is minimally affected by thermophoretic velocity bias.

Results and Discussion

As previously stated, a fundamental assumption of the flamelet model is that the flamelet responds quasi-steadily to the flow field. If this condition holds true, the flamelet can be fully characterized by the mixture fraction and the instantaneous scalar dissipation rate. However, if

the flamelet is subjected to rapid changes in strain rate, a more detailed description of the system is required [2,4,9].

The measured strain rates and the maximum reaction zone temperatures, T_{max}, are plotted in Figure 5-7 for a SSR of 44 s^{-1} (unforced flow conditions) at various forcing frequencies. The precision of the mean measurements is given by the standard deviation of the mean, defined in the conventional sense as the standard deviation of parameter x, σ_x, divided by the square root of the number of samples, $\sigma_{\bar{x}} \equiv \sigma_x / \sqrt{N}$. For the temperature, $\sigma_{\bar{T}}$ varied between 5 and 29 K, whereas for the strain rate measurements, $\sigma_{\bar{K}}$ varied between 0.4 s^{-1} and 1.3 s^{-1}. The full error bar length represents twice σ_x.

At a forcing frequency of 30 Hz (Figure 5-7 A), the measured strain rate increases between the temporal locations of *0+* and *0–* from 30 s^{-1} to 73 s^{-1}. During this period T_{max} decreases from 2153 K to 2055 K. Then, between locations *0–* and *Min*, the strain rate decreases to 41 s^{-1} and T_{max} increases to 2129 K. At this forcing frequency, the flame appears to be responding in a quasi-steady manner, i.e., with increasing strain rate, T_{max} decreases, and when the strain rate decreases, the T_{max} increases. However, for steady strain rate, the T_{max} continuously decreases with increasing strain rate (decreasing Damkohler number) due to increasing thermal and species concentration gradients, which can eventually lead to extinction of the flame.

As the forcing frequency increased to 50 Hz (Figure 5-7 B), the measured strain rate is found to increase from 38 s^{-1} to 64 s^{-1} between the *0+* and *0–* locations, while T_{max} decreases from 2116 K to 1942 K. Between the *0–* and *Min* phases, the strain rate decreases to 41 s^{-1} and T_{max}

increases to 2091 K. Thus, as evidenced by this phase relation between imposed strain and T_{max} (i.e., ~180° out of phase), the flame is responding in a quasi-steady manner at both 30 and 50 Hz.

The flame behavior shows unsteadiness when the forcing frequency is increased to 200 Hz. Between the locations of *0+* and *Max*, the strain rate decreases from 58 s^{-1} to 41 s^{-1} while T_{max} decreases from 2105 K to 2071 K. T_{max} then shows a small decrease to 2064 K at *0–* and finally drops to 2037 K at the *Min* location. The strain rate shows a reasonable increase between *Max* and *0–* to 54 s^{-1} and continues to increase to 60 s^{-1} at the *Min* location in the speaker oscillation. Based upon the reaction-zone temperatures at the 200 Hz forcing frequency, there appears to be a phase shift between the imposed strain rate and the maximum temperature in the reaction zone.

A reasonable sinusoidal fit with the measured strain rate and maximum reaction zone temperature can be made at forcing frequencies of 30 and 50 Hz, but is unsatisfactory at 200 Hz where the uncertainty in the measurements is also largest (and the fluctuation in temperature is relatively small). Other than inherent experimental uncertainty, the agreement between the fitted curves and the measured data is affected by non-sinusoidal flame response, which has been attributed to leakage of reactants through the reaction zone [4], as well as the complex coupling of temperature and flow-field conditions which lead to soot formation.

Figure 5-8 illustrates the response of T_{max} and the strain rate for the same unforced flow conditions (SSR = 44 s^{-1}), but with smaller oscillation amplitudes at 30 and 200 Hz. Smaller fluctuation amplitudes were also investigated to test conditions that were far from extinction and would experience minimal reactant leakage. For the flows shown in Figure 5-8, the amplitude oscillations were 13 and 5 % of the extinction amplitude for 25 Hz and 200 Hz forcing

frequencies [8]. A good sinusoidal fit can be made here (in contrast to the case illustrated in Figure 5-7(C)). Particularly interesting is the result shown in Figure 5-8 (B), where the strain rate and the maximum reaction zone temperature are approximately in phase at the 200 Hz oscillation frequency, which is a significant departure from quasi-steady behavior. This result further illustrates the diffusion limited frequency response of the reaction zone as previously illustrated [4,9,18].

The amplitude of oscillation is the same for both conditions shown in Figure 8, but the peak-to-peak amplitude of T_{max} is 49 K for the 30 Hz case and 90 K for the 200 Hz case where the mean fitted temperature for the two cases only varies by 5 K. Based upon previous results, we may expect the amplitude to decrease with increasing forcing frequencies. Soot production, however, could be a significant factor; indeed, earlier measurements found peak soot volume fraction measured at a 25 Hz oscillation were greater and had a 40% difference compared to the 200 Hz oscillation case [8]. Also, the soot volume fraction fluctuations for the initial flow conditions shown in Figure 5-8 become insensitive above 100 Hz [8].

Previously, the "dilatation velocity" was used as a qualitative flame-temperature marker [9]. The dilatation velocity was defined as the difference between the minimum velocity just prior to the heat-release zone and the maximum velocity in the heat-release zone; or about 26 cm/s based on the velocities shown in Figure 5-6. An increasing phase angle was found between the strain rate oscillations and the dilatation velocity with increasing forcing frequency. Due to the precision of the measurements, sampling of four temporal locations is not sufficient to properly resolve the frequency response of T_{max} accurately enough to determine phase-angle relationships.

Therefore, only qualitative comparisons can be made between the maximum temperature in the reaction zone and the instantaneous strain rate.

In Figure 5-9 the relationship between the strain rate and the width (FWHM) of the OH field is shown for three forcing frequencies for the SSR of 44 s^{-1} with the same flow and oscillation amplitude conditions illustrated in Figure 5-7. As seen in the relationship between imposed strain rate and the maximum reaction zone temperature, with forcing frequencies of 30 Hz and 50 Hz, the OH field appears to be responding quasi-steadily to the instantaneous strain rate: as strain rate increases, the reaction zone width, indicated with the OH–field width, decreases and vice versa. Between the temporal locations *0+* and *0–*, the strain rate increases continuously, while the FWHM of the OH field continuously decreases. Between the *0–* and *Min* locations, the converse is seen at 30 Hz and 50 Hz forcing frequencies.

As with the temperature measurements, unsteady behavior is found for the OH-field width at a forcing frequency of 200 Hz when considering the four measured points in the oscillation. Between the *Max* and *0-* locations, the strain rate and the OH-field width are both increasing. From the results shown in Figure 5-7 and Figure 5-9, higher temporal sampling is necessary to properly describe the behavior at a forcing frequency of 200 Hz.

Now, consider OH-field FWHM measurements in Figure 5-10, which correspond to the same conditions illustrated in Figure 5-8. At the lower amplitude and 30 Hz forcing frequency, the OH field and strain rate are almost 180° out of phase as expected in a quasi-steady flame. As with the maximum reaction zone temperature measurements at 200 Hz, a considerable departure from quasi-steady behavior is found: the strain rate and the OH-field thickness are approximately

in phase, showing the presence of a diffusion limited frequency response of the flame. Essentially, the flame will respond to the reactants delivered to the flame front, but as the time rate of change of reactants delivered to the edge of the convective diffusive zone increases and approaches a characteristic diffusion time, a phase-shifted response of the flame will occur.

In a numerical study of an opposed-flow CH_4-air flame, Im, et al., [16] showed that stoichiometric scalar dissipation rate χ_{st} is more closely correlated than the air-side strain rate (as defined in Figure 5-6) with the unsteady flowfield [16]. More specifically, Im, et al., found the following: 1) at low flow-field oscillation frequency, the resulting χ_{st} follows more closely steady-flame response (than does K_{air}); and 2) the phase variation of χ_{st} is monotonically increasing with increasing flow-field oscillation frequency, whereas with K_{air} the phase variation increases initially and then decreases beyond 200 Hz. Of course, K_{air} is much easier to measure, and so in spite of its deficiencies, it has been used in the present study. As previously suggested, when the flame is responding steadily, the scalar dissipation rate scales directly with strain rate [19].

Figure 5-11 (C) shows the results of a SSR 84 s^{-1} case with a 500 Hz oscillation. The measured strain rate response is reasonably sinusoidal, but no discernable trends are seen in the OH-field response. This would suggest that at this oscillation amplitude and frequency, the changes are undetectable with the resolution used for these measurements. In general, the OH-field response fits a sinusoid very accurately, especially for the higher steady strain rate conditions.

In a numerical investigation, Egolfopoulos and Campbell [4] were able to correlate the variation in maximum flame temperature with a dimensionless frequency, a so-called Stokes parameter η_K, defined as,

$$\eta_K = \left(\frac{\pi \cdot f}{K} \right)^{\frac{1}{2}} \qquad (1)$$

Where, f is the forcing frequency and K is the cycle mean strain rate. This comparison can also be made with the variation in reaction-zone width. Here, the measured OH-field widths were fit to an offset sine function,

$$FWHM_{OH} = u_0 + u_1 \cdot \sin\left(2 \cdot \pi \cdot f \cdot t + u_2\right) \qquad (2)$$

where u_0 is the mean value, u_1 is the amplitude of the oscillation of the OH-field width, f is the forcing frequency, t is time within the oscillation, and u_2 is a phase angle. In Figure 5-12, the variation in thickness of the OH zone through the oscillation (amplitude of the oscillation) normalized by the mean value is plotted against the logarithm of this Stokes parameter. All the data from the four forcing frequencies (30, 50, 100 and 200 Hz) and three different initial strain rates (23, 44, and 74 s^{-1}) collapse onto a single line with a fairly steep negative slope. At the largest η_K, however, the slope magnitude appears to decrease, perhaps due to the limited spatial resolution of the OH PLIF system (and a concomitant limited ability to resolve small changes in thickness). The Stokes parameter ranges from about 1 to 6 in these experiments, which is similar to the results reported by Egolfopoulos and Campbell [4]. Fundamentally, this plot illustrates

that the OH-field width oscillations are attenuated in a predictable fashion with increasing frequency for the conditions illustrated. For the condition shown in Figure 5-11 (C), the Stokes parameter is ~4.4 and based on the Stokes plot, the normalized OH FWHM variation would be ~.018.

Conclusions

OH planar laser-induced fluorescence (PLIF) and particle image velocimetry (PIV) have been used to study the frequency response of laminar C_3H_8-air counterflow diffusion flames. PIV was used to determine the flame strain rate, while OH PLIF was used both to measure temperature at the flame front, using the two- line PLIF technique, and the OH-field width. Both measurements demonstrate the existence of a diffusion-limited frequency response of flames subjected to a time-varying flow field. At the 30 Hz and 50 Hz forcing frequencies, the maximum reaction-zone temperature and the OH-field width were found to respond quasi-steadily. At higher forcing frequencies, 100 and 200 Hz, however, transient behavior is evident from the phase relationship between the imposed sinusoidal strain and the resulting OH-field width and peak temperature.

The measured values of the OH-field widths (FWHM) were fit well by an offset sine function. For smaller amplitude oscillations, when the oscillation amplitude (from the sine-curve fit) is normalized by the steady strain rate and plotted against the non-dimensional flow field frequency, it collapses onto a single line with a steep negative slope. This result provides validation to the numerical study of Egolfopoulos and Campbell [4]. An implication of the

Stokes plot is that the fluctuations of the reaction zone width are decreasing monotonically with increasing forcing frequency in a predictable manner for the conditions considered.

As previously stated, the reaction zone continued to respond in a sinusoidal manner at all frequencies which signals that the break down in the quasi steady response is not a result of the chemical kinetics, but a result of the mixture field response. The mixture field response was explained in the context of a diffusion limited response of the reaction zone.

Acknowledgements

This work was supported by the Army Research Office, under ARO Grant DAAH04-95-10230 (Dr. David Mann, monitor), the Air Force Office of Scientific Research (Dr. Julian Tishkoff, monitor), and the Propulsion Directorate of the Air Force Research Laboratory, Wright-Patterson AFB.

References

1. Peters, N., *Prog. Energy Comb. Sci.*, **10**, pp. 319-339 (1984).
2. Bray, K. N. C., Peters, N., *Turbulent Reacting Flows*, Academic Press Ltd, (1994), p. 63.
3. Im, H. G., Law, C. K., Kim, J. S., Williams, F.A., *Combust. Flame* **100**, pp. 21-30 (1995).
4. Egolfopoulos, F. N., Campbell, C. S., *J. Fluid Mech.* **318**, pp. 1-29 (1996).
5. Darabiha, N., *Combust. Sci. and Tech.* **86**, pp. 163-181 (1992).
6. Brown, T. M., Pitz, R. W., Sung, C. J., Proc. Combust. Inst. 27: 703-710 (1998).
7. Puri, I. K., Seshadri, K., *Combust. Flame*, **65**, 137-150 (1986).
8. DeCroix, M. E., Roberts, W. L., *Comb. Sci. and Tech* **160**, pp. 165-190 (2000).
9. Welle, E. J., Roberts, W. L., Donbar, J. M., Carter, C.D., DeCroix, M.E., Proc. Combust. Inst. 28: 2021-2027 (2001).
10. Palmer, J. L., Hanson, R. K., *Applied Optics* **35**, pp. 485-498 (1996).
11. Seitzman, J. M., Hanson, R. K., DeBarber, P. A., Hess, C. F., *Applied Optics* **33**, pp. 4000-4012 (1994).
12. Seitzman, J. M., Hanson, R. K*., Appl. Phys. B* **57**, pp. 385-391 (1993).
13. Barlow, R. S., and Carter, C. D., *Combust. Flame* **97**, pp. 261-280 (1994).

14. Barlow, R. S., Sandia National Laboratories, Personnel Communication.
15. Sung, C. J., Law, C. K., and Axelbaum, R. L., *Comb. Sci. Tech.* **99**, pp. 119-132 (1994).
16. Im, H., G., Chen, J. H., Chen, J., Combust. Flame, **118**, pp. 204-212 (1999
17. Barlow, R.S., Dibble, R.W., Chen, J.Y., Lucht, R.P., *Combust. Flame* **82**, pp. 235-251 (1990).
18. Brown, T.M., Pitz, R.W., Sung, C.J., *The 27th Symposium of the Combustion Institute*, pp. 703-710 (1998).
19. Peters, N., Turbulent Combustion, Cambridge Univ. Press, Cambridge, U.K., 2000, p. 184.

Table 5-1: Flow conditions for the counterflow diffusion flame burner.

	Air slpm	Propane slpm	Nitrogen slpm
SSR 23	4.76	3.9	11
SSR 44	9.6	7.6	14.5
SSR 74	14.4	11.5	21.7

Table 5-2: The calibration intensity ratios used and the adiabatic flame temperatures for various equivalence ratios.

ϕ	$I_{Q1(5)}/I_{Q1(14)}$	T_{ad} (K)
0.75	0.85	1919
0.8	0.783	1996
0.85	0.74	2069
0.9	0.709	2134
0.975	0.656	2211

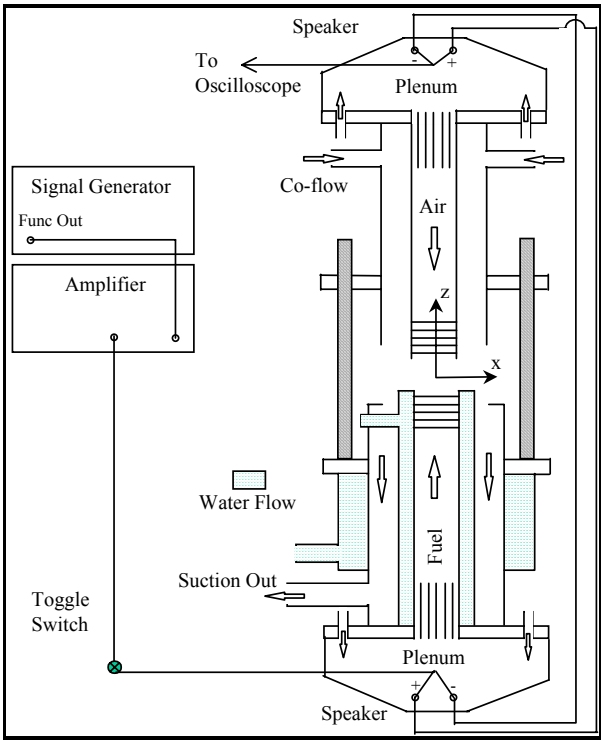

Figure 5-1: Schematic of counterflow diffusion flame burner.

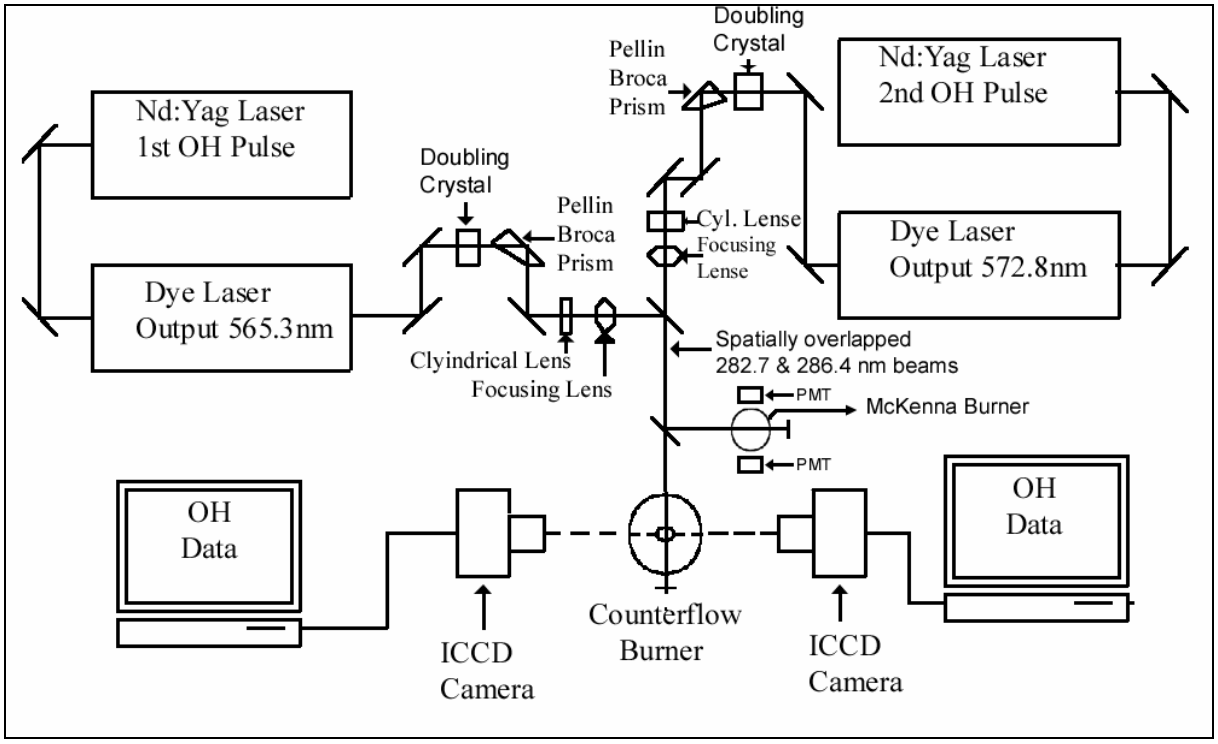

Figure 5-2: Optical layout for the simultaneous two-line OH thermometry.

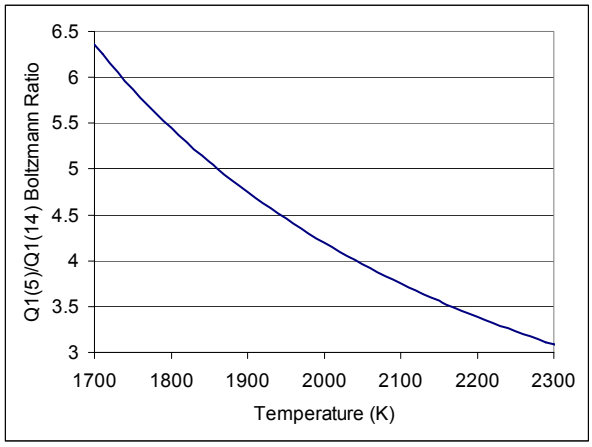

Figure 5-3: Ratio of the Boltzmann fraction for the $Q_1(5)$ and $Q_1(14)$ transitions as a function of temperature.

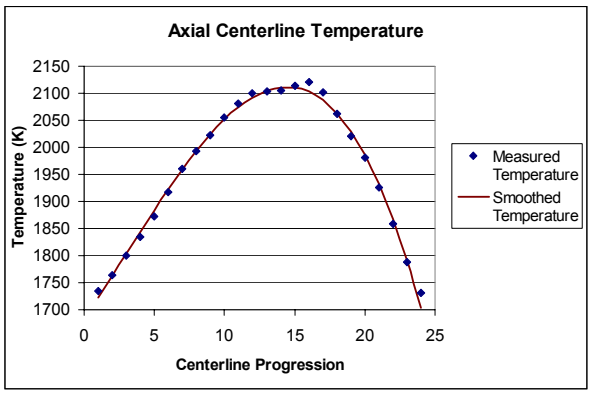

Figure 5-4: Centerline temperature measurements in the flame with SSR of 44 s^{-1}. T_{max} for this case from the smoothed curve is 2113 K.

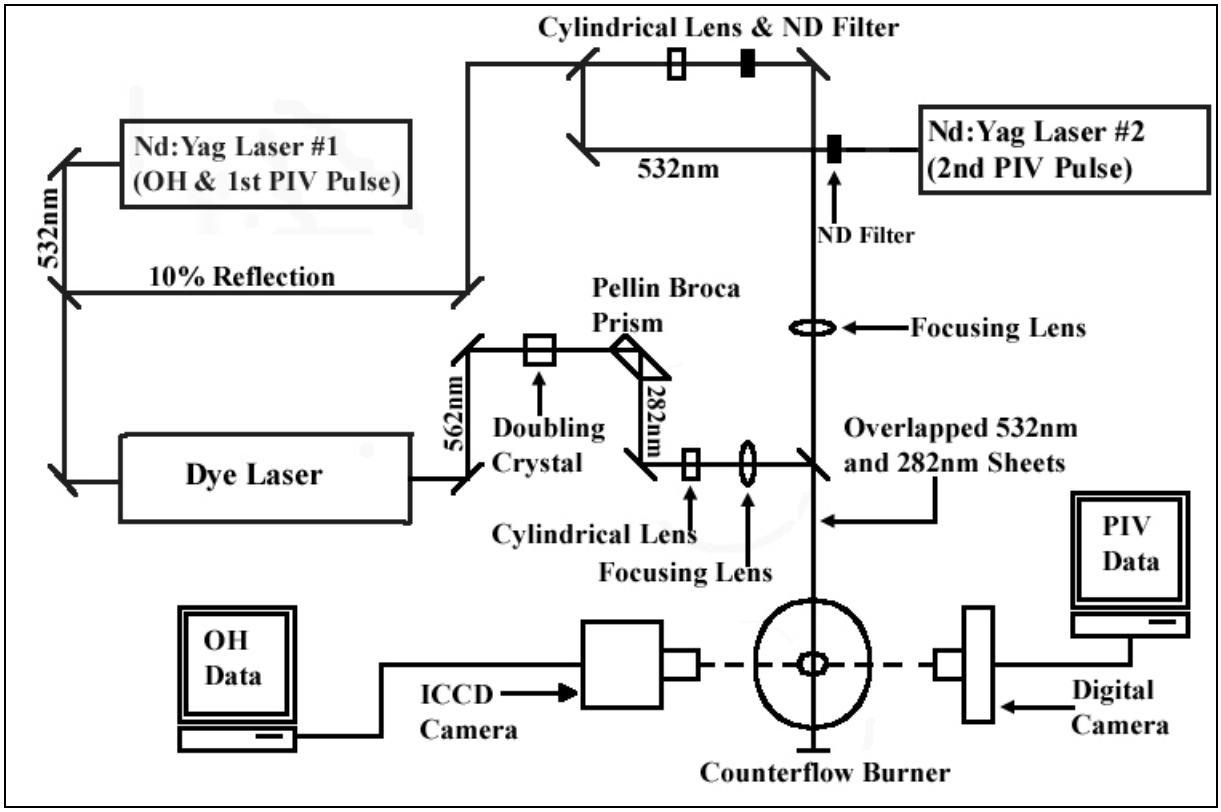

Figure 5-5: Optical layout for the simultaneous OH-PLIF/PIV measurements.

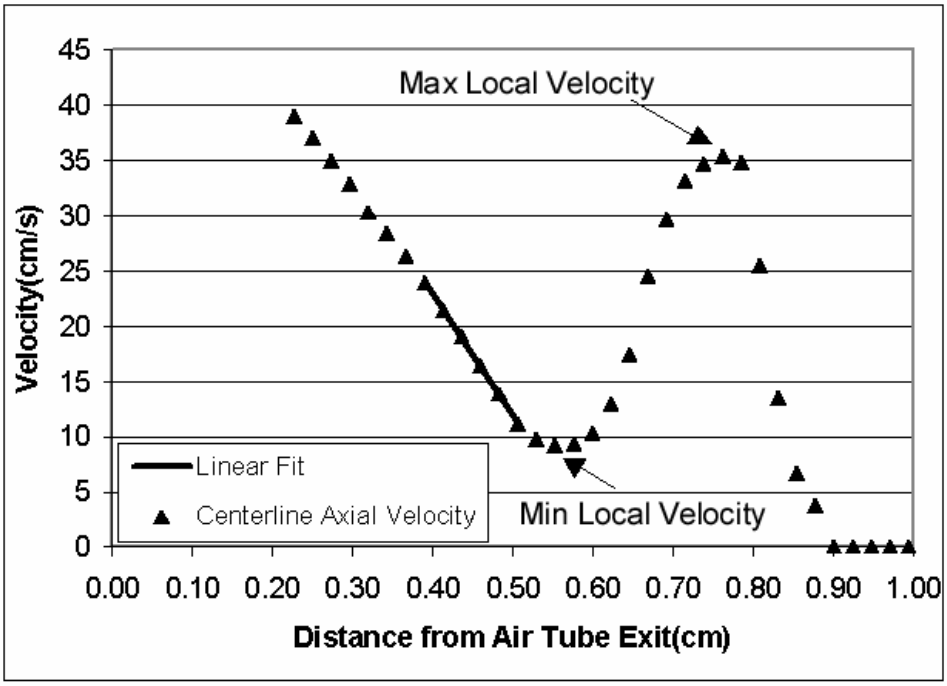

Figure 5-6: Velocity field data showing the fitted line for strain rate calculations. Also shown are the velocities used to determine the dilatation velocity.

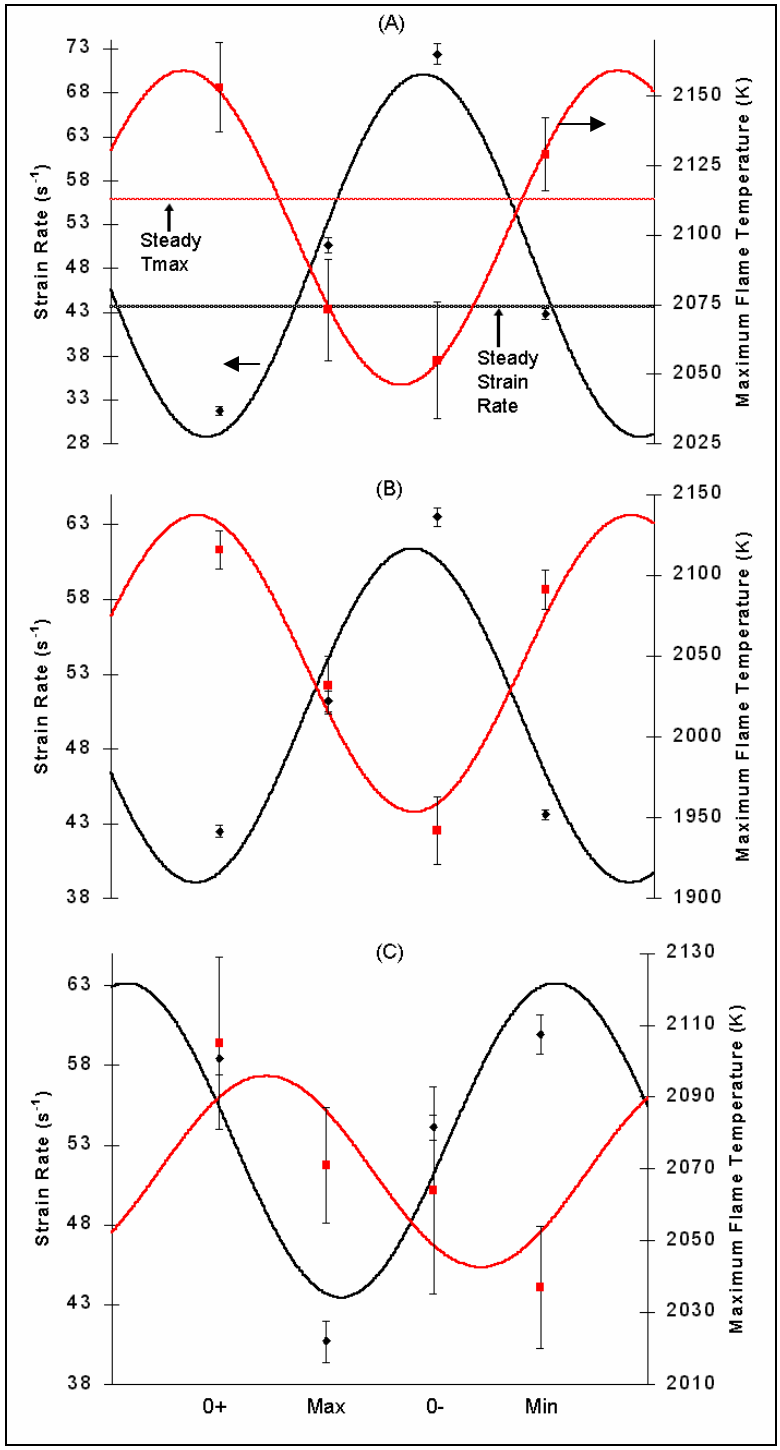

Figure 5-7: Maximum reaction-zone temperature, T_{max} (Boxes), and instantaneous strain rate (Diamonds) at 30 Hz (A), 50 Hz (B), 200 Hz (C) at the four phases. The horizontal lines are the steady values of T_{max} and the strain rate. The solid lines are sinusoidal fits to the measured data points at the four temporal.

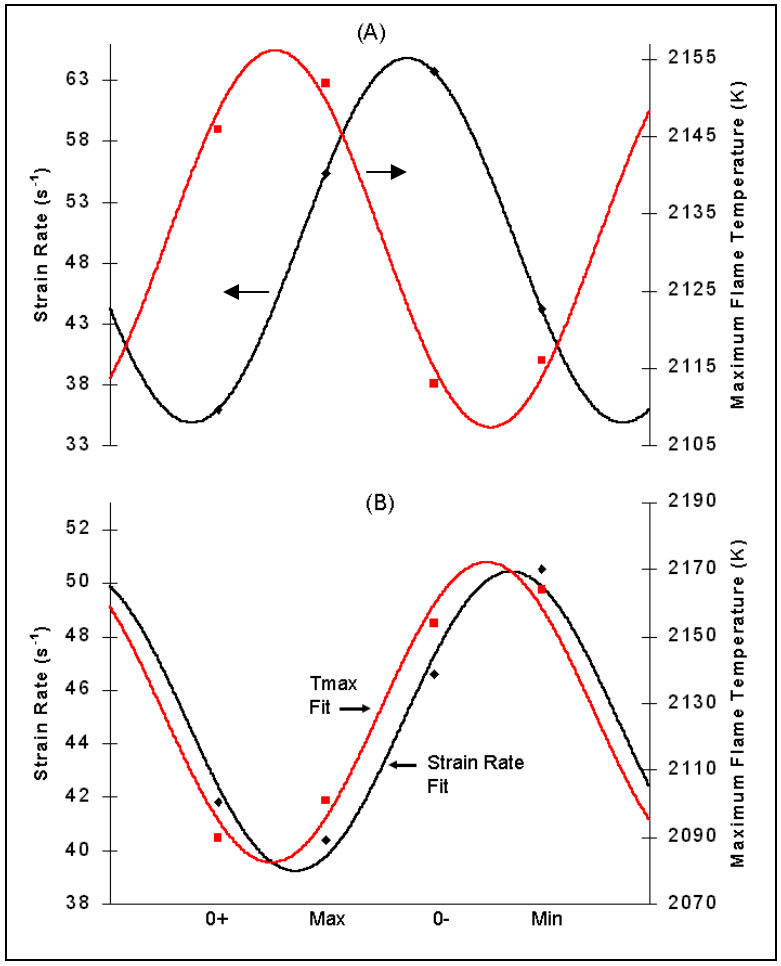

Figure 5-8: Maximum reaction-zone temperature, T_{max} (squares), and instantaneous strain rate (diamonds) at 30 Hz (A) and 200 Hz (B) at the four phases.

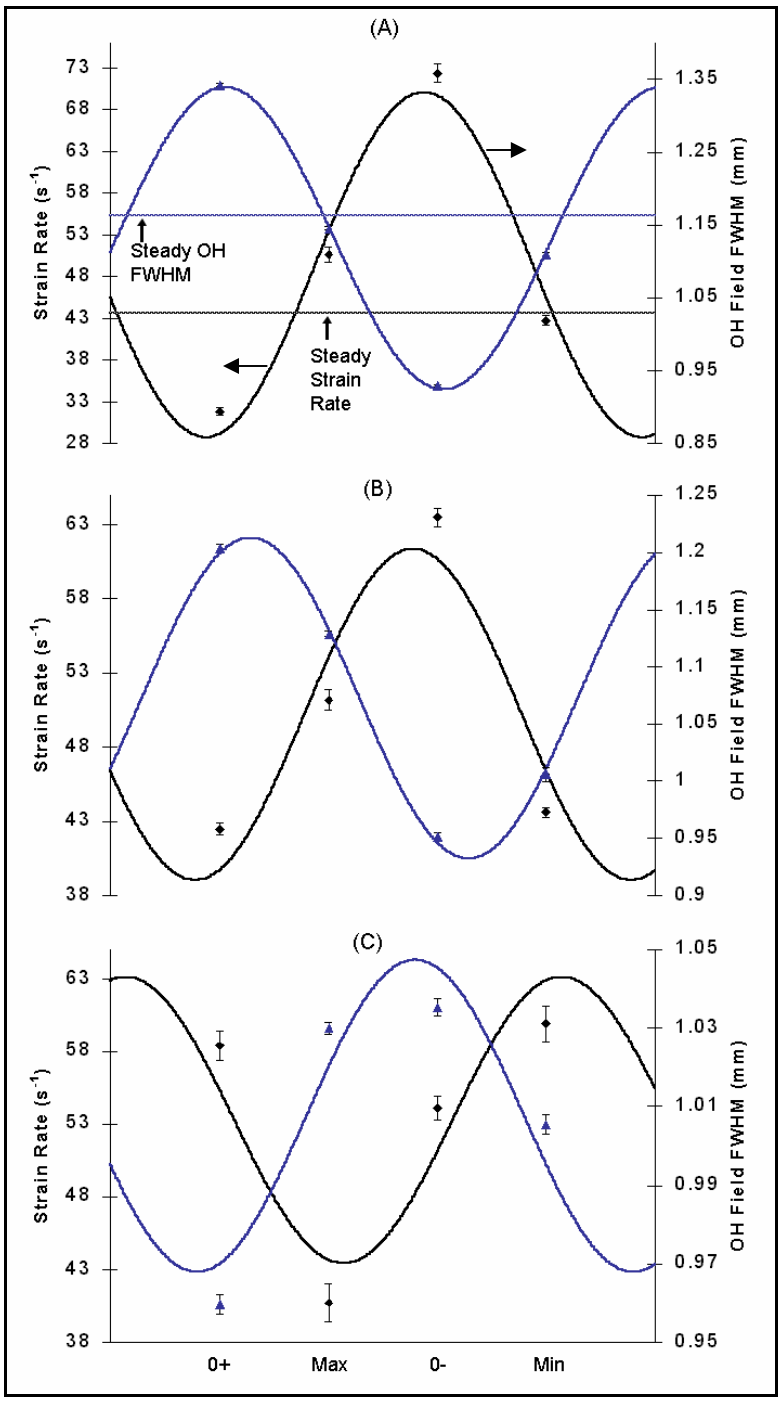

Figure 5-9: Instantaneous strain rates (dashed lines) and the OH field's FWHM (solid lines) at 30- (A), 50- (B), and 200-Hz (C) forcing frequencies. The horizontal dashed and solid line represents the steady strain rate and OH field FWHM respectively.

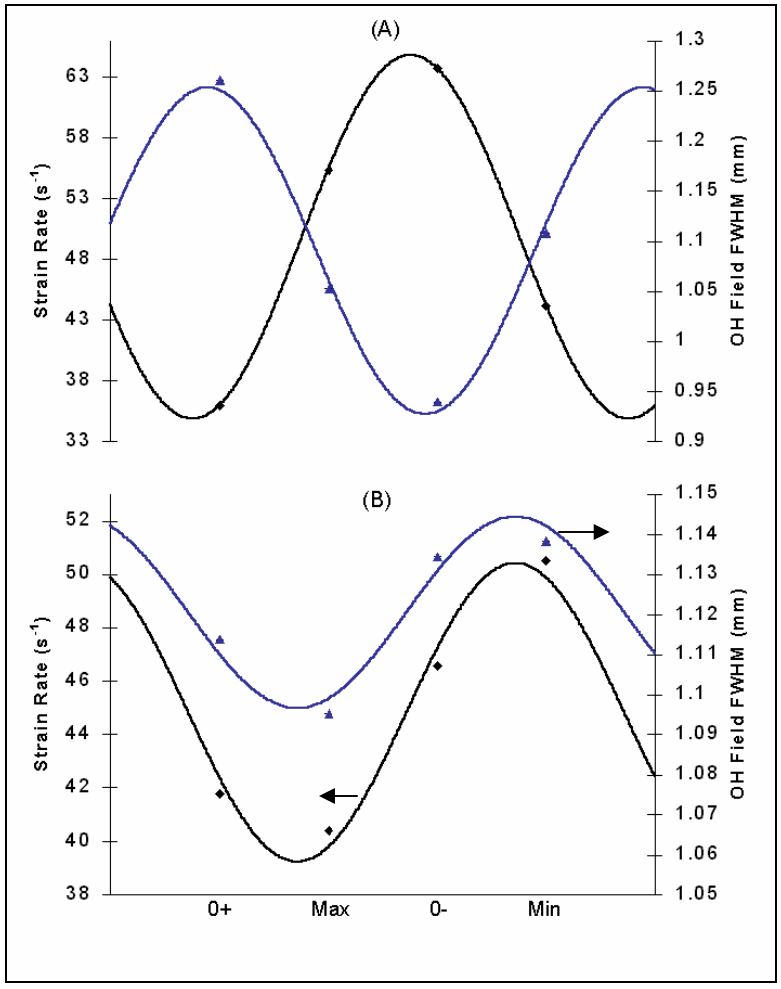

Figure 5-10: OH field FWHM and instantaneous strain rate at 30 Hz (A) and 200 Hz (B) at the four phases.

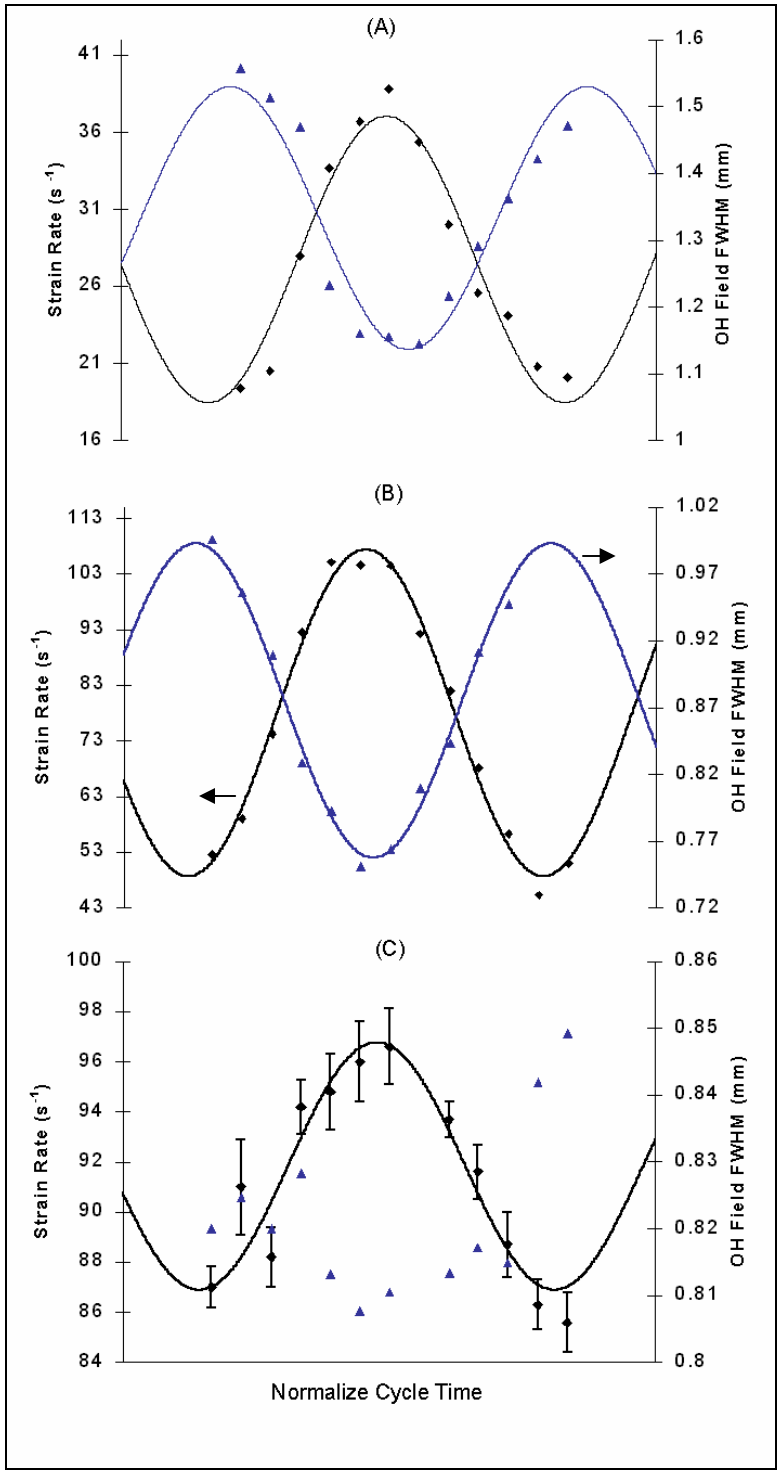

Figure 5-11: High-resolution strain rate (Diamonds) and OH-field width (Triangles) for a SSR 24s^{-1} at 30 Hz (A), SSR 84 s^{-1} at 30 Hz (B), and 500 Hz (C).

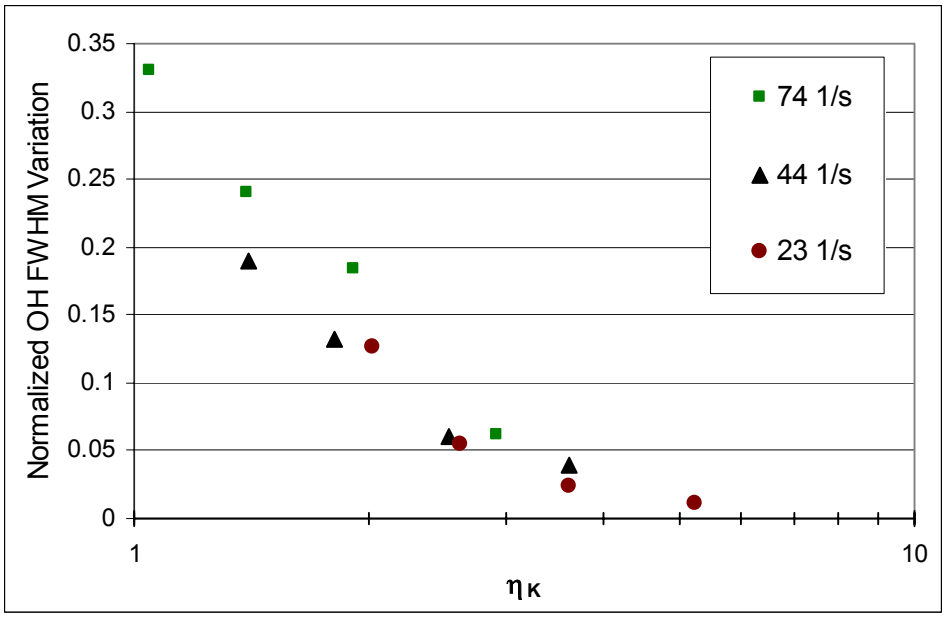

Figure 5-12: Amplitude of the OH width oscillation normalized by the mean value as a function of the Stokes parameter η_k.

6 An Experimental study of the Quasi-Steady Response of a Counter-Flow Diffusion Flame and the Appropriateness of using Strain Rate as a substitute for Scalar Dissipation Rate

Abstract

The Scalar dissipation rate (χ) is of fundamental interest in diffusion flame studies as it is a parameter that describes the transport of reactants to the flame front. Unfortunately, this quantity is very difficult to determine experimentally. Typically, a Raman or Raman-Raleigh experimental setup is used to measure necessary species and thereby permit the determination of χ. A simpler approach in a counter-flow diffusion flame is to use the strain rate, which is determined from velocity measurements as a substitute for the scalar dissipation rate as it is much easier to measure experimentally. According to traditional flamelet theory, a "quasi-steadily" responding Flamelet can be described by the mixture fraction and the scalar dissipation rate. Furthermore, for a counter-flow diffusion flame configuration the scalar dissipation rate can be shown to be directly proportional to the local flow field axial strain rate. In this study, a transient flow-field was imposed upon a counter-flow propane/air diffusion flame and quantitative measurements of velocity, using Particle Image Velocimetry (PIV), and OH measurements, using Planar Laser Induced Fluorescence (PLIF), were made simultaneously. These non-intrusive measurements were performed to spatially and temporally resolve flow-field and flame characteristics as a function of initial steady strain rate and forcing frequency to

determine the appropriateness of using strain rate instead of scalar dissipation rate for the experimentally constructed Flamelet.

Introduction

Flamelet theory is a method that characterizes turbulent diffusion flames as a collection of strained, laminar, one-dimensional flamelets [1,2], which are dependent upon the mixture fraction and instantaneous scalar dissipation rate. The scalar dissipation rate can be interpreted as the inverse of a characteristic diffusion time and due to the transformation that leads to this parameter, it incorporates the effects of convection and diffusion normal to the surface of the stoichiometric mixture [1]. As a result, this parameter is of prime interest in the study of Flamelet Theory [1] and turbulent combustion in general [3]. To experimentally determine the scalar dissipation rate (χ), the mixture fraction (Z) must be determined. This dependence is illustrated in Equation 6-1 below.

Equation 6-1 Scalar dissipation rate defined

$$\chi \equiv 2 \cdot D \cdot (\nabla Z \cdot \nabla Z)$$

In Equation 1 above, D is the molecular diffusivity of the gaseous mixture. Raman measurements [4] or Raman/Raleigh measurements [5,6,7,8,9] have been performed to measure mixture fraction. These methods are valuable but are equipment intensive and can suffer from signal-to-noise (SNR) limitations. More recently, a NO-PLIF/Raleigh technique has been demonstrated that allows for the determination of scalar dissipation rate with much greater SNR [10]. The above mentioned techniques all require extensive measurement systems with inherent complications so it is prudent to examine cases where simpler methods may be used to infer information about the scalar dissipation rate.

The purpose of this investigation was to quantify the strain rate and relative OH concentration fluctuations in a propane-air flame subjected to sinusoidal velocity fluctuations. A counter-flow diffusion flame burner was used because it has the same scalar structure as a Flamelet in the mixing zone of a turbulent reacting flow-field [1]. PIV measurements were used to quantify the strain rate, while simultaneously; the OH field was measured using PLIF. Fundamental relationships predicted by Flamelet theory are applied to the measured parameters in order to determine the suitability of using the strain rate to quantify Flamelet response for the transient flow field considered in this study and to comment on the appropriateness of using strain rate as a substitute for scalar dissipation rate.

Experimental Apparatus and Procedure

A schematic of the counter-flow diffusion flame burner used in this study is shown in Figure 6-1. Briefly, the burner is a modification of the design described by Puri and Seshadri [11], and described in detail in [12]. The oxidizer and fuel tubes are 25.4 mm in diameter and have a 12.7 mm separation distance. Plenums located on the fuel and oxidizer sides are capped with 20 cm loudspeakers, which impose the velocity fluctuations and are driven by an amplified signal generator.

An unsteady flow-field was imposed on the counter-flow diffusion flame by inputting a sinusoidal voltage signal to the speakers. The velocity and OH field measurements were made as a function of initial steady strain rate (SSR) and forcing frequency. These measurements were made at four temporal locations within the sinusoidal voltage oscillation applied to the speakers: the zero amplitude with positive slope (0+), maximum amplitude (Max), zero amplitude with

negative slope (0-), and minimum amplitude (Min). The forcing frequencies considered in this study were 30, 50, 100, and 200 Hz.

The PIV measurements were made using two frequency doubled Nd:YAG lasers (λ = 532 nm) and the experimental setup is illustrated in Figure 6-2. The PIV images were recorded using a Kodak interline-transfer digital camera fitted with a 105 mm lens. An interference filter centered at 532 nm with a FWHM of 3 nm was used to block background flame emission.

The OH measurements were made using a Nd:YAG pumped dye laser. The $R_1(8)$ transition of the $A^2\Sigma+ \leftarrow X^2\Pi(1,0)$ band was excited and detected using a Princeton Instruments ICCD camera. The $R_1(8)$ transition was chosen because of its reduced signal level sensitivity to temperature fluctuations over the temperature range expected (small changes in the ground state population). A more exhaustive explanation of the experimental setup can be found in [13].

The response of the reaction zone to velocity oscillations was characterized by measuring the full width at half maximum (FWHM) of the OH field. The strain rate was determined by evaluating the gradient of the axial velocity profile at the centerline of the burner on the oxidizer side of the stagnation plane. A line was fit to the velocity data prior to the preheat zone and the strain rate (K) was then calculated from the fitted line. Figure 6-3 illustrates the location of the fitted line relative to the preheat zone. Twenty OH and PIV images were taken and averaged at each of the four temporal locations within the speaker oscillation for each data point reported. No corrections for thermophoretic effects have been performed on the velocity measurements, as previous studies have shown that accurate velocity measurements can be performed prior to the preheat zone without accounting for thermophoresis [14].

Results and Discussion

For a propane/air counter-flow diffusion flame, the transport of reactants to the flame front on the oxidizer side is a result of convection and diffusion processes where the transport of the fuel is strictly via diffusion. The direct coupling of this convective-diffusive transport process has led to the use of the strain rate on the oxidizer side to characterize reactant delivery and flame response [15,16,18]. With traditional Flamelet Theory, a direct relationship can be derived that relates the strain rate to the stoichiometric scalar dissipation rate (χ_{st}) [18]. Equation 6-2 below shows this relation for an axis-symmetric counter-flow diffusion flame.

Equation 6-2 Stoichiometric scalar dissipation rate derived in ref. 18

$$\chi_{st}(Z_{st}) = \frac{2K}{\pi}\exp\left[-2\left(\mathrm{erf}^{-1}[2Z_{st}]^2\right)\right]$$

In Equation 6-2 above, Z is the mixture fraction, which is a conserved scalar and K is the axial strain rate. The scalar dissipation rate is a fundamental parameter as it describes the molecular mixing and couples the reaction zone response to the flow field.

Figure 6-4 illustrates the results of the simultaneous PIV/OH-PLIF measurements for forcing frequencies of 30 and 200 Hz for a flow with an unforced steady strain rate (SSR) of 44 s^{-1}. Also, the amplitudes of the oscillations imposed on the flames reported here did not exceed half the extinction amplitude [12]. For a Flamelet that is responding quasi-steadily, an increase in strain rate (increasing scalar dissipation rate) is accompanied by an increase in concentration

and temperature gradients. As a result, the flame will cool and the reaction zone will thin. This thinning of the reaction zone has been noted in previous works [13,18,19]. For the 30 Hz oscillation case in Figure 6-4, this quasi-steady response is unambiguous and the appropriateness of using strain rate as a surrogate for scalar dissipation rate is apparent. With an increasing strain rate ($\chi\uparrow$) we find a thinning reaction zone thickness and with a decreasing strain rate ($\chi\downarrow$) the reaction zone responds by growing in thickness. Effectively, the strain rate and the reaction zone thickness are ~ 180º out of phase. In stark contrast to this behavior, we find the opposite trend is present when the flame is forced at a frequency of 200 Hz. For the 200 Hz oscillation, the strain rate and the reaction zone thickness are approximately in phase. It is clear that at this condition using the strain rate as a predictor of flame behavior may be inappropriate and other methods must be employed. Also, it is still unclear as to whether strain rate is still a good surrogate for χ_{st}.

In a numerical study conducted by Im et al. [20], a comparison was conducted between the strain rate and the scalar dissipation rate and it was found that for unsteady flames with high frequency oscillations strain rate was an unsuitable measure of flame response. In that study, it was found that a monotonically increasing phase lag occurred between χ_{st} and the quasi steady value where the phase lag for the strain rate did not increase monotonically over the frequency ranges reported. For their methane/air flame, the strain rate phase lag increased monotonically up to a forcing frequency 200 Hz, but then experienced a decrease. As a result it was suggested that although χ_{st} was not in phase with the flame response, its phase was increasing in what appears to be a predictable fashion, which makes χ_{st} a more suitable marker for flame response.

The non-monotonic phase lag found at elevated frequencies in ref. 20 is likely a result of the diffusion limited frequency response of the flame. With increasing forcing frequency, a phase lag occurs between the volumetric expansion resulting from the heat release and the quasi steady value. Figure 6-3shows the strong effects that the volumetric expansion resulting from heat release has on the flow-field. If an isothermal potential flow was considered originating at the first measurement location in Figure 6-3, we would find a dramatically different flow-field structure and strain rate as illustrated by the dashed line. Consequently, the strain rate variations will follow the lagging volumetric expansion so long as the variations of the volumetric expansion are large relative to the flow field variations. On the other hand, it has been shown experimentally [15] and computationally [16] that the amplitude of the oscillations of various flame parameters reduces with increasing forcing frequency, thus reducing the effects of the volumetric expansion on the flow field. It has been postulated that the cause of this is likely the diffusion process of the oxidizer to the flame front [15, 16]. The result of this is that once the amplitude of the volumetric expansion variations becomes small, the strain rate fluctuations begin to follow the flow field variations. This was found to be the case and is illustrated in Figure 6-5 which shows that the phase difference between the strain rate and the velocity fluctuations are decreasing with increasing forcing frequencies and going into phase. Therefore, the hope of using a correlation which relates the flame response to strain rate fluctuations is not likely due to the non-monotonic lag of the strain rate with increasing forcing frequency brought about by the attenuated response of the volumetric expansion with increasing forcing frequency.

In another computational study, the issue of the transient response of the flamelet has been approached using a Lagrangian description [21]. They defined a diffusion time that helps to quantify the effects of the flow field's rapid changes on the steady nature of the flamelet response as shown in Equation 6-3.

Equation 6-3 Diffusion time defined in ref. 21.

$$t_{\chi} = \frac{(\Delta Z)^2}{\tilde{\chi}_{st}}$$

Where ΔZ is considered to be the flame thickness in mixture fraction space, which has also been shown to be proportional to $(\Delta Z)_F \propto 1/\sqrt{K}$ [17] and $\tilde{\chi}_{st}$ is the Favre mean stoichiometric scalar dissipation rate. It was suggested that if the time necessary to exchange mass and energy over ΔZ is small relative to the Lagrangian time, the flamelet is able to follow changes in the scalar dissipation rate rapidly. If this is not the case, they proposed that more unsteady terms in the computations must be retained to properly describe the flamelet response, which further complicates the description of the flame experimentally.

The response of the flame can also be viewed from the perspective of other expectations that result from theory which predicts that the reaction zone thickness scales with the inverse of the strain rate ($\delta_F \propto 1/\sqrt{K}$). Figure 6-6 is a plot of the low frequency (30 and 50 Hz) and high frequency (100 and 200 Hz) response of the reaction zone thickness for various initial steady strain rates. For the low frequency response, the data was found to follow the expected quasi-steady flamelet trend very closely where the high frequency response plot does not follow this trend. The high frequency response illustrates that the flame thickness is responding to the mean

strain rate of the flow where the SSR 44 s^{-1} has a mean OH field thickness of ~1.1 mm and the SSR 74 s^{-1} condition has a thinner mean OH field thickness of ~0.9 mm. In a study performed by Donbar et al. [22], simultaneous CH-PIV images were collected and it was found that the variations of the CH field thickness were not in phase with the strain field which indicated that the CH layer was not responding to the high-frequency components of the instantaneous strain rate. This is consistent with the results reported in this study in the sense that at elevated forcing frequencies the flames were found to respond to the mean strain rate but not to the instantaneous strain rate.

The physical mechanism responsible for this behavior is the diffusion limited frequency response of the reaction zone that has been sighted in previous experimental studies [13,15] but first described well in [16]. Close to the reaction zone on the oxidizer side, the concentration gradients become very steep near the reaction zone and the major transport mechanism for the oxidizer becomes diffusion. Due to this fact, there is a certain diffusion layer thickness (δ_D), which has a suggested form of Equation 6-4 [16], and there is a time associated with this diffusion process.

Equation 6-4 Diffusion layer thickness as suggested by Egolfopoulos et al.

$$\delta_D \approx \left(\frac{D}{K}\right)^{1/2}$$

At the edge of this diffusion layer the reactants are delivered via convective velocities. When the characteristic time scale of the fluctuations of reactant delivery at the edge of this layer is much longer than the time associated with diffusion, the flame appears to quickly adjust to flow-field

fluctuations. When the characteristic time scale of the changes in the convective velocities (forcing frequency in this study) are on the order of the diffusion time, a phase lag appears in the reaction zone response and this lag will continue to increase with increasing forcing frequency [13,16]. This is illustrated in Figure 6-4 for the 200 Hz oscillating condition. The reaction zone is still responding to the fluctuations in reactant delivery, but at a delayed time. The failure of the instantaneous strain rate to act as a predictor of the flame response is a result of the phase shifting heat release and thermal expansion of the flow-field as previously described in this paper.

Conclusions

OH planar laser-induced fluorescence (PLIF) and particle image velocimetry (PIV) have been used to study the quasi-steady response of laminar C_3H_8-air counter-flow diffusion flames to evaluate the flame response with increasing forcing frequency and to determine when the strain rate is a suitable substitute for the scalar dissipation rate. This is of great interest as the number of studies that have and will be performed using counter-flow diffusion flames is beyond referencing. This is crucial as more and more studies go beyond steady measurements in counter-flow diffusion flames in an attempt to mimic the transient environments present in practical combustion systems. It was found that at low forcing frequencies (long characteristic time scales of flow field fluctuations) the flame responds quasi-steadily and the strain rate is an appropriate surrogate for the scalar dissipation rate. At high forcing frequencies, the direct correlation between strain rate and scalar dissipation rate is likely no longer valid and is attributed to the attenuation of the volumetric expansion in the heat release zone. It was found

that the reaction zone continued to respond in a sinusoidal manner which signals that the break down in the correlation is not a result of the chemical kinetics, but a result of the mixture field response. This mixture field response was explained in the context of a diffusion limited response of the reaction zone. Ultimately, if a flame is subjected to transient flow field with very small time scales, it is likely that strain rate will not be appropriate to describe flame response.

Acknowledgements

This work was supported by the Army Research Office, under ARO Grant DAAH04-95-10230 (Dr. David Mann, monitor), the Air Force Office of Scientific Research (Dr. Julian Tishkoff, monitor), and the Propulsion Directorate of the Air Force Research Laboratory, Wright-Patterson AFB.

References

1. Peters, N., Prog. Energy Comb. Sci., 10:319-339 (1984).
2. Bray, K.N.C., Peters, N., Turbulent Reacting Flows, Academic Press Ltd, p. 63 (1994).
3. Bilger, R. W., Proc. Combust. Inst. 22:475-488 (1988).
4. Kyritsis, D. C., Santoro, V. S., Gomez, A., Eastern States Section of the Combustion Institute, pp. 320-323 (2001).
5. Stårner, S. H., Bilger, R.W., Dibble, R.W., Barlow, R.S., Combust. Sci and Tech., Vol. 86, pp. 223-236 (1992).
6. Stårner, S. H., Bilger, R.W., Frank, J. H., Marran, D. F., Long, M. B., Combust. Flame, 107:307-313, (1996).

7. Frank, J. H., Lyons, K. M., Marran, D. F., Long, M. B., Stårner, S. H., Bilger, Proc. Combust. Inst. 25:1159-1166 (1994).
8. Fielding, J., Schaffer, A. M., Long, M. B., Proc. Combust. Inst. 27:1007-1014 (1998).
9. Brockhinke, A., Kohse-Höinghaus, K., Optics Letters Vol. 21 No. 24, pp. 2029-2031 (1996).
10. Sutton, J. A., Driscoll, J. F., To appear in Proc. Combust. Inst. 29.
11. Puri, I.K., Seshadri, K., Combust. Flame, 65, 137-150 (1986).
12. DeCroix, M.E., Roberts, W.L., Comb. Sci. Tech v146, pp.57-84, (1999).
13. Welle, E. J., Roberts, W. L., Donbar, J. M., Carter, C.D., DeCroix, M.E., Proc. Combust. Inst. 28: 2021-2027 (2001).
14. Sung, C.J., Kistler, M., Nishioka, M., Law, C.K., Combust. Flame, 105:189-201 (1996).
15. Welle, E. J., Roberts, W. L., Donbar, J. M., Carter, C.D., Submitted to Combust. Flame.
16. Egolfopoulos, F.N., Campbell, C.S., J. Fluid Mech., 318:1-29 (1996).
17. Peters, N., "Turbulent Combustion", Cambridge Press, pp. 184 (2000).
18. Sung, C.J., Liu, J.B., Law, C.K., Combust. Flame 102:481-492 (1995).
19. Pellett, G.L., Isaac, K.M., Humphreys, JR., W.M., Gartrell, L.R., Roberts, W.L., Dancey, C.L., Northam, G.B., Combust. Flame 112:575-592 (1998).
20. Im, H. G., Chen, J. H., Chen, J., Combust. Flame 118:204-212 (1999).
21. Pitsch, H., Chen, M., Peters, N., Proc. Combust. Inst. 28, 1057-1064.
22. Donbar, J. M., Driscoll, J., F., Carter, C. D., Combust. Flame 125:1239-1257 (2001).

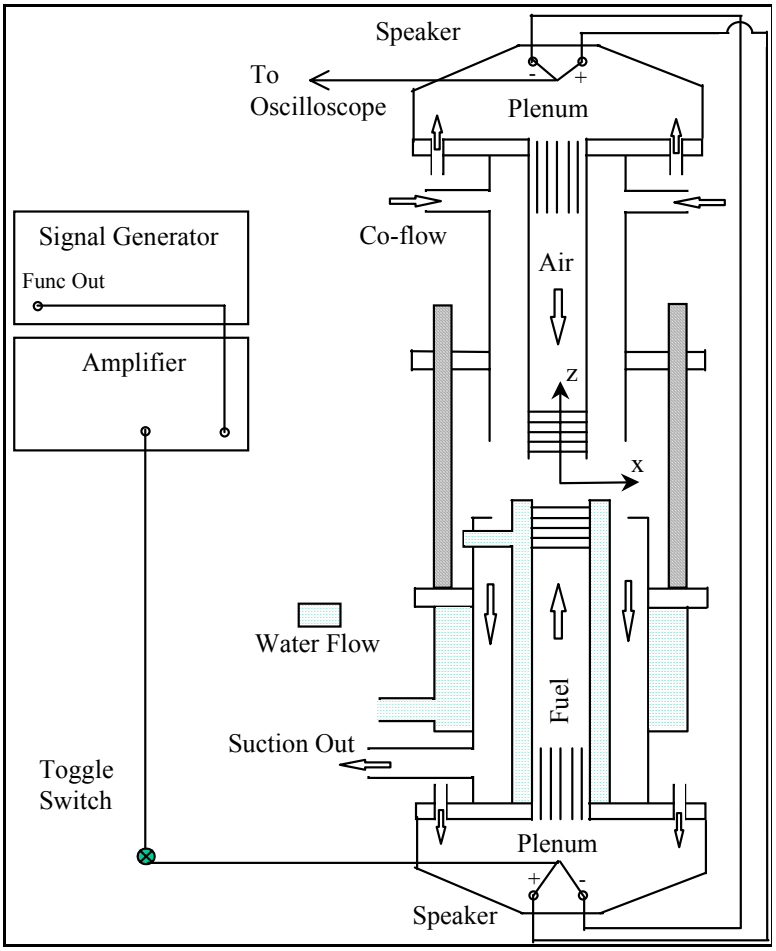

Figure 6-1 Schematic of the counter-flow diffusion flame burner

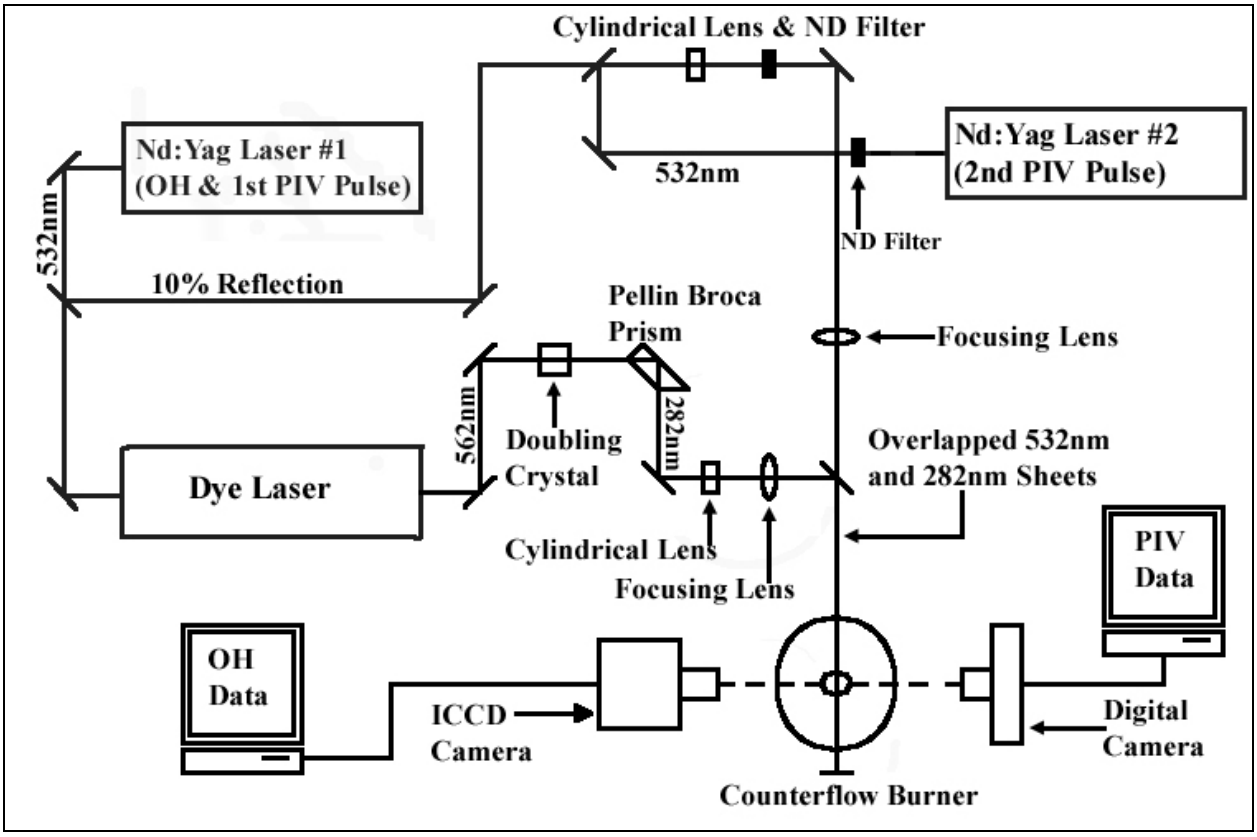

Figure 6-2 Optical Layout for PIV and OH-PLIF measurements

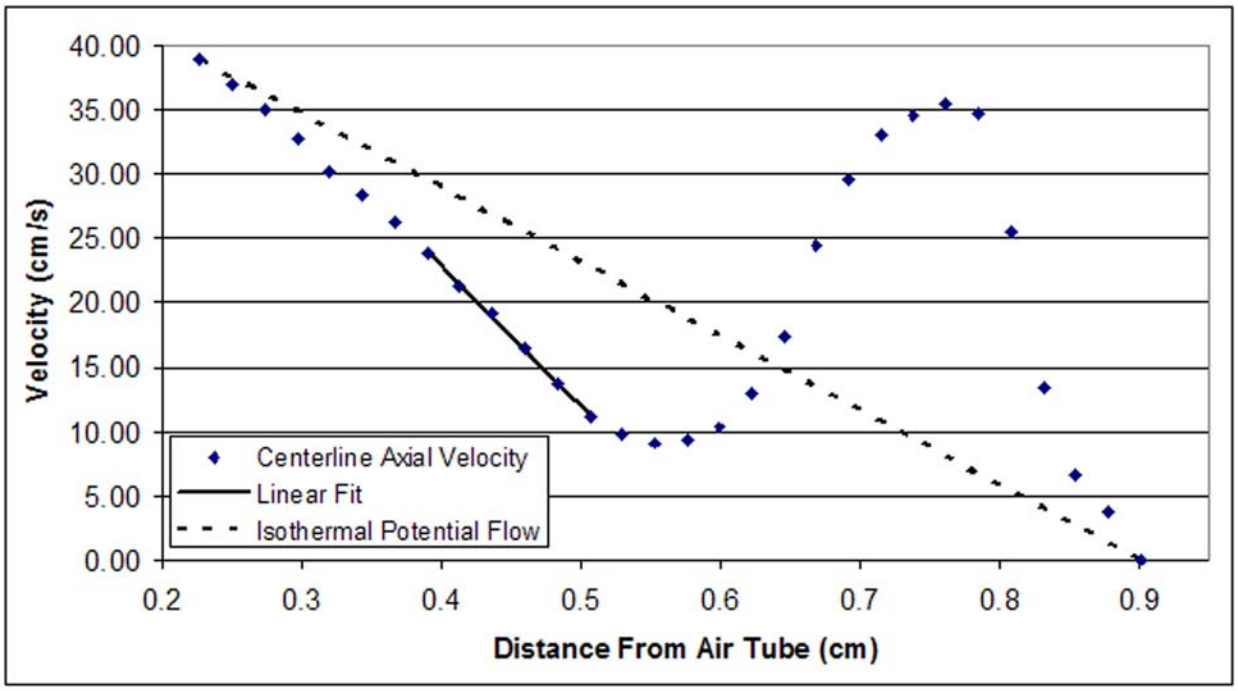

Figure 6-3 Velocity field data showing the fitted line for strain rate calculations. Also shown is an isothermal potential flow velocity profile.

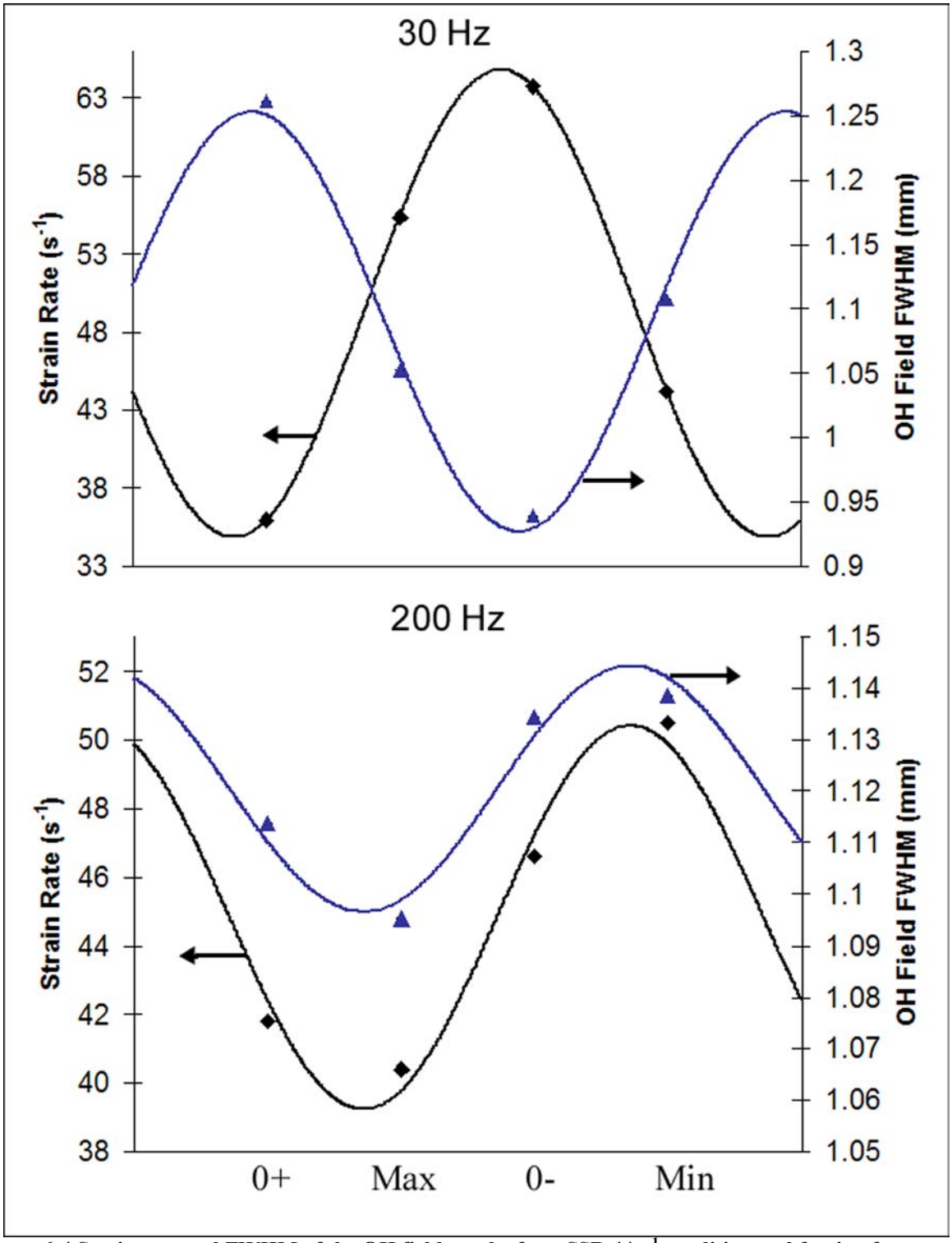

Figure 6-4 Strain rate and FWHM of the OH field results for a SSR 44 s^{-1} condition and forcing frequencies of 30 and 200 Hz with fitted offset sine function

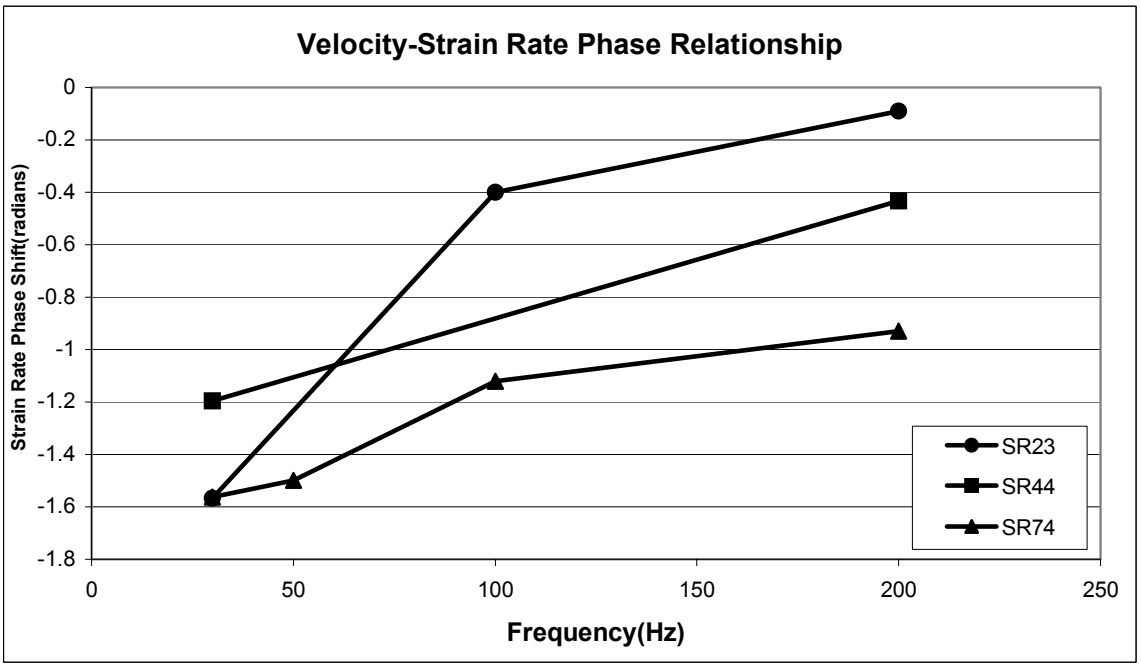

Figure 6-5 Phase difference relationships between the air velocity and the strain rate as a function of frequency for initial steady strain rates of 23·s^{-1}, 44·s^{-1}, and 74·s^{-1}. The circles connected by solid lines represent the 23·s^{-1} data, the squares represent the 44·s^{-1} data, and the triangles represent the 74·s^{-1} data

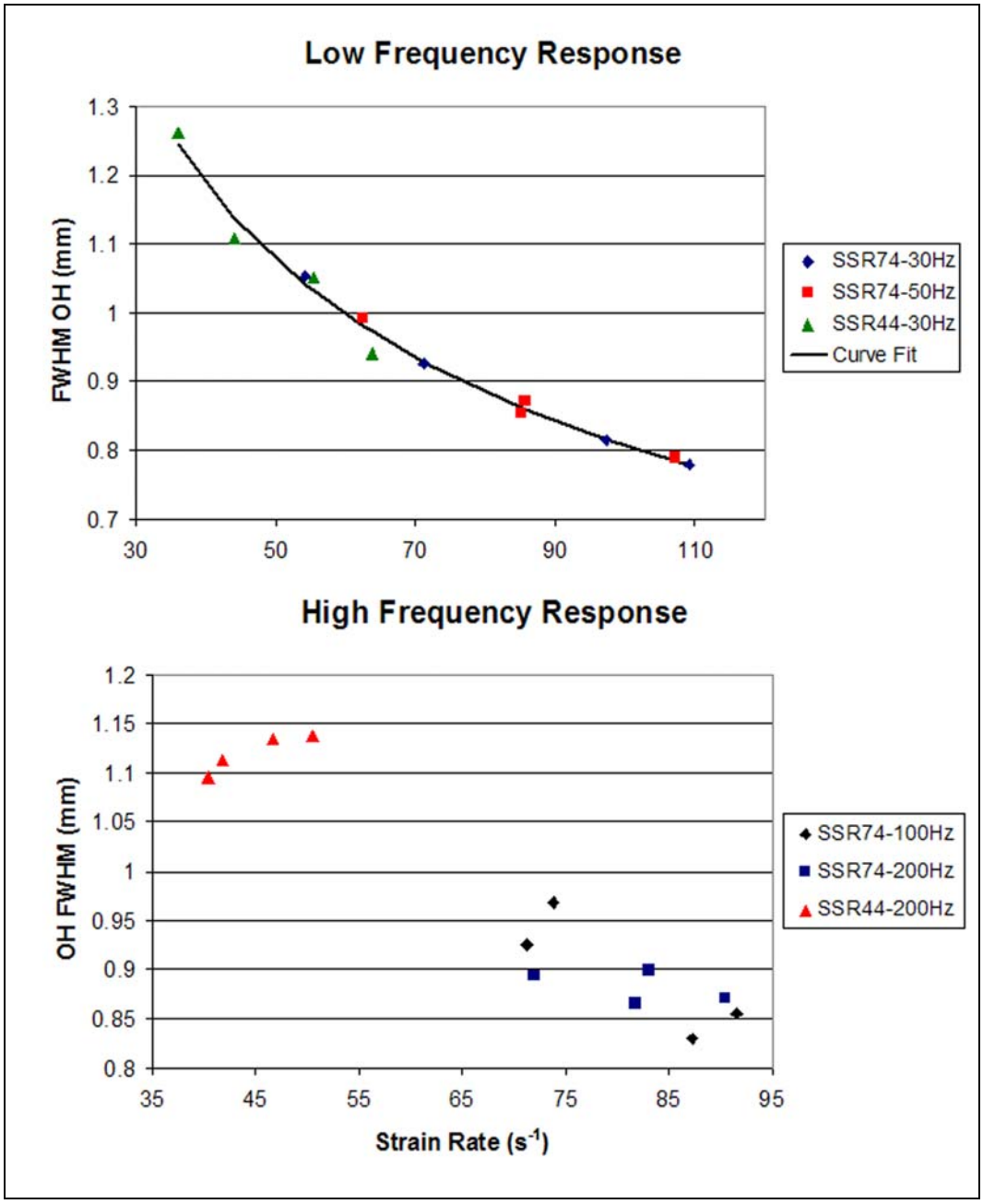

Figure 6-6 The low frequency (30 and 50 Hz) and high frequency (100 Hz and 200 Hz) response plots of the OH field thickness versus strain rate for two initial steady strain rates. Also, a $1/\sqrt{K}$ line fit is shown for the low frequency response illustrating the quasi-steady response at these frequencies

7 Soot Field Response to the Unsteady Flow Field

Due to the negative impact of pollutants formed during combustion processes, tremendous effort is being expended to understand the formation mechanisms of these pollutants. This interest is continually strengthened as greater health and environmental concerns are raised about these pollutants. Of particular interest is the desire for the reduction of soot levels present in the post combustion exhaust gases. In order to understand how to reduce the levels of these undesirable byproducts of combustion, an understanding of the fundamental formation mechanism of these pollutants and how they are affected by the reacting flow-fields where they are formed must be achieved.

To determine the effects of the transient flow field, LII measurements were performed in the counterflow diffusion flame burner with a sinusoidally varying flow field. Measurements were also conducted in unforced flow fields for a baseline measurement. Figure 7-1 shows the LII intensity profile around the centerline of the burner. It shows a steady increase around the 2 mm location of the plot and then the signal plateaus around 3 mm and then abruptly drops off around 4.3 mm. The pyrolysis reactions that lead to soot precursors are highly temperature sensitive, these reactions will initiate once the parent fuel diffuses to the point the gas temperatures are ~1400 K. Given sufficient time, primary particles will be formed and begin to agglomerate. Eventually, the agglomerated soot aggregate will reach the point where the concentration gradient driving it to the reaction zone is not sufficient to overcome the forces of the convective velocities, which are in the direction of the stagnation plane and away from the reaction zone. At this point the particle will be convected back to the stagnation plane. This

location is evident in Figure 7-1, where at the 4.3 mm location the soot particles amass at the stagnation plane and are then convected away via the radial velocities.

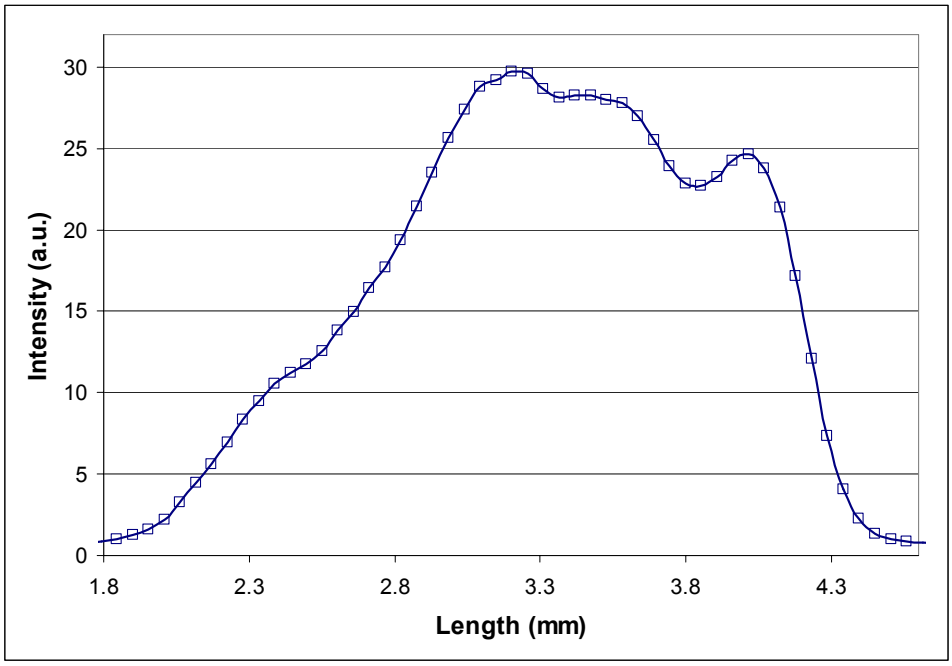

Figure 7-1 LII intensity profile in an unforced, steady GSR30s^{-1} flame around the burner centerline

The LII intensity profiles for a GSR 30 s^{-1} condition are shown in Figure 7-2 and Figure 7-3 for 30 and 100 Hz oscillations respectively and are shown at ten temporal locations in the oscillation. The various temporal sampling locations are represented as the percentage of that temporal location to the entire cycle time of the oscillation. Note that all scales are identical in each figure with the exception of the 80% condition of Figure 7-2. For the 30 Hz oscillation, the structure of the LII profile shows strong deviations from the unforced profile as shown in Figure 7-1. This is evident in the fluctuating peak value and the strong changes in the overall profile.

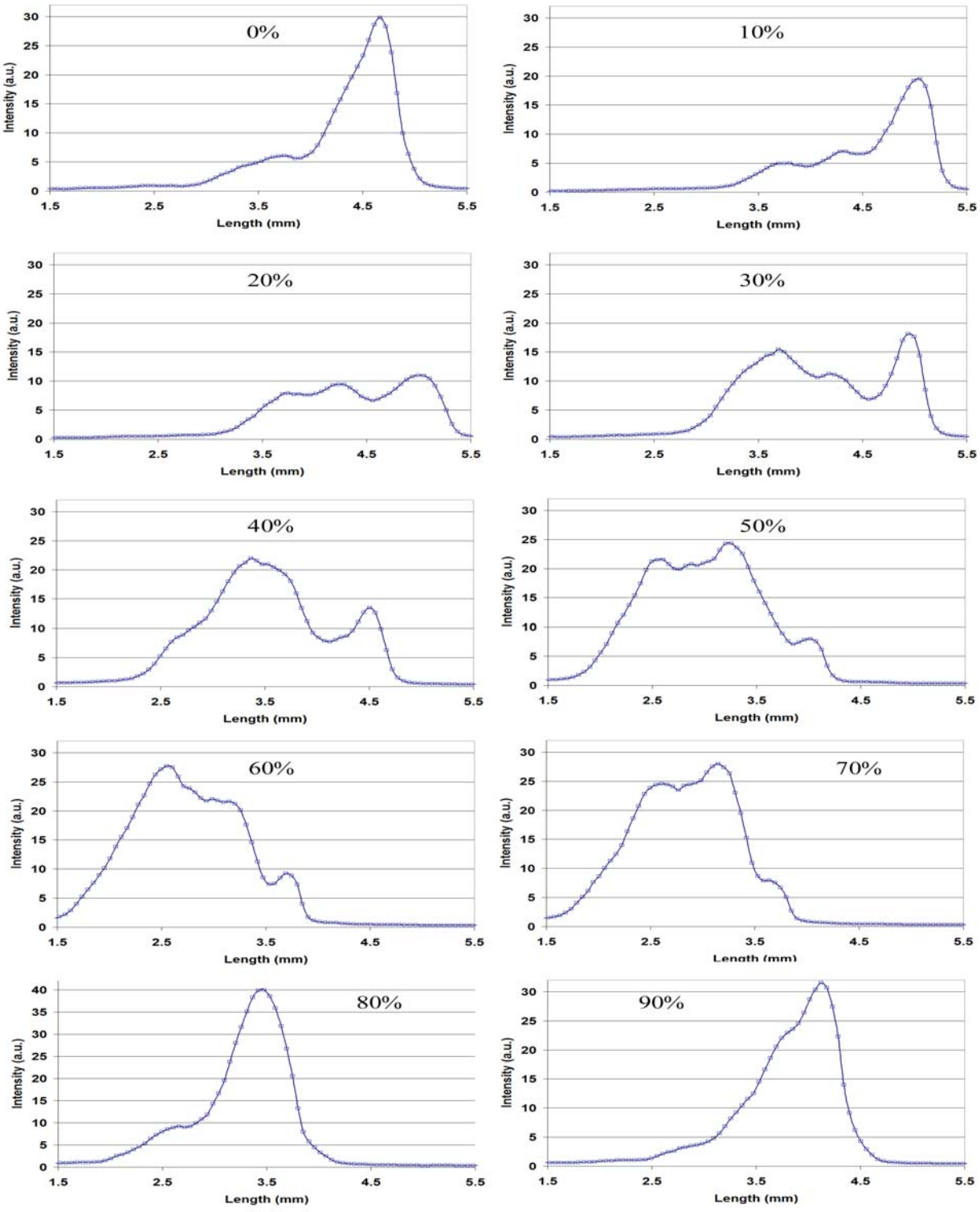

Figure 7-2 GSR 30s^{-1} axial LII profiles throughout a 30 Hz flow field oscillation

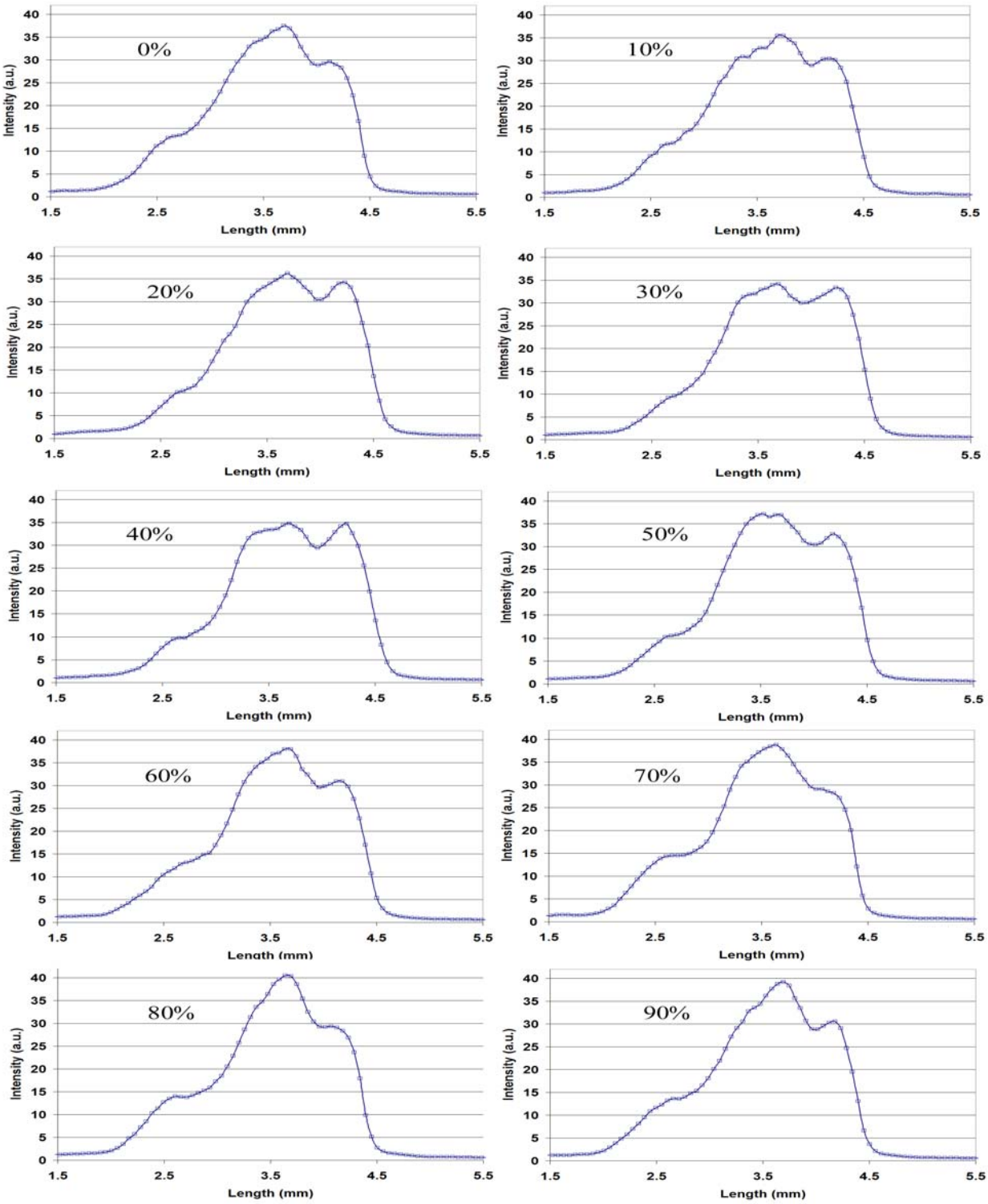

Figure 7-3 GSR 30s^{-1} axial LII profiles throughout a 100 Hz flow field oscillation

In fact, for most of the sequences shown in Figure 7-2 the profile is very dissimilar to that of the steady profile in shape and magnitude except for the 50, 60 and 70 % sampling locations. The changes in the LII profile are a result of the expansion and contraction of the high temperature region of the flow field around the reaction zone. As the reaction zone thickens and increases in temperature, which is consistent with a decreasing strain rate for a quasi-steady response, the high temperature region becomes thicker and thus allows for greater periods of time for the formation of the PAHs, subsequent particle inception and agglomeration processes to occur. That being said, it is still obvious that the general structure of the LII profile is dissimilar to that of the steady case even at 30 Hz oscillation. This is contrary to what has been seen previously in Chapters 4 and 5, where the reaction zone temperature and width were quasi-steady in structure and response throughout the oscillation at 30 and 50 Hz oscillations. This is a result of the characteristic time scales of the response of the various parameters, where the soot formation process is much longer relative to the chemical kinetic processes of combustion.

Upon review of the 100 Hz oscillation shown in Figure 7-3, it is obvious that a considerable change is evident in the response of the LII profile throughout the oscillation relative to the 30 Hz condition. For a 100 Hz oscillation, the general profile does exhibit small changes throughout the oscillation, but maintains a more consistent global structure that is very similar to the unforced, steady LII profile. This seems to suggest that the soot field will asymptote to a steady structure as the forcing frequency increases. This is likely a result of two effects. The first being that of the attenuated frequency response of the reaction zone with increasing forcing frequency as sited in Chapters 4 and 5. A second effect could be a result of

the smearing of the soot formation process with decreasing characteristic flow field fluctuations. As the time scale of the increase and decrease of the thermal expansion decreases to the point that it is similar to that of the soot formation process, it will smear the response of the soot field. The particle formation process alone occurs in ~ 1 ms so one would expect flow field fluctuations on this order will result in some smearing of the formation process.

Qualitative evaluation of Figure 7-2 and Figure 7-3 lead to the descriptions previously stated. Ideally, it is desirable to quantitatively describe the response of the LII profile and determine if there is a response function that can be derived from the data. In the previous sections, the peak temperature and reaction zone width were easily determined and were obvious ways of quantifying the response of the reaction zone, but attempting to choose a parameter such as the peak LII intensity seems inappropriate due to the multi-peak profiles. Instead, the LII profiles were integrated to determine a representative quantity that describes the entire LII signal. The MathCAD worksheet that performed this integration is shown in Appendix 3 and the worksheet that determines the parameters for the offset sine function is illustrated in Appendix 4.

Figure 7-4 shows the integrated profile values fitted to an offset sine function for the 30, 50 and 100 Hz forcing frequencies. This figure shows that the soot field is responding to the sinusoidally varying flow field and the amplitude of the response is decreasing with increasing forcing frequency. For the 30 and 50 Hz oscillations, the plotted data fits the sine function very nicely where the fit is not as good for the 100 Hz oscillation. This is likely due to the fact that a threshold is being reach for what can be resolved using LII. The random noise in the measurement is becoming large relative to the fluctuations.

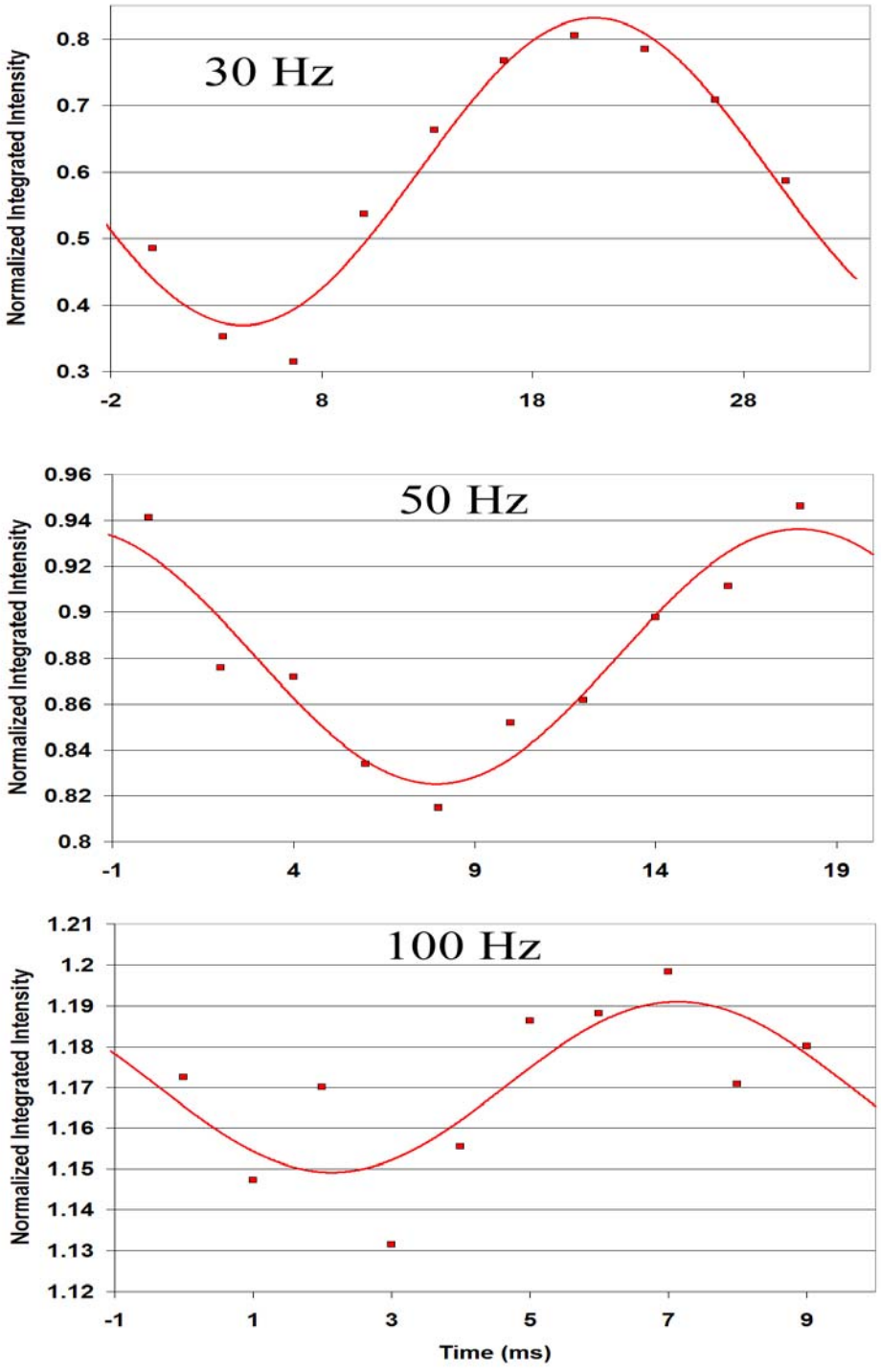

Figure 7-4 Offset sine function fitted to integrated LII signal for GSR 30s^{-1}

The offset sine function of the integrated profile has the form

$IP = LII_0 + LII_1 \cdot \sin(b \cdot t + LII_1)$ and the fitted parameters are illustrated in Table 7-1.

Table 7-1 Fitted sine function parameters to integrated LII profiles

	30	50	100	STEADY
LII_0	0.601	0.881	1.17	1
LII_1	0.231	0.056	0.021	0
LII_2	3.9	2.2	3.4	0

Table 7-1 illustrates that even at the lowest forcing frequency measured; the unsteady flow field has a strong unsteady effect on the LII profile. The mean integrated value at 30 Hz is ~40% lower than the steady case and from Figure 7-1 and Figure 7-2 there are significant departures from the steady LII profile. What is further illustrated is that as the forcing frequency increases, the mean integrated LII profile value approaches the steady value at 50 Hz and exceeds it at 100 Hz by ~14%. It appears that at elevated forcing frequencies the soot structure becomes reasonably steady in structure with enhanced mean soot production for the conditions measured.

8 Conclusions

The use of turbulent diffusion flames in combustion devices is very common due to their higher heat release rates relative to laminar diffusion flames. As the turbulent Reynolds number increases, there exists a range of eddy sizes where the characteristic turnover times of the smallest eddies are comparable to the diffusion times of the laminar flamelets and this results in a wide range of characteristic frequencies of the flow field. As a result, it is necessary to investigate the frequency response of flamelets to better understand the applicability of the flamelet model. In doing so, it is also important to investigate the effects of the time varying flow fields on pollutant formation. Of particular interest in this study were the effects of the unsteady flow field on the soot formation process.

In this investigation, the global response of the flow field/reaction zone was tested and quantified. Parameters quantified included the velocity field, strain rate, reaction zone thickness and reaction temperature and soot field incandescence. The conclusions of this work are as follows:

1) The width of the OH field appears to be responding quasi-steadily to the instantaneous strain rate for forcing frequencies of 30 Hz and 50 Hz; the calculated phase difference between the strain rate and width of the OH field are 183° and 185° respectively. However, at forcing frequencies of 100 Hz and 200 Hz, the phase lag of the OH field thickness grew to 210° and 241°, respectively.

2) For the weakly forced flames the sinusoidal response of the velocity, strain rate, and width of the OH field correlated well with the speaker oscillations at the given frequency. For the larger amplitude oscillations the data fit a sinusoid reasonably well, but in general the data did not fit the sine wave as well as the low amplitude oscillations. This is likely a result of oxygen leakage during the higher scalar dissipation rate conditions, which will lead to a non-symmetric sinusoid response.

3) A phase difference was present between the velocity and the strain rate, which was found to decrease with increasing forcing frequency. For an isothermal flow, it is expected that the strain rate will be in phase with the velocity for the forcing frequencies investigated here with the small separation distance of the reactant tubes. This phase shifting relationship for the reacting flow results from the distortions imposed on the velocity field due to a phase shifted thermal expansion.

4) The dilatation velocity was used as an indicator of flame temperature. The phase difference between the velocity and the dilatation velocity was found to increase with increasing forcing frequency. This increasing phase difference suggests the transport of reactants through the reactive-diffusive zone of the flame is the limiting step in the response of the flame sheet. The general trends described by the dilatation velocity were later verified from the 2-λ OH PLIF thermometry measurements.

5) At the 30 Hz and 50 Hz forcing frequencies, the maximum reaction-zone temperature was found to respond quasi-steadily as indicated by the ~180° phase shift relative to the strain rate variations. At higher forcing frequencies, 100 and 200 Hz, however, transient

behavior is evident from the phase relationship between the imposed sinusoidal strain and the resulting peak flame temperature where a ~0° phase shift was found between the strain rate and reaction zone maximum temperature at 200 Hz.

6) For smaller amplitude oscillations, when the oscillation amplitude (determined from the sine-curve fit) is normalized by the steady strain rate and plotted against the non-dimensional flow field frequency, it collapses onto a single line with a steep negative slope. This result provides validation to the numerical study of Egolfopoulos and Campbell. An implication of the Stokes plot is that the fluctuations of the reaction zone width are decreasing monotonically with increasing forcing frequency in a predictable manner for the conditions considered.

7) It was found that at low forcing frequencies (long characteristic time scales of flow field fluctuations) the flame responds quasi-steadily and the strain rate is an appropriate surrogate for the scalar dissipation rate. At high forcing frequencies, the direct correlation between strain rate and scalar dissipation rate is no longer valid and the scalar dissipation rate is likely a more appropriate measure of the flamelet response.

8) It was found that unlike the quasi-steady response of other measured parameters, the structure of the soot field showed significant deviations from the steady structure even at the lowest measured forcing frequency. The global structure of the LII profile does seem to asymptote to that of a steady structure with increasing forcing frequency.

9) It was shown that due to the multi-peak structure of the LII field, choosing a peak value is not an appropriate response marker for the soot field. Instead, the integrated LII profile

was used and was found to be an adequate way to characterize the response of the soot field.

10) As with the reaction zone thickness and peak temperature, an attenuated response of the integrated soot field fluctuations was noted with increasing forcing frequency, although the relative percent attenuation was much larger for the LII signal. This was evident by the reduction of the amplitude oscillation by ~90% between 30 and 50 Hz for a flame with an unforced global strain rate of 30 s^{-1}.

11) As previously stated, the reaction zone continued to respond in a sinusoidal manner at all frequencies which signals that the break down in the quasi steady response is not a result of the chemical kinetics, but a result of the mixture field response. The mixture field response was explained in the context of a diffusion limited response of the reaction zone.

9 Future Work

Although the amount of soot present in the post combustion gases is important, there is also a great interest in the size distribution of the particulates present. Health agencies are interested in these size distributions due to the fact that they overlap size ranges for which the human body has no natural filtering mechanism (Seinfeld and Pandis, 1996), which allows them to travel deep into the respiratory system. The extent of this transport into the respirator system is a significant concern since soot agglomerates are highly carcinogenic and mutagenic. Because of these factors, it is important to determine the effects of an unsteady flow field on the size distribution of particles formed. A two angle scattering measurement is being perfected so it can be applied in the counterflow diffusion flame burner for this exact purpose.

10 Bibliography

Ahn, b.T., Bastiaans, G.J., Albahadily, F., (1982) "Practical Determination of Flame Species via Laser Saturation Fluorescence Spectroscopy", *Appl. Spect*, **36**, 106-110.

Allen, M.G., Hanson, R.K., (1986) "Digital Imaging of Species Concentration Fields in Spray Flames", *Proc. Combust. Inst.*, **21**, 1755-1761.

Appel, J., Jungfleisch, B., Marquardt, M., Suntz, R., and Brockhorn, H. (1996) "Assessmentof Soot Volume Fractions from Laser-Induced-Incandescence by Comparison with Extinction Measurements in Laminar Premixed Flat Flames", *Proc. Combust. Inst.*, **26**, 2387-2395.

Barlow, R. S., and Carter, C. D., (1994) "Raman Rayleigh LIF measurements of nitric-oxide formation in turbulent hydrogen jet flames" *Combust. Flame,* **97**, 261-280.

Barlow, R. S., Sandia National Laboratories, *Personnel Communication*.

Barlow, R.S., Dibble, R.W., Chen, J.Y., Lucht, R.P., (1990) "Effect of Damköhler number on super equilibrium OH concentration in turbulent nonpremixed jet flames", *Combust. Flame,* **82**, 235-251.

Bilger, R. W., (1988) "The structure of turbulent nonpremixed flames", *Proc. Combust. Inst.*, **22**, 475-488.

Bilger, R.W. (1976) "Turbulent Jet Diffusion Flames", *Prog. Energy Comb. Sci.*, **1**, 87-109.

Bios International Corp., (2001) "Drycal User Manual" *Bios International Corp*.

Bray, K.N.C., Peters, N., (1994) *Turbulent Reaction Flows Ch. 2: Laminar Flamelets in Turbulent Flames*, Academic Press Ltd.

Brockhinke, A., Kohse-Höinghaus, K., (1996) "Double-pulse one-dimensional Raman and Rayleigh measurements for the detection of temporal and spatial structure in a turbulent H2-air diffusion flame" *Optics Letters*, **21(24)**, 2029-2031.

Brown, T.M., Pitz, R.W., Sung, C.J., (1998) " Oscillating Stretch effects on the structure and extinction of counterflow diffusion flames", *Proc. Combust. Inst.*, **27**,, 703-710.

Bryce, D.J., Ladommatos, N., Zhao, H., (2000) "Quantitative investigation of soot distribution by laser-induced incandescence" *Applied Optics*, **39(27)**, 5012-5022.

Burke, S.P. and Schumann, T.E.W. (1928) "Diffusion Flames", *Combustion Symposium*, 76th Meeting of Chemical Society, Swampscott, MA, 998-1003.

Carter, C.D., King, G.B., Laurendeau, N.M., (1992) "Saturated Fluorescence measurements of the hydroxyl radical in laminar high-pressure C2H6/O2/N2 flames", *Applied Optics*, **31(10)**, 1511-1522.

Carter, C.D., Laurendeau, N.M., (1994) "Wide- and Narrow-Band Saturated Fluorescence Measurements of Hydroxyl concentration in Premixed Flames from 1 bar to 10 bar" *Appl. Phys. B*., **58**, 519-528.

Cattolica, R. (1981) "OH Rotational Temperature from Two-Line Laser Excited Fluorescence", *Appl. Opt.*, **20**, 1156-1166.

Chan, C., Daily, J.W., (1980) "Measurement of Temperature in Flames using Laser Induced Fluorescence Spectroscopy of OH", *Applied Optics*, **19(12)**, 1963-1968.

Chidsey, I. L. and Crosley, D. R. (1980). "Calculated Rotational Transition Probabilities for the A-X System of OH," *J. Quant. Spectrosc. Radiat. Transfer*, **23**: 187-199.

Choi, M.Y., and Jensen, K.A. (1998) "Calibration and Correction of Laser-Induced Incandescence for Soot Volume Fraction Measurements", *Combust. Flame*, **112**, 485-491.

Cignoli, F., Benecchi, S., and Zizak, G. (1992) "Simultaneous one-dimensional visualization of OH, polycyclic aromatic hydrocarbons, and soot in a laminar diffusion flame", *Optics Letters*, **17**:4, 229-231.

Crosley, D.R., (1981) "Collisional Effects on Laser-Induced Fluorescence Flame Measurements," *Opt. Engin*, **20**, 511-521.

Crosley, D.R., Smith, G.P., (1983) "Two Photon Spectroscopy of the $A^2\Sigma$-$X^2\Pi_i$ System of OH", *J. Chem. Phys*., **79**, 4764-4773.

Daily, J.W., (1977) "Saturation Effects in Laser Induced Fluorescence Spectroscopy", *Appl. Opt.*, **16**, 568-571.

Darabiha, N., (1992) "Transient behavior of laminar counterflow hydrogen air diffusion flames with complex chemistry", *Combust. Sci. and Tech*., **86**, 163-181.

DeCroix , M.E., (1998) "The effects of unsteady hydrodynamics on soot formation in a counterflow diffusion flame", Ph.D. Thesis, North Carolina State Univ.

DeCroix, M.E., Roberts, W.L., (2000) "Transient flow field effects on soot volume fraction in diffusion flames", *Combust. Sci. Technol.*, **160**, 165-189.

Dieke, G. M. and Crosswhite, H. M. (1962). "The Ultraviolet Bands of OH," *J. Quant. Spectrosc. Radiat. Transfer*, **2**: 97-199.

Dimpfl, W. L. and Kinsey, J. L. (1979). "Radiative Lifetimes of OH($A^2\Sigma$) and Einstein Coefficients for the A-X System of OH and OD," *J. Quant. Spectrosc. Radiat. Transfer*, **21**: 233-241.

Donbar, J.M., Driscoll, J.F., Carter, C.D., (2001) "Strain Rates Measured along the Wrinkled Flame Contour within Turbulent Non-Premixed Jet Flames," *Combust. Flame*, **125**, 1239-1257.

DU, D.S., Wang, H., Law, C.K., (1998) "Soot Formation in Counterflow Ethylene Diffusion Flames from 1 to 2.5 Atmospheres", *Combust. Flame*, **113**, 264-270.

Du, J. and Axelbaum, R.L. (1995) "The Effect of Flame Structure on Soot-Particle Inception in Diffusion Flames", *Comb. Flame*, **100**, 367-375.

Dyer, M.M., Crosley, D.R., (1982) "Two-Dimensional Imaging of OH Laser-Induced Fluorescence in a Flame", *Optical Letters*, **7**, 382-384.

Eckbreth, A.C. (1988) *Laser Diagnostics for Combustion Temperature and Species*, Abacus Press.

Egolfopoulos, F. N., Campbell, C. S., (1996) "Unsteady counterflowing strained diffusion flames: Diffusion-limited frequency response "*J. Fluid Mech.* **318**, pp. 1-29

Fielding, J., Schaffer, A. M., Long, M. B., (1998) "Three-scalar imaging in turbulent non-premixed flames of methane", *Proc. Combust. Inst*. , **27**, 1007-1014.

Frank, J. H., Lyons, K. M., Marran, D. F., Long, M. B., Stårner, S. H., Bilger, (1994) "Mixture fraction measuremtns in turbulent nonpremixed hydrocarbon flames", *Proc. Combust. Inst*., **25**, 1159-1166.

Glassman, I. (1996) *Combustion* (Third Edition), Academic Press.

Greenhalgh, D.A. (1994) "Inelastic Scattering Laser Diagnostics; CARS, Planar LIF and Planar LII", *Optical Diagnostics for Flow Processes*, Plenum Press, New York, 357-389.

Hanson, R.K., Seitzman, J.M., Paul, H.P., (1990) "Planar Laser-Fluorescence Imaging of Combustion Gases", *Applied Optics B*, **50**, 441-454.

Haynes, B.S. and Wagner, H.Gg. (1981) "Soot Formation", *Prog. Energy Comb. Sci.*, **7**, 229-273.

Im, H., G., Chen, J. H., Chen, J., (1999) "Chemical response of methane air diffusion flames to unsteady strain rate", *Combust. Flame*, **118**, 204-212.

Im, H.G., Law, C.K., Kim, J.S., Williams, F.A., (1995) "Response of counterflow diffusion flames to oscillating strain rates" *Combust. Flame*, **100**, 21-30.

Jeffries, J. B., Kohse-Höinghaus, K., Smith, G. P., Copeland, R. A., and Crosley, D. R. (1988). "Rotational-Level-Dependent Quenching of OH($A^2\Sigma^+$) at Flame Temperatures," *Chemical Physics Letters*, **152(2,3)**: 160-166.

Kim, J.S., Libby, P.A., Williams, F.A., (1992) "On the displacement effects of laminar flames", *Combust. Sci. and Tech*., **87**, 1-25.

Kistler, J.S., Sung, C.J., Dreutz, T.G., Law, C.K., Nishioka, M., (1996) "Extinction of counterflow diffusion flames under velocity oscillations", *Proc. Combust. Inst*. **26**, 113-120.

Krass, BlJl, Zellmer, B.W., Puri, I.K., Singh, S., (1999) "Application of Flamelet Profiles to Flame Structure in Practical Burners", *Transactions of the ASME*, **121**, 66-72.

Kyritsis, D. C., Santoro, V. S., Gomez, A., (2001) "Measurements and computations of scalar dissipation rate in vortex perturbed counterflow diffusion flames", *Eastern States Section of the Combustion Institute*, 320-323.

Lengel, R. K. and Crosley, D. R. (1977). "Energy Transfer in $A^2\Sigma^+$ OH. I. Rotational," *The Journal of Chemical Physics*, **67(5)**: 2085-2101.

Lengel, R. K. and Crosley, D. R. (1978). "Energy Transfer in $A^2\Sigma^+$ OH. II. Vibrational," *The Journal of Chemical Physics*, **68(12):** 5309-5324.

Lucht, R.P., Laurendeau, N.M., Sweeney, D.W., (1982) "Temperature Measurements by two-line laser-saturated OH fluorescence in flames", *Applied Optics*, **21(20)**, 3729-3735.

Lucht, R.P., Sweeney, D.W., Laurendeau, N.M., (1983) "Laser-Saturated Fluorescence Measurements of OH Concentration in Flames" *Combust. Flame*, **50**, 189-205.

Luque, J., Crosley D.R., (1999) "LIFBASE: Database and Spectral Simulation Program (Version 1.5)", *SRI International Report,* MP 99-009.

McMillin B.K., Palmer, J.L., Antonio, A.L., Hanson, R.K., (1992) "Instantaneous, Two-Line Temperature Imaging of a H2/NO Jet in Supersonic Crossflow" *AIAA/SAE/ASME/ASEE 28th Joint Conf. and Exhibit*, AIAA-92-3347.

Melton, L.A. (1984) "Soot diagnostics based on laser heating", *Applied Optics*, **23**:13, 2201-2208.

Mewes, B., Seitzman, J.M., (1997) "Soot volume fraction and particle size measurements with laser-induced incandescence", *Applied Optics*, **36(3)**, 709-717.

Mueller, C., Driscoll, J. F., Reuss, D., and Drake, M., (1998) "Vorticity generation and attenuation as vortices convect through a premixed flame" *Combust. Flame,* **112**, 342–358 (1998).

Palmer, J. L. and Hanson, R. K. (1996). "Temperature Imaging in a Supersonic Free Jet of Combustion Gases with Two-Line OH Fluorescence," *Applied Optics*, **35(3)**: 485-499.

Palmer, J.L., Hanson, R.K., (1996) "Temperature imaging in a supersonic free jet of combustion gases with two-line OH fluorescence" *Applied Optics*, **35(3)**, 485-498.

Pellett, G.L., Isaac, K.M., Humphreys, JR., W.M., Gartrell, L.R., Roberts, W.L., Dancey, C.L., Northam, G.B., (1998) "Velocity and thermal structure, and strain-induced extinction of 14 to 100% hydrogen-air counterflow diffusion flames", *Combust. Flame*, **112**, 575-592.

Peters, N. (1986) "Laminar Flamelet Concepts in Turbulent Combustion", *Proc. Combust. Inst*., **21**, 1231-1250.

Peters, N. (2000) *Turbulent Combustion* (1st Edition), Cambridge University Press.

Peters, N., (1984) "Laminar Diffusion Flamelet Models in Non-Premixed Turbulent Combustion", *Prog. Energy Combust. Sci*., **10**, 319-339.

Pinson, J.A., Mitchell, D.L., Santoro, R.J., and Litzinger, T.A. (1993) "Quantitative, Planar Soot Measurements in a D.I. Diesel Engine Using Laser-Induced Incandescence and Light Scattering", SAE Technical Paper 932650.

Pitsch, H., Chen, M., Peters, N., (1998) "Unsteady flamelet modeling of turbulent hydrogen-air diffusion flames", *Proc. Combust. Inst*., **27**, 1057-1064.

Puri, I.K. and Seshadri, K. (1986) "Extinction of Diffusion Flames Burning Diluted Methane and Diluted Propane in Diluted Air", *Combust. Flame*, **65**, 137-150.

Puri, R., Santoro, R.J., and Smyth, K.C. (1994) "The Oxidation of Soot and Carbon Monoxide in Hydrocarbon Diffusion Flames", *Comb. Flame*, **97**, 125-144.

Quay, B., Lee, T.-W., Ni, T., and Santoro, R.J. (1994) "Spatially Resolved Measurements of Soot Volume Fraction Using Laser-Induced Incandescence", *Comb. Flame*, **97**, 384-392.

Raiche, G. A., Jeffries, J. B., Rensberger, K. J., and Crosley, D. R. (1990). "Vibrational Energy Transfer in OH $X^2\Pi_i$, $\nu = 2$ and 1," *The Journal of Chemical Physics*, **92(12):** 7258-7263.

Santoianni, D.A., DeCroix, M.E., Roberts, W.L., (2001) "Temperature imaging in an unsteady propane-air counterflow diffusion flame subjected to low frequency oscillations", *Flow Turbul. Combust.*, **66(1)**, 23-36.

Schäfer, Ketterle, W., Wolfrum, (1991) "Saturated 2D-LIF of OH and 2D Determination of Effective Collisionial Lifetimes in Atmospheric Pressure Flames", *Applied Physics B*, **52**, 341-346.

Seitzman, J.M., Hanson, R.K., (1993) "Two-Line Fluorescence for Temporally Resolved Temperature Imaging in a Reacting Supersonic Flow over a Body" *Appl. Phys. B*, **57**, 385-391.

Seitzman, J.M., Hanson, R.K., DeBarber, P.A., Hess, C.F., (1994) "Application of quantitative two-line OH planar laser-induced fluorescence for temporally resolved planar thermometry in reacting flows" *Applied Optics*, **33(18)**, 4000-4012.

Shaddix, C.R., and Smyth, K.C. (1996) "Laser-Induced Incandescence Measurements of Soot Production in Steady and Flickering Methane, Propane, and Ethylene Diffusion Flames, *Combust. Flame* , **107**:4, 418-452.

Stårner, S. H., Bilger, R.W., Dibble, R.W., Barlow, R.S., (1992) "Measurements of conserved scalars in turbulent diffusion flames" *Combust. Sci and Tech*., **86(1-6)**, 223-236.

Stårner, S. H., Bilger, R.W., Frank, J. H., Marran, D. F., Long, M. B., (1996) "Mixture fraction imaging in a lifted methane jet flame" *Combust. Flame*, **107**, 307-313.

Stefan, W., Schraml, S., Bader, K., Leipertz, A., (1998) "Performance characteristics of soot primary particle size measurements by time-resolved laser-induced incandescence" *Applied Optics*, **37(24)**, 5647-5658.

Sung, C. J., Law, C. K., and Axelbaum, R. L., (1994) "Thermophoretic effects on seeding particles in LDV measurements of flames", *Comb. Sci. Tech.* **99**, 119-132.

Sung, C.J., Kistler, M., Nishioka, M., Law, C.K., (1996) "Further studies on effects of thermophoresis on seeding particles in LDV measurements of strained flames" *Combust. Flame*, **105**, 189-201.

Sung, C.J., Liu, J.B., Law, C.K., (1995) "Structural Response of counterflow diffusion flames to strain-rate variations", *Combust. Flame,* **102**, 481-492.

Sutton, J. A., Driscoll, J. F., (2002) "Scalar Dissipation Rate Measurements in Flames – A Method to Improve Spatial Resolution by Using Nitric Oxide PLIF", *To appear in Proc. Combust. Inst, 29*.

Tait, N.P. and Greenhalgh, D.A. (1993) "PLIF Imaging of Fuel Fraction in Practical Devices and LII Imaging of Soot", *Ber. Bunsenges. Phys. Chem.*, **97**:12, 1619-1625.

Tait, N.P., Greenhalgh, D.A., (1992) "2D Laser Induced Fluorescence Imaging of Parent Fueld Fraction in Nonpremixed Combustion", *Proc. Combust. Inst*., **24***,* 1621-1628.

Tamura, M., Berg, P. A., Harrington, J. E., Luque, J., Jeffries, J. B., Smith, G. P., and Crosley, D. R. (1998). "Collisional Quenching of CH(A), OH(A) and NO(A) in Low Pressure Hydrocarbon Flames," *Combustion and Flame*, **114**: 502-514.

Tujishita, M., Hirano, A., Yokoo, M., Sakuraya, T., Takeshita, J., (1999) "Accurate Thermometry Using NO and OH Laser-Induced Fluorescenc in an Atmospheric Pressure Flame" *JSME International Journal Series B*, **42(1)**, 119-126.

Vander Wal R.L., Choi, M.Y., and Lee, K.-O. (1995) "The Effects of Rapid Heating of Soot: Implications When Using Laser-Induced Incandescence for Soot Diagnostics", *Comb. Flame*, **102**, 200-204.

Vander Wal, R.L. (1996) "Onset of Carbonization: Spatial Location Via Simultaneous LIF-LII and Characterization Via TEM", *Comb. Sci. Tech.*, **118**, 343-360.

Vander Wal, R.L., Jensen K.A., (1998) "Laser-induced incandescence: excitation intensity" *Applied Optics*, **37(9)**, 1607-1616.

Vander Wal, R.L., Jensen, K.A., and Choi, M.Y. (1997) "Simultaneous Laser-Induced Emission of Soot and Polycyclic Aromatic Hydrocarbons within a Gas-Jet Diffusion Flame", *Combust. Flame* , **109**, 399-414.

Watson, K.A., Lyons, K.M., Donbar, J.M., Carter, C.D., (1999) "Scalar and Velocity field measurements in a lifted CH4-air diffusion flame" *Comb. Flame*, 117, 257-271.

Welle, E.J., Roberts, W.L., Donbar, J.M., Carter, C.D., (2000) "Simultaneous PIV and OH-PLIF Measurements in an Unsteady Counterflow Propane-Air Diffusion *Flame" Proc. Combust. Inst.,* **28***,* 2021-2027.

Welle, E.J., Roberts, W.L., Donbar, J.M., Carter, C.D., (Present) "Simultaneous 2-λ and OH-PLIF Thermometry Measurements in an Unsteady Counterflow Propane-Air Diffusion Flame" To be submitted.

Wilcox, D.C., (1998) *Turbulence Modeling for CFD*, DCW Industries, Inc..

Will, S., Schraml, S., and Leipertz, A. (1996) "Comprehensive Two-Dimensional Soot Diagnostics Based on Laser-Induced Incandescence (LII)", *Proc. Combust. Inst.*, **26**, 2277-2284.

XU, F., Faeth, G.M., (2001) "Soot Formation in Laminar Acetylene/Air Diffusion Flames at Atmospheric Pressure", *Combust. And Flame*, **125**, 804-819.

Zhang, C., Atreya, A., and Lee, K. (1992) "Sooting Structure of Methane Counterflow Diffusion Flame with Preheated Reactants and Dilution by Products of Combustion", *Proc. Combust. Inst.,* **24**, 1049-1057.

Zhoa, J., Isaac, K.M, Pellett, G.L., (1996) "Global characteristic and structure of hydrogen-air counterflow diffusion flames", *Journal of Propulsion and Power*, **12(3)**, 534-542.

Appendix 1: LabView Boxcar VI (vi Diagram)

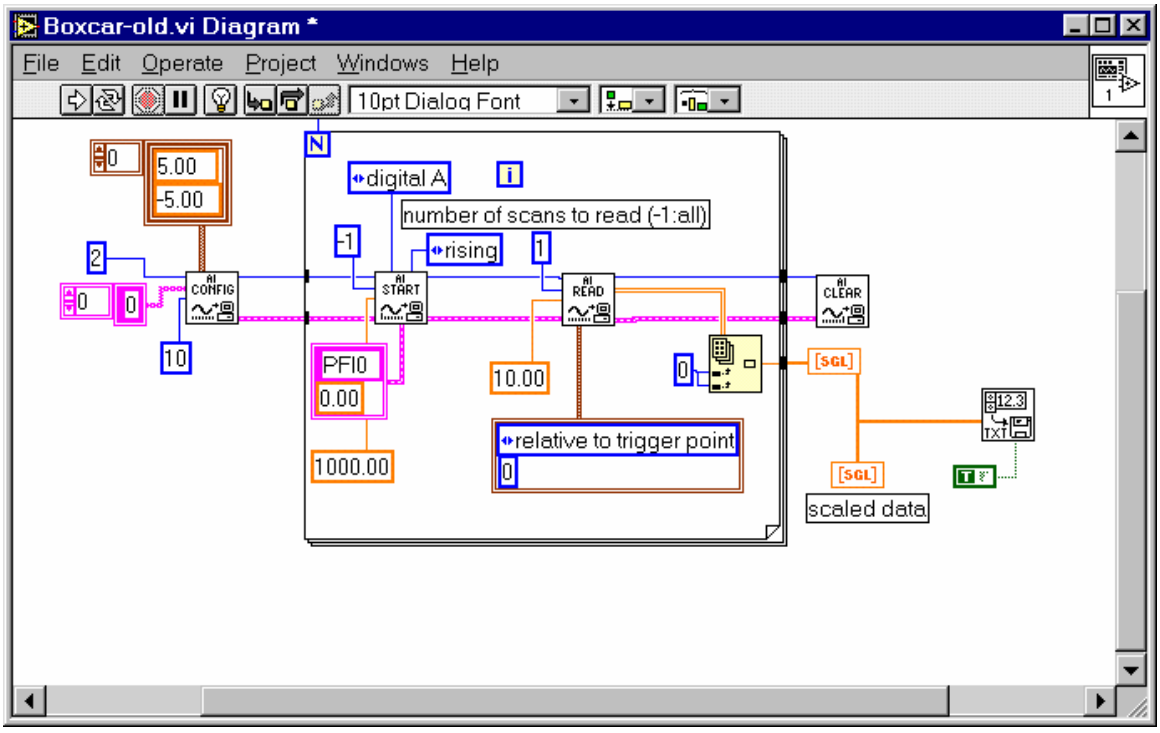

Appendix 1: LabView Boxcar VI (Front Panel)

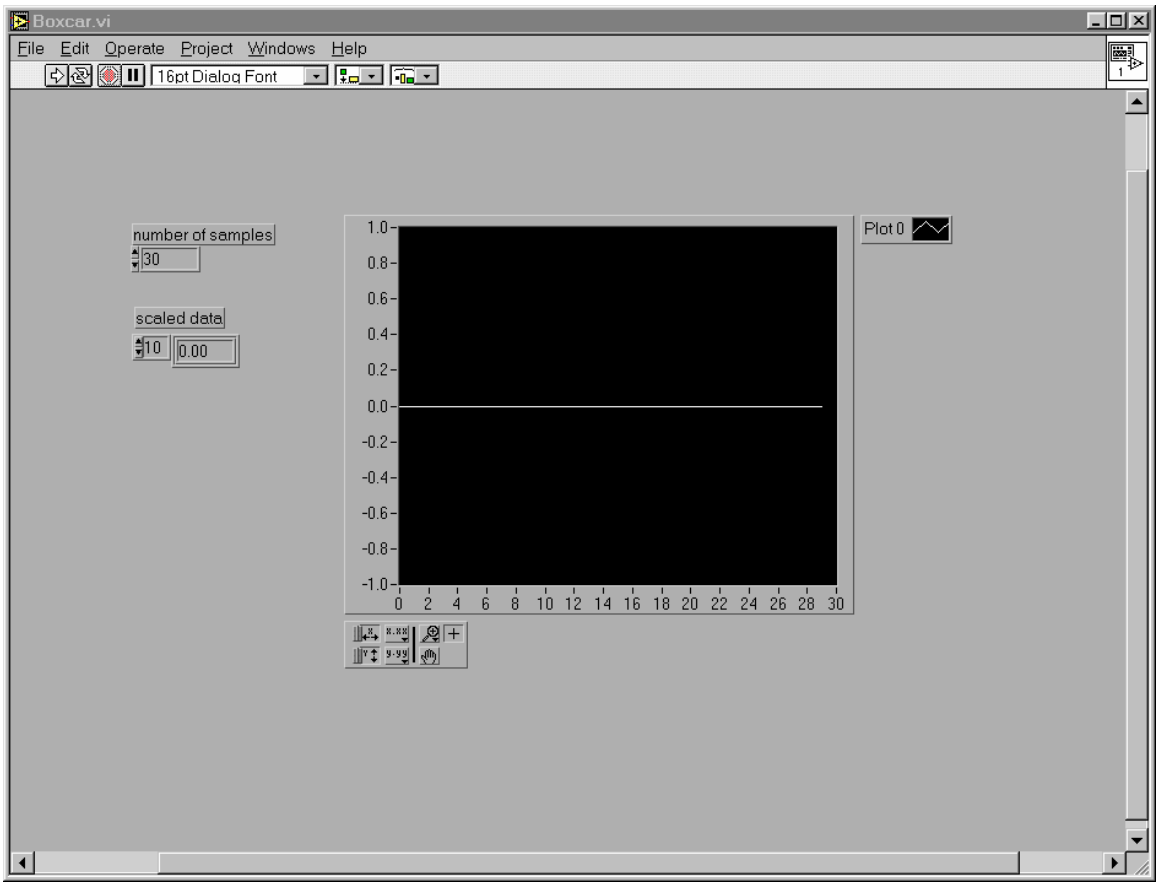

Appendix 2: MathCAD Flow Rates

Meter Calibration Data:

$$\begin{pmatrix} Meter_{Air} \\ LPM_{Air} \\ SLPM_{Air} \\ Meter_{C3H8} \\ LPM_{C3H8} \\ SLPM_{C3H8} \end{pmatrix} :=$$

Meter	Lpm	Slpm		Meter	Lpm	Slpm	
3.5	4.296	4.178		2.8	1.639	1.591	
4.7	5.529	5.371		3.7	2.08	2.015	
5.1	6.038	5.859		4.2	2.37	2.297	
5.7	6.645	6.447		4.7	2.566	2.491	
7	7.799	7.745		5.7	3.102	3.007	
8.7	9.589	9.287		7.1	3.823	3.706	
10	10.87	10.52		8	4.293	4.162	
10.5	11.3	10.95		8.5	4.54	4.401	
11	11.8	11.43		9	4.761	4.615	

Air Calibration

$Y := Meter_{Air}$ $X := SLPM_{Air}$

Enter degree of polynomial to fit:

$k := 3$

Number of data points:

$n := 10$ $z := regress(X, Y, k)$

Polynomial fitting function:

$fit(x) := interp(z, X, Y, x)$ $coeffs := submatrix(z, 3, length(z) - 1, 0, 0)$

Plots

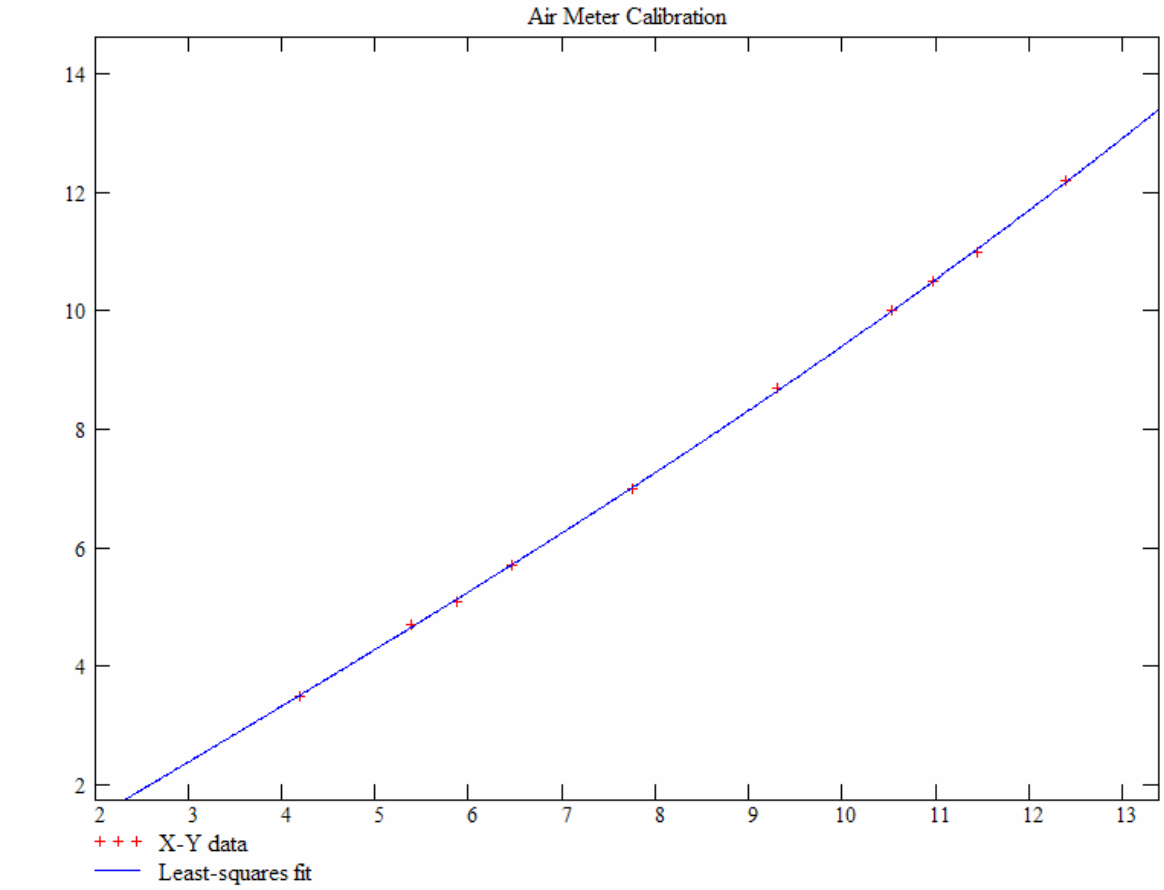

Propane Calibration

$Y1 := Meter_{C3H8}$ $X1 := SLPM_{C3H8}$

Enter degree of polynomial to fit:

$k := 3$

Number of data points:

$n := 11$ $z1 := regress(X1, Y1, k)$

Polynomial fitting function:

$coeffs1 := submatrix(z1, 3, length(z1) - 1, 0, 0)$

$fit1(x) := interp(z1, X1, Y1, x)$

Plots

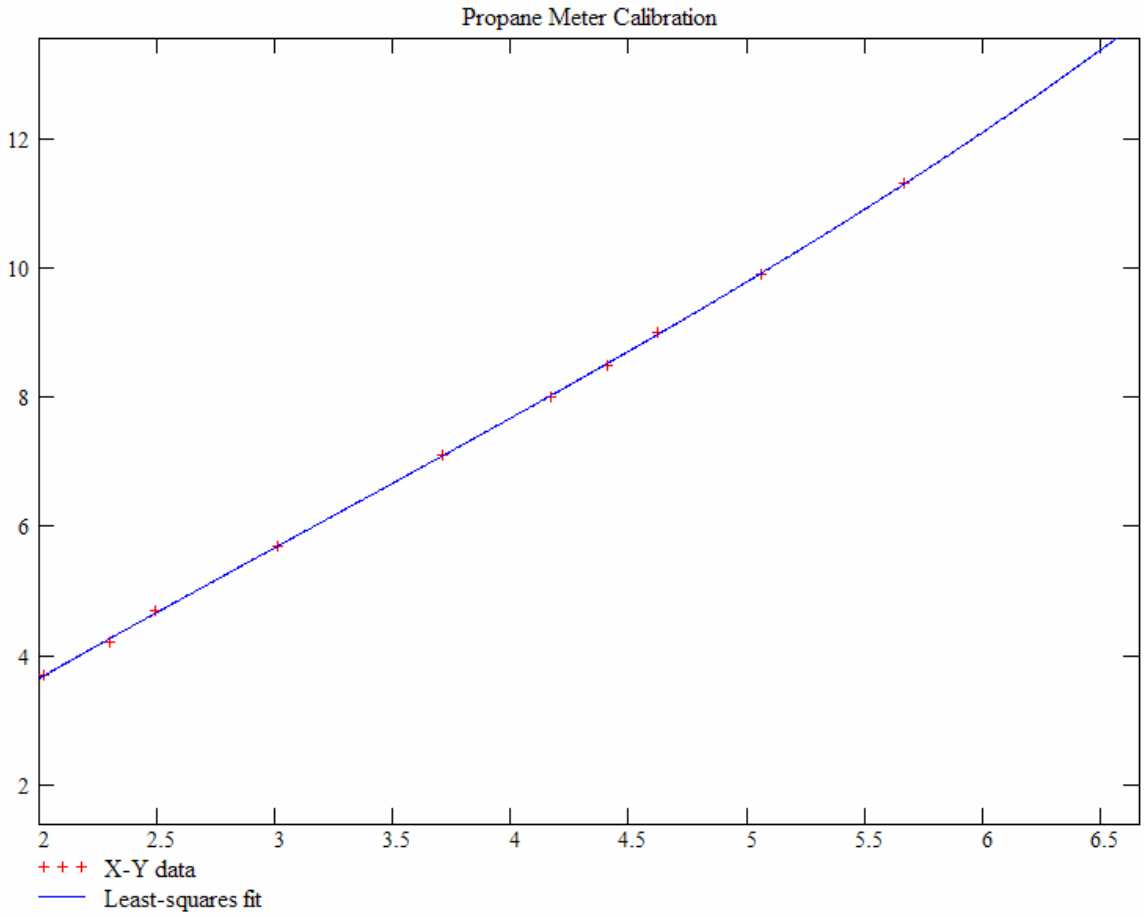
Propane Meter Calibration
12
10
8
6
4
2
2
2.5
3
3.5
4
4.5
5
5.5
6
6.5
X-Y data
Least-squares fit

$kJ := 1000 \cdot joule$ $kmole := 1000 \cdot mole$ $mm\_Hg := \frac{1}{25.4} \cdot in\_Hg$

$MW_{air} := 29 \cdot \frac{kg}{kmole}$ $MW_{propane} := 44.1 \cdot \frac{kg}{kmole}$ $R_{bar} := 8.314510 \cdot \frac{kJ}{kmole \cdot K}$

$R_{air} := \frac{R_{bar}}{MW_{air}}$ $R_{air} = 0.287 \frac{kJ}{kg \cdot K}$

$R_{propane} := \frac{R_{bar}}{MW_{propane}}$ $R_{propane} = 0.189 \frac{kJ}{kg \cdot K}$

$L_{gap} := \frac{25.4mm}{2}$

$D_{exit} := 2.413 \cdot cm$ $A_{exit} := \pi \cdot \left(\frac{D_{exit}}{2}\right)^2$ $A_{exit} = 4.573\,cm^2$

$T := (21 + 273.15) \cdot K$ $P := 1 \cdot atm$

$\rho_{air} := \frac{P}{R_{air} \cdot T}$ $\rho_{air} = 1.201 \frac{kg}{m^3}$

$\rho_{propane} := \frac{P}{R_{propane} \cdot T}$ $\rho_{propane} = 1.827 \frac{kg}{m^3}$

$i := 1, 2 .. 9$

$K_i :=$

$20 \cdot s^{-1}$
$30 \cdot s^{-1}$
$40 \cdot s^{-1}$
$50 \cdot s^{-1}$
$60 \cdot s^{-1}$
$70 \cdot s^{-1}$
$80 \cdot s^{-1}$
$90 \cdot s^{-1}$
$100 \cdot s^{-1}$

$U_{air_i} := \frac{K_i \cdot L_{gap}}{2}$

$U_{air_i} =$

12.7	$\frac{cm}{s}$
19.05	
25.4	
31.75	
38.1	
44.45	
50.8	
57.15	
63.5	

$P_{dot\_air_i} := \rho_{air} \cdot A_{exit} \cdot \left(U_{air_i}\right)^2$

$P_{dot\_air_i} =$

$8.862 \cdot 10^{-5}$
$1.994 \cdot 10^{-5}$
$3.545 \cdot 10^{-5}$
$5.539 \cdot 10^{-5}$
$7.976 \cdot 10^{-5}$
$1.086 \cdot 10^{-4}$
$1.418 \cdot 10^{-4}$
$1.795 \cdot 10^{-4}$
$2.215 \cdot 10^{-4}$

N

$Q_{air_i} := \rho_{air} \cdot A_{exit} \cdot U_{air_i}$

$U_{propane_i} := \left(\frac{P_{dot\_air_i}}{\rho_{propane} \cdot A_{exit}} \right)^{\frac{1}{2}}$

$U_{propane_i} =$

10.299
15.448
20.597
25.747
30.896
36.046
41.195
46.344
51.494

$\frac{cm}{s}$

$Q_{propane_i} := \rho_{propane} \cdot A_{exit} \cdot U_{propane_i}$

$P_{dot\_propane_i} := \rho_{propane} \cdot A_{exit} \cdot \left(U_{propane_i}\right)^2$

$Q_{propane_i} =$

$8.605 \cdot 10^{-5}$
$1.291 \cdot 10^{-4}$
$1.721 \cdot 10^{-4}$
$2.151 \cdot 10^{-4}$
$2.581 \cdot 10^{-4}$
$3.012 \cdot 10^{-4}$
$3.442 \cdot 10^{-4}$
$3.872 \cdot 10^{-4}$
$4.302 \cdot 10^{-4}$

$\frac{kg}{s}$

$Q_{air_i} =$

$6.978 \cdot 10^{-5}$
$1.047 \cdot 10^{-4}$
$1.396 \cdot 10^{-4}$
$1.744 \cdot 10^{-4}$
$2.093 \cdot 10^{-4}$
$2.442 \cdot 10^{-4}$
$2.791 \cdot 10^{-4}$
$3.14 \cdot 10^{-4}$
$3.489 \cdot 10^{-4}$

$\frac{kg}{s}$

$P_{dot\_propane_i} \cdot 10^5 =$

0.886
1.994
3.545
5.539
7.976
10.856
14.179
17.945
22.154

N

$P_{dot\_air_i} \cdot 10^5$

0.886
1.994
3.545
5.539
7.976
10.856
14.179
17.945
22.154

N

$LPM_{propane_i} := Q_{propane_i} \cdot \frac{R_{propane} \cdot T}{P}$

$LPM_{air_i} := Q_{air_i} \cdot \frac{R_{air} \cdot T}{P}$

$LPM_{propane_i} =$

2.8
4.2
5.7
7.1
8.5
9.9
11.3
12.7
14.1

$\frac{L}{min}$

$LPM_{air_i} =$

3.5
5.2
7
8.7
10.5
12.2
13.9
15.7
17.4

$\frac{L}{min}$

$K_i \cdot s =$

20
30
40
50
60
70
80
90
100

$$X_{C3H8_i} := LPM_{propane_i} \cdot \frac{min}{L} \qquad X_{Air_i} := LPM_{air_i} \cdot \frac{min}{L}$$

$$Meter_{C3H8_i} := coeffs1_0 + coeffs1_1 \cdot X_{C3H8_i} + coeffs1_2 \cdot \left(X_{C3H8_i}\right)^2 + coeffs1_3 \cdot \left(X_{C3H8_i}\right)^3$$

$$Meter_{Air_i} := coeffs_0 + coeffs_1 \cdot X_{Air_i} + coeffs_2 \cdot \left(X_{Air_i}\right)^2 + coeffs_3 \cdot \left(X_{Air_i}\right)^3$$

$Meter_{C3H8_i}$ =

5.3
8.2
11.3
14.9
19.5
25.3
32.6
41.8
53.1

$Meter_{Air_i}$ =

2.8
4.5
6.2
8
9.9
12
14.1
16.5
19

$K_i \cdot s$ =

20
30
40
50
60
70
80
90
100

Appendix 3: MathCAD Numerical Integration

Enter a matrix of X-Y data to be interpolated:

$\begin{pmatrix} X \\ Y \end{pmatrix} :=$

X	Y
1	4.9831
2	5.1441
3	5.2797
4	5.4068
5	5.5085
6	5.5424
7	5.5932
8	5.6525

Spline coefficients:

$S := \text{cspline}(X, Y)$

Fitting function:

$\text{fit}(x) := \text{interp}(S, X, Y, x)$

Integral fitting function:

$n := 0 .. \text{rows}(X) - 2$

$\text{ifit}(x) := \int_0^x \text{fit}(\xi)\, d\xi \quad IX_n := X_{n+1}$

$\text{rows}(X) - 2 = 66 \qquad \text{maxn} := \text{rows}(X) - 2 \qquad \text{ifit}(\text{maxn}) = 246.2$

$$IY_0 := \left(\frac{Y_0 + Y_1}{2}\right)\cdot(X_1 - X_0)$$

trapezoidal approximation to integral (a crude, but valid comparison)

$$n := 1 .. \text{rows}(X) - 2$$

$$IY_n := \left(\frac{Y_n + Y_{n+1}}{2}\right)\cdot(X_{n+1} - X_n) + IY_{n-1}$$

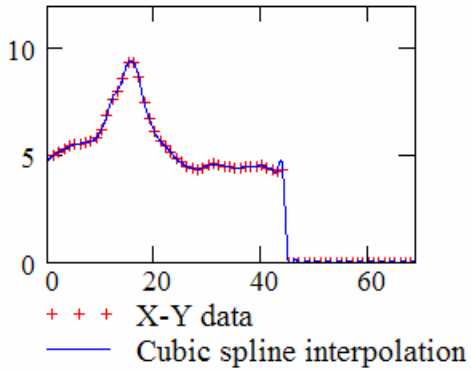

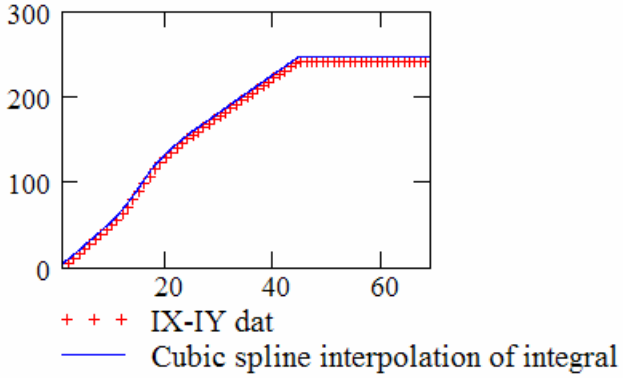

Appendix 4: MathCAD Offset Sine Function

Strain Rate Data:

$F := 100 \qquad f := \frac{1}{F}$

$$vx := \begin{pmatrix} 0 \\ 2.5 \\ 5 \\ 7.5 \end{pmatrix} \cdot 10^{-3} \qquad vy := \begin{pmatrix} 1.409571737 \\ 1.420355346 \\ 1.394166581 \\ 1.355140187 \end{pmatrix}$$

The first element contains the function that will approximate the data. The others contain the partial derivatives:

Applied Velocity Field period: $b := \frac{2 \cdot \pi}{f} \qquad b = 628.319$

$$Func(z, u) := \begin{pmatrix} u_0 + u_1 \cdot \sin(b \cdot z + u_2) \\ 1 \\ \sin(b \cdot z + u_2) \\ u_1 \cdot \cos(b \cdot z + u_2) \end{pmatrix}$$

This vector contains guess values for the parameters u_0, u_1, and u_2.

$$vg := \begin{pmatrix} 48.005 \\ 30 \\ 4 \end{pmatrix} \qquad P := genfit(vx, vy, vg, Func) \qquad P = \begin{pmatrix} 1.39481 \\ -0.0335 \\ 9.65675 \end{pmatrix}$$

Best functional fit to data (graphed below):

$i := 0..12$ $\quad r := -.5f, -.499 \cdot f .. f$ $\quad Z(r) := P_0 + P_1 \cdot \sin(b \cdot r + P_2)$